KU LEUVEN

ARENBERG DOCTORAL SCHOOL
Faculty of Science

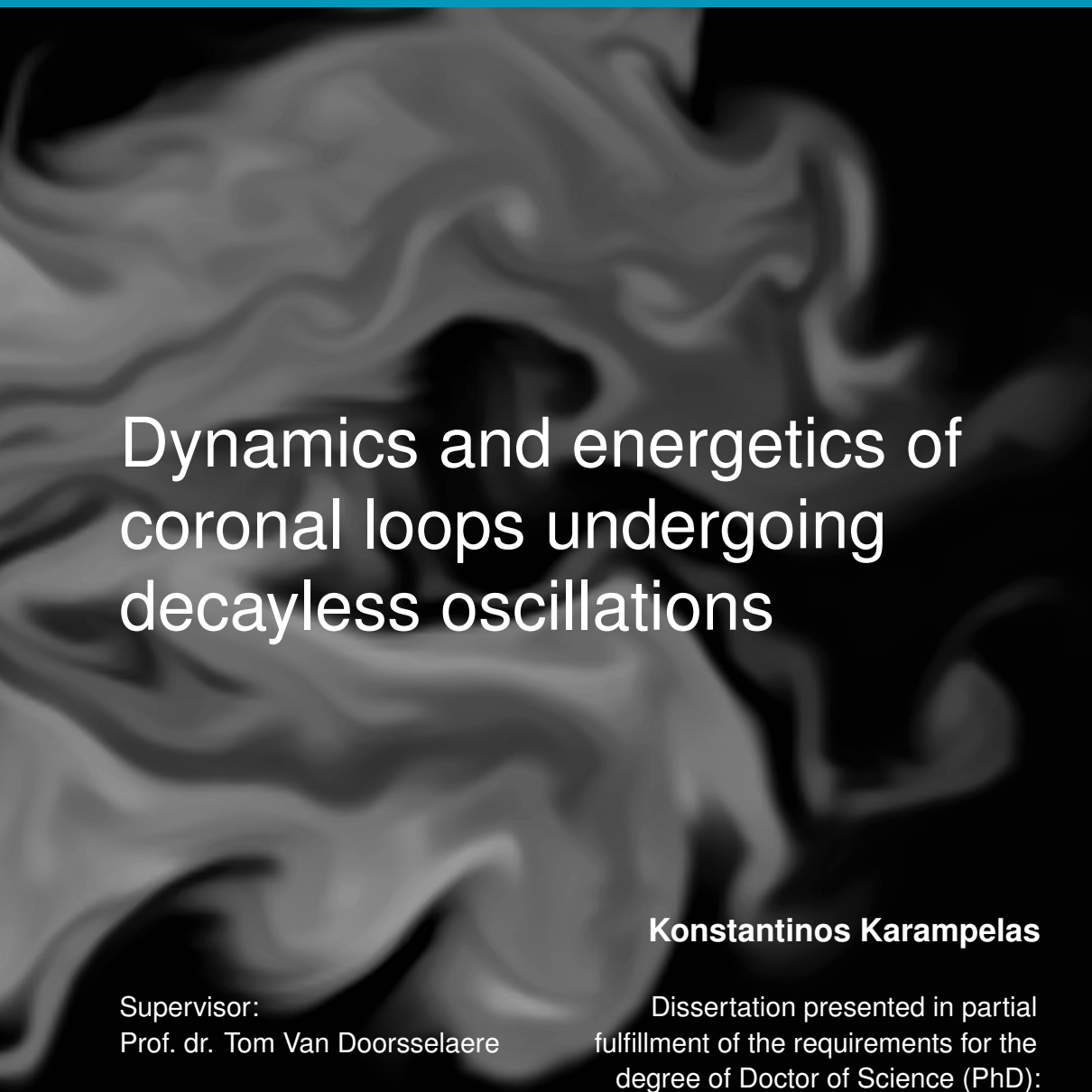

Dynamics and energetics of coronal loops undergoing decayless oscillations

Konstantinos Karampelas

Supervisor:
Prof. dr. Tom Van Doorsselaere

Dissertation presented in partial fulfillment of the requirements for the degree of Doctor of Science (PhD): Mathematics

September 2019

Dynamics and energetics of coronal loops undergoing decayless oscillations

Konstantinos KARAMPELAS

Examination committee:
Prof. dr. Tim Verdonck, chair
Prof. dr. Tom Van Doorsselaere, supervisor
Prof. dr. Stefaan Poedts
Prof. dr. ir. Giovanni Lapenta
Dr. Patrick Antolin
(Northumbria University)
Prof. dr. Valery Nakariakov
(University of Warwick)

Dissertation presented in partial fulfillment of the requirements for the degree of Doctor of Science (PhD): Mathematics

September 2019

© 2019 KU Leuven – Faculty of Science
Uitgegeven in eigen beheer, Konstantinos Karampelas, Celestijnenlaan 200B, box 2400, room 03.35, B-3001 Leuven (Belgium)

Alle rechten voorbehouden. Niets uit deze uitgave mag worden vermenigvuldigd en/of openbaar gemaakt worden door middel van druk, fotokopie, microfilm, elektronisch of op welke andere wijze ook zonder voorafgaande schriftelijke toestemming van de uitgever.

All rights reserved. No part of the publication may be reproduced in any form by print, photoprint, microfilm, electronic or any other means without written permission from the publisher.

Acknowledgements

All things must come to an end... even a PhD. Or especially that. No matter how anyone looks at it, a PhD is a long and tiresome journey, while being too short at the same time! Long and tiresome, since it takes years, stress and a lot of effort for a student to complete. Too short, because four years are not just enough when you are having such a great time.

But first of all, I feel the need to thank my supervisor, Tom. I still remember that summer of 2015, when I received an email from him, replying to my application. During a critical, and slightly uncertain point regarding my future steps, he gave me a chance to continue with my studies, and pursue one of my life goals. I am not exaggerating when saying that he is a really good supervisor, near whom I have learned many things about the field. And what a vast field it is. The Sun is just one star, but it surely is an exciting one to study, with a very active community of researchers, which I hope to remain a part of for many years to come.

I would also like to thank all the members of my examination committee for their willingness to read and judge my work. And of course my BSc and MSc thesis supervisor, Nektarios Vlahakis. Not only was I introduced to MHD by him, but I was also given the chance to work on an actual research project. And for a bachelor student, not many things can be more motivating than that.

But coming back to the PhD life, I can argue that these were some of the best years of my life so far. Years full of excitement, accomplishment, and even disappointments. After all, what good would life be if everything went as planned? The past and current members of CmPA made this an exciting journey, which I wish I could repeat. How can I forget the hospitality of Norbert and Fabio, or the game nights with Jo, Julia and Dimitris? I also have to thank Dimitris, for always being willing to help me with my questions, or to just listen to me complaining. I would like to apologise to Andrei, for not managing to jam together, although music is probably better for it. To the young Greeks

of the CmPA, Lia and Alex, to Camilla, Chris, Dana, Brecht and Bieke, to Matthieu, Bart and Yana, to Christine, Skralan, Nicolas, Michaël and Mingzhe, to all the past and present members of CmPA and to everyone from our office over the years I say a big 'Thank you for everything'.

I was also lucky enough to meet a lot of nice people over the years, both on conferences and in Leuven. But I should mention and thank the "locals", Ana, Michael and Milos, Shreeya, and Marilena for the dinners, beers and board game nights that we had. They really made this difficult last year a little easier to endure. Ana and Michael, however, would agree that we should have practised Dutch more often.

I also cannot forget my old friends. First of all, the old guard from UoA, Pericles, Giannis, Giorgos and Stelios. It was hard to stay in touch, but I was always happy to meet and talk to them on any given chance. Then, my old friend Charis, the conference buddy and family man. Then there is Efi, my old friend from school, to whom I wish the best to her and her family. I should not forget to mention Stavros and Alexandros, my fellow soldiers and good friends, whom I would meet almost every time I was back to Greece.

Last, but definitely not least, I want to thank my good friend Leela. She was the one who convinced me to keep searching for a PhD all those years ago, and always understood why I would feel disappointed at times. As a fellow doctoral student, she knows better that anyone of all the problems that one must face in order to finish a PhD, and I wish her a quick and successful conclusion to her studies.

As for my family, I would not have made it this far without their love and support over all these years. I know that they are proud of me, and I also love them more than anything.

Kostas,
September the 13th, 2019

Abstract

The Sun, as the nearest star to Earth, has been extensively studied ever since the development of modern Astrophysics. The large number of multi-frequency observations has shed light on many of the phenomena existing in the solar interior and the solar atmosphere, but not without generating a whole range of questions regarding the nature of these processes. The sheer volume of observations performed over the decades by ground and space observatories demands the development of new theories and models that can address them.

It has become widely accepted that the solar atmosphere is not an assembly of static, clearly defined layers, but is instead a widely dynamic part of the Sun, filled with flows, oscillations and energetic phenomena, like flares. Waves and oscillations are some of the most common observed phenomena across the layers of the solar atmosphere, like the chromosphere and the corona. Of particular interest have been the transverse waves in the solar corona, ever since their discovery in coronal loops in the late 90s, and the revelation of their ubiquitous nature in the solar atmosphere, during the late 2000s.

The aforementioned loops are some of the most basic structures found in the lower corona and the transition region. Stretching over different layers of the solar atmosphere, they transfer energy in the form of waves across those layers. Loops are not only sites of different types of waves, but can serve as a valuable tool in coronal seismology, i.e. using the observations to deduce the values of parameters like the magnetic field and the density in those environments.

One of the most important unsolved mysteries in solar physics is the multi-million temperature of the solar corona, with different heating mechanisms being under consideration. Of particular value is the way energy can be transferred from the lower atmosphere in to the corona, and how it gets dissipated to increase the plasma temperature. The interest in oscillating loops lies in their nature as potential candidates of wave heating of the solar atmosphere.

However, modern astrophysics, including solar physics, do not only rely on

observations and theoretical models, but also in experiments. And since neither full scale laboratory nor in situ experiments are physically possible, we rely on numerical studies in order to test our theories. 3D simulations try to shed light on the underlying mechanisms, while post-processing of the results gives us synthetic emission maps, which can be directly compared to the real observations.

This study focuses on wave heating in coronal loops, which undergo continuous driving. The layout of this manuscript shows the evolution of our used models over the years, and the respective results at each step. In Chapter 3 we present our numerical results on wave heating for both footpoint driven and impulsively oscillating coronal loops. In Chapter 4, we focus on the effects of the developing instabilities on the internal structure of loops. The aforementioned results are expanded in Chapter 5 for a more realistic model, through the inclusion of gravity and additional dissipation parameters. Finally, the energy-bearing capabilities of continuously oscillating loops are considered in Chapter 6.

Beknopte samenvatting

De zon is, als de dichtstbijzijnde ster van de aarde, uitgebreid bestudeerd sinds de ontwikkeling van de moderne astrofysica. Het grote aantal waarnemingen met in meerdere golflengtes heeft veel van de fenomenen laten zien, die bestaan in het binnenste van de son en de zonne-atmosfeer, maar niet zonder een hele reeks vragen te genereren met betrekking tot de aard van deze processen. Het enorme volume van grotendeels continue observaties gemaakt door heen tientallen jaren vereist de ontwikkeling van nieuwe theorieën en modellen die hen kunnen verklaren.

Het is algemeen geaccepteerd dat de zonne-atmosfeer geen verzameling is uit statische, duidelijk gedefinieerde lagen, maar in plaats daarvan het een breed dynamisch deel van de zon is, gevuld met stromen, oscillaties en energetische verschijnselen, zoals flares. Golven en oscillaties zijn enkele van de meest voorkomende waargenomen fenomenen in de lagen van de zonne-atmosfeer, zoals de chromosfeer en de corona. Van bijzonder belang zijn de transversale golven in de zonnecorona, sinds hun ontdekking in coronale lussen eind jaren 90, en de onthulling van hun alomtegenwoordige aard in de atmosfeer van de zon, eind jaren 2000.

De hiervoor genoemde lussen zijn enkele van de meest fundamentele structuren gevonden in de onderste corona en de transitieregio. Ze strekken zich uit over verschillende lagen van de atmosfeer en dragen energie over in de vorm van golven doorheen die lagen. Lussen zijn niet alleen locaties waar verschillende soorten golven voorkomen, maar de golven kunnen als een waardevol hulpmiddel dienen in coronale seismologie, d.w.z. de waarnemingen gebruiken om de waarden van parameters zoals het magnetische veld en de dichtheid in die omgevingen af te leiden.

Een van de belangrijkste onopgeloste mysteries in de zonnefysica is de temperatuur van meer dan een miljoen graden van de zonnecorona, met verschillende mogelijke verhittingsmechanismen. Van groot belang is de manier

waarop energie van de lagere atmosfeer naar de corona kan worden overgebracht en hoe deze wordt gedissipeerd om de plasmatemperatuur te verhogen. De interesse in oscillerende lussen ligt in hun karakter als potentiële kandidaten voor golfverwarming van de zonne-atmosfeer.

Moderne astrofysica, waaronder zonnefysica, vertrouwten echter niet alleen op observaties en theoretische modellen, maar ook op experimenten. En aangezien laboratoriumwerk op ware grootte en in situ-experimenten fysiek onmogelijk zijn, vertrouwen we op numerieke studies om onze theorieën te testen. 3D-simulaties proberen de onderliggende mechanismen te verlichten, terwijl de bewerking van de resultaten ons synthetische emissie oplevert, die direct kunnen worden vergeleken met de echte waarnemingen.

Deze studie richt zich op de verhitting door golven in coronale lussen, die continu aangedreven worden. De afdeling van dit manuscript toont de evolutie van onze gebruikte modellen door de jaren heen, en de respectieve resultaten van elke stap. In hoofdstuk 3 presenteren we onze numerieke resultaten op golfverhitting voor zowel voetpuntgedreven als impulsief oscillerende coronale lussen. In hoofdstuk 4 concentreren we ons op de effecten van de zich ontwikkelende instabiliteiten op de interne structuur van lussen. De bovengenoemde resultaten worden in hoofdstuk 5 uitgebreid voor een meer realistisch model, door de uitvoering van zwaartekracht en extra dissipatieparameters. Ten slotte worden de energiedragende mogelijkheden van continu oscillerende lussen in hoofdstuk 6 behandeld.

List of Abbreviations

AIA Atmospheric Imaging Assembly

CFL Courant–Friedrichs–Lewy

EIS EUV imaging spectrometer

EUV Extreme Ultra Violet

GLM Generalized Lagrangian Multiplier

Hinode The solar observing satellite "Hinode"

HLL Harten-Lax-van Leer

HLLC Harten-Lax-van Leer-Contact

HLLD Harten-Lax-van Leer-Discontinuities

JAXA Japan Aerospace Exploration Agency

KH(I) Kelvin-Helmholtz (instability)

MHD magnetohydrodynamics

NASA National Aeronautics and Space Administration

SDO Solar Dynamics Observatory

SOHO Solar and Heliospheric Observatory Homepage

STEREO Solar Terrestrial Relations Observatory

TRACE Transition Region and Coronal Explorer

TWIKH Transverse Wave Induced Kelvin-Helmholtz

Contents

Abstract iii

Beknopte samenvatting v

List of Abbreviations vii

Contents ix

1 Introduction 1

1.1 Prologue: What is Astrophysics? 1

1.2 The Sun 3

2 Theory and methods 21

2.1 Prologue 21

2.2 MHD equations 23

2.2.1 Contribution from electromagnetism 23

2.2.2 Fluid equations 25

2.2.3 The complete system 27

2.3 MHD waves 28

2.3.1 Linear MHD waves in a uniform medium 28

2.3.2 Linear MHD waves in a cylindrical flux tube 31

2.4 Wave damping mechanisms 34
2.5 Computational MHD 39
2.5.1 Conservative MHD equations 40
2.5.2 Finite volume method 41
2.5.3 Enforcing the $\nabla \cdot B = 0$ condition 44

3 Heating by transverse waves **47**
3.1 Introduction 48
3.2 Numerical models 51
3.2.1 Equilibrium 51
3.2.2 Grid 53
3.2.3 Driver 53
3.2.4 Boundary conditions 55
3.3 Results and discussion 56
3.4 Conclusions 66

4 Fully deformed loops **69**
4.1 Introduction 70
4.2 Numerical model 71
4.3 Results 72
4.4 Discussion and conclusions 75

5 Wave heating in stratified loops **79**
5.1 Introduction 80
5.2 Numerical model 82
5.2.1 Equilibrium 82
5.2.2 Grid 85
5.2.3 Driver 88

5.2.4 Boundary conditions 88
5.2.5 Forward modelling 90
5.3 Results 90
5.3.1 Loop dynamics and evolution 92
5.3.2 Temperature evolution in cold loops 94
5.3.3 Heating in very viscous cold loops ($R_e = 10^2$) 98
5.3.4 Energy profiles and heating rate 100
5.4 Discussion and conclusions 107

6 Amplitudes of decayless oscillations 113
6.1 Introduction 114
6.2 Material and Methods 116
6.2.1 Basic setup 116
6.2.2 Boundary conditions and driver 117
6.2.3 Numerical method and grid 118
6.2.4 Forward modelling 119
6.3 Results 121
6.4 Discussion 128

7 Conclusions 133

Bibliography 137

Curriculum Vitae 147

Chapter 1

Introduction

"So what is it that you do, again?"
Every scientists' relatives and friends, ever.

In this introductory chapter, we present a small overview of our current understanding of solar physics. We give some basic general information about the Sun, before describing, in short, the solar interior. We then proceed with a more detailed description of the solar atmosphere, as well as a detailed description of coronal loops, providing the necessary context for our research. Finally, we present the coronal heating problem and the different explanations proposed over the years.

1.1 Prologue: What is Astrophysics?

Astronomy (from the greek word $\alpha\sigma\tau\rho o\nu o\mu\acute{\iota}\alpha$) is the study of the laws that regulate the positions and motion of the celestial objects, like the stars in the night sky. As a practice, astronomy's existence spans over a long part of human civilization, evolving from a religious belief during the early human societies to its modern form of astrophysics. With the term *astrophysics* we call the systematic study of the nature of the astronomical objects and phenomena such as the Sun, the stars, the planets, astrophysical jets, supernovas, γ-ray bursts, the cosmic background radiation, and as of 2018, gravitational waves. Astrophysics have started to develop in the nineteenth century, when the first light spectra from the Sun revealed dark lines. The position of these dark lines

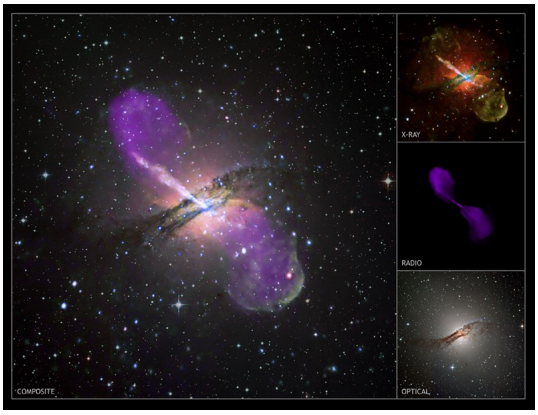

Figure 1.1: Composite image of the Active Galaxy Centaurus A. This view of the galaxy combines image data from the X-ray (Chandra), optical (ESO), and radio (VLA) regimes. Image Credit: Astronomy Picture of the Day, 2008 January 10.

corresponded to the position of known emission spectra from gases. This proved that the same elements found in the Sun, were also found on Earth, and gave birth to the field of astrophysics.

Since the second half of the 20th century, the development of new instruments for observations over a large part of the electromagnetic spectrum has led to a rapid advancement of the field of astrophysics and cosmology. A whole new world, invisible in white light, has been revealed to us through the new technologies (Fig. 1.1). In addition to that, our modern understanding of physics and chemistry, the development of computational methods and the wide spread of advanced computational clusters has allowed us to gain a new insight into the cosmos.

But even before that, astronomy and astrophysics were organically connected to scientific and technological advancement in a slow process lasting from the sixteenth century up to this day. A characteristic example of this is the journey from the geocentric model to the first estimation of the speed of light. The ancient hypothesis of Philolaus and Aristarchus of Samos, that the Sun and not Earth was the center of the universe, had been overshadowed during the Middle Ages by the geocentric model of Ptolemy. When Nicolaus Copernicus published his work on the heliocentric system in 1543, as a more elegant model to explain the motion of the celestial bodies, he lacked any formal proof to support his claim. Using his improved version of the Dutch navy telescope, Galileo Galilei discovered in 1610 the four largest satellites of Jupiter. Deducing that these

Table 1.1: Values of principal physical parameters of the sun from (from Aschwanden 2004).

Physical quantity	Symbol	Value	SI values
Solar radius	$R\odot$	6.96×10^8	m
Solar mass	$M\odot$	1.99×10^{30}	kg
Solar gravitation	$g\odot$	274	m s^{-2}
Solar age	$t\odot$	4.6×10^{10}	years
Astronomical unit	AU	1.5×10^{11}	m
Solar radiant power	$L\odot$	3.9×10^{26}	J s^{-1}
Solar radiant flux density	$F\odot$	6.41×10^7	J m^{-2} s^{-1}
Solar constant (flux at 1 AU)	$f\odot$	1.39×10^3	J m^{-2} s^{-1}
Photospheric temperature	T_{phot}	5762	K

observed objects were revolving around the planet, Galileo had given a strong hint supporting Copernicus' hypothesis, while finding a new application for the telescope. This in turn demanded even further improvement of the instrument, developing the field of modern optics. The work of Johannes Kepler over the elliptical planetary orbits, which expanded Copernicus' hypothesis, lead to Isaac Newton's proposed universal gravity and the inverse-square law of gravitational attraction. Later observations of Jupiter's satellite Io by Cassini and Rømer revealed differences in the duration of Io's eclipses, which hinted towards a finite speed of light. Using this notion, alongside Cassini's and Rømer's data, Christiaan Huygens made the first estimation of the speed of light.

This short story is not only indicative of the interplay between different fields, it also shows how small steps in one 'obscure' field of science can lead to advancements in multiple fields, as well as the everyday life. An initial hypothesis over the place of the Earth in the universe contributed to the eventual improvement of the telescope and optics technology, contributed to the development of classical mechanics and the law of gravity, and eventually led to the first estimation of the speed of light.

1.2 The Sun

Coming back to astrophysics, as in the study of stars, one cannot ignore the closest and most influential star to our everyday lives: the Sun. The Sun, located in the center of the solar system, is a near-spherical ball (Kuhn et al. 2012) of plasma with a radius of around 696,000 km (or 109 Earth radii) and a

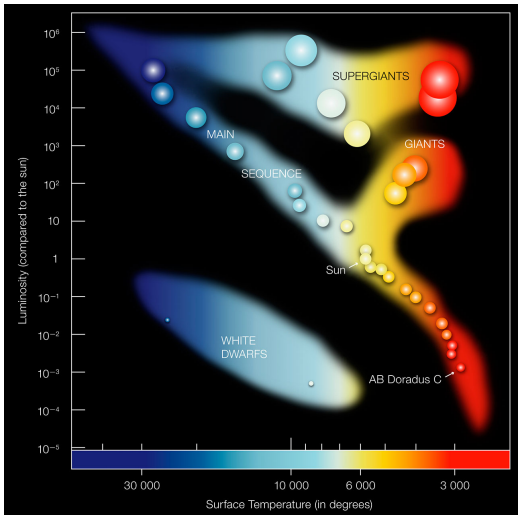

Figure 1.2: A qualitative Hertzprung-Russell diagram, with the position of the sun highlighted. The Hertszprung-Russell (temperature-luminocity) diagram is a representation of stellar evolution. The main sequence consites of stars that burn hydrogen into helium. Additional branches contain giant and supergiant stars, as well as white dwarfs. Credit: ESO, adapted from https://www.eso.org/public/images/eso0728c/.

total mass of $1.99 \cdot 10^{30}$ kg (or 333, 000 Earth masses).

Being the main source of life for all life on Earth, the Sun has been revered as a God by many cultures over the centuries. The ancient Egyptians worshiped Ra as the deity of the sun, and even had the short-lived monotheistic religion of Atenism. In Atenism, the sun disk Aten (or Aton) was praised as the creator and giver of life. Ra was later merged with the creator god Amun (or Amon), creating the creator deity of Amun-Ra. The importance of this deity in the Egyptian pantheon made it popular even outside of Egypt, with the ancient Greeks merging him with the god of the sky, Zeus, worshipping him as Amon-Zeus. The ancient Greek god of the sun was the titan Helios (literally *Sun*) on his flying chariot, who was later replaced with Apollo-Phoebus ("Radiant"). In a similar fashion, the Aztecs had Huitzilopochtli (god of war, sun and *literal* human sacrifice), the Japanese had Amaterasu (goddess of the sun and the universe, ancestor of the emperors of Japan), in Hinduism we see the solar deity Surya (Sun) riding a chariot etc.

Despite its importance for life on Earth, the sun is a rather common type of

star. It is one of approximately 100 billion stars in the Milky Way galaxy, and consists mainly of hydrogen and helium (92.1% and 7.8%, respectively), with small traces of other elements (Pasachoff 2003). It is a G-type (G2V) star based on the Harvard spectral classification system. It has a surface temperature of around 5700 K and is part of the so-called yellow dwarf stars, although its color is closer to white with a spectrum that peaks near blue and green in the visible. Our sun lies at a distance of approximately 150 million km from Earth, the distance that we call one Astronomical Unit (AU).

The sun was formed about 4.6 billion years ago from an cloud of dust and gas, the solar nebula. A fragment of that initial cloud collapsed due to self gravity and accreted into a proto-star, while a spinning disk surrounding it, eventually formed the planets and smaller objects surrounding our sun. The accretion and the gravitational collapse of the initial proto-star continued, compressing the stars core until its temperature reached approximately 15 million K. By that point, the tunneling effect allowed the hydrogen nuclei at the core to overcome the electrostatic barrier (Coulomb repulsion), allowing nuclear fusion. Thus we have 'ignition' and the creation of a new star.

In the Hertzprung-Russel diagram of Fig. 1.2, the sun lies in the diagonal line of the Main Sequence. This means that it is in its stable state, burning hydrogen into helium. In the Hertzprung-Russell diagram (H-R, first created by Ejnar Hertzprung and Henry Norris Russell in 1910) the temperatures of stars are plotted against their luminosities, with the position of a star giving information about its present stage and mass. Stars like our sun lie in the main sequence branch. The H-R diagram also has branches for the end state of the stars. When a star exhausts all the hydrogen, it leaves the main sequence and becomes a red giant or a supergiant, depending on its mass. Stars with the mass of the Sun pass through the stage of a red giant and end up as a white dwarf, after they release their outer layers in the form of a planetary nebula.

The solar interior

The Sun is structured in several distinct layers, as is qualitatively shown in Fig. 1.3. The unique characteristics of each one of these layers is briefly presented, starting from the innermost part of the sun, the *solar core*. The core is the powerhouse of the Sun, with a radius approximately $20-25\%$ of the Sun's total radius and mass equal to 34% of the Sun's mass. Inside the core, energy is produced, mainly through the 'proton–proton chain reaction', which converts hydrogen (H) to helium (He):

$$4\,^1H \longrightarrow^4 He + 2\,e^+ + 2v + 26.7 \quad MeV, \tag{1.1}$$

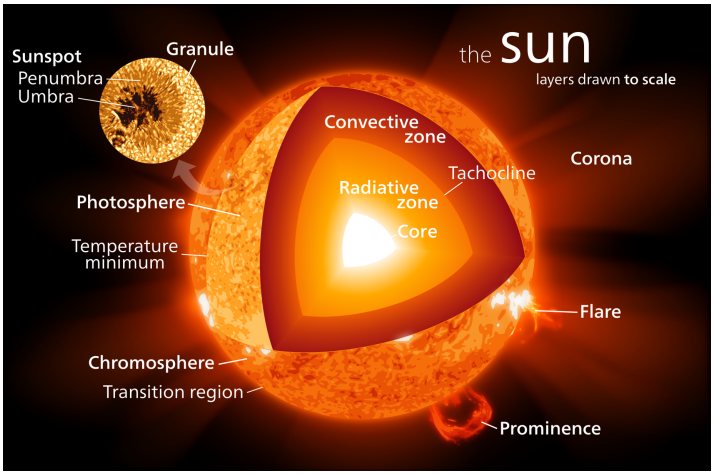

Figure 1.3: Illustration of the structure of the inner Sun and the solar atmosphere: The energy released by nuclear fusion of hydrogen to helium in the Sun's core is transported outwards via radiation. In the outer shell energy transfer is dominated by convection. Layers with different characteristics extend outwards from the solar surface. Credit: Kelvinsong, Wikimedia Commons. https://en.wikipedia.org/wiki/File:Sun_poster.svg

where we also have the production of positrons (e^+), neutrinos (ν) and energy ($1\ \text{eV} = 1.6 \cdot 10^{-19}$ J). The temperature and density inside the core are around 15 MK and $150 \cdot 10^3$ kg m^{-3} at the center and drop to around 7 MK and $20 \cdot 10^3$ kg m^{-3} near the outer layers of the core.

The fusion rate in the core is in a self-correcting equilibrium, meaning that a slightly higher rate would increase the core temperature, forcing it to expand reducing its density and fusion rate, while a slightly lower rate would have the opposite effect. The entirety of the Sun's energy is produced at its core, and then travels outwards, heating the rest of the star.

The layer right beyond the core is the *radiation zone*. From the core out to about 0.7 solar radii, thermal radiation is the primary means of energy transfer. The energy generated in the core is carried by light (photons) that collides with particles through the layer. The temperature drops from approximately 7 million to 2 million kelvins with increasing distance from the core, while the density drops from $20 \cdot 10^3$ kg m^{-3} down to only $0.2 \cdot 10^3$ kg m^{-3}.

The Sun's *convection zone* extends from 0.7 solar radii to its 'surface'. In this layer, the solar plasma is neither dense nor hot enough to transfer the heat

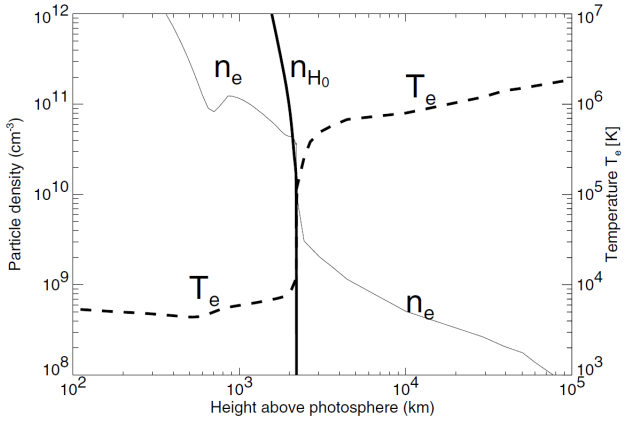

Figure 1.4: Electron density and temperature model of the chromosphere and lower corona. The sharp temperature increase at the solar transition region is shown. The plasma is partially ionized in the chromosphere and becomes fully ionized in the corona. The electron density is n_e and the neutral hydrogen density is n_{H0} Credit: Aschwanden (2004)

energy of the interior outward via radiation. Instead we have the development of convective motions that move the energy outwards, because the radial temperature gradient is larger than the adiabatic gradient (rate of temperature drop for an adiabatic upward movement of a plasma volume).

The transition layer between the radiation and the convection zone is called the *tachocline*. At the tachocline, the uniformly rotating radiative zone meets the differentially rotating convection zone. The Sun's magnetic field is believed to be generated by a magnetic dynamo in this location. The high ratio of gas to magnetic field pressure (plasma$-\beta$) in the convection zone, results in the magnetic field being anchored to the moving plasma, getting transferred by the convective motions. The combination of this magnetic field and the convective motions manifests at the overlaying layers of the solar atmosphere. A detailed description of the physics in the convection zone and the tachocline are presented in Nordlund et al. (2009).

The solar atmosphere: Photosphere

The transition layer between the solar atmosphere and the inner parts of the Sun is the *photosphere* (sphere of light). It is named by the fact that this is the origin of the Sun's observed white light, as most of the observed radiation comes

from this layer. The photosphere can be defined as the region of finite depth where the solar plasma becomes opaque to visible light, moving towards the solar interior. The Sun's photosphere has a temperature range of $4500 - 6000$ K, with an effective temperature of ~ 5700 K, and an approximate width of 100 km. Its density goes from 10^{-3} to 10^{-6} kg m^{-3} the higher up we travel into the solar atmosphere.

The photosphere consists of a granulation pattern caused by the convective flows in the convection zone. The individual cells, or *granules*, have horizontal scales of varying orders, and give the photosphere its characteristic boiling-like observed texture. Granulation consists of cells with scales ~ 1 Mm and a life-span between $8 - 20$ minutes. A typical granule consists of a hotter and brighter ascending region of plasma, and darker sides of colder, descending plasma. When observed through Dopplergrams, the different radial velocities of the different parts of granules are observed. Larger scale flows at the solar atmosphere are classified into mesogranulation ($5 - 10$ Mm), supergranulation ($20 - 50$ Mm) and giant cells (> 100 Mm) (Nordlund et al. 2009).

Another important phenomenon taking place in the solar photosphere is the magnetic field flux through its surface. The emerging magnetic field of the order of kG is connected to the 22-year solar cycle through the Babcock-Leighton dynamo mechanism (Babcock 1961; Leighton 1969). The concentrated magnetic flux in the photosphere is also connected with temporary phenomena like pores, sunspots, and bright spots. The biggest of these are the sunspots. The sunspots are parts of the photosphere that have lower temperature than the surrounding plasma, located in the so called active regions. They are composed of an umbra in the center, surrounded by penumbra, seen at high resolution as bright and dark filaments getting out of the umbra.

One of the most established semi-empirical models for describing the zones of the solar atmosphere above the photosphere is the Vernazza-Avrett-Loeser (VAL) model (Vernazza et al. 1981). This model is obtained from the determination of the temperature and density stratifications, and it gives us a basic understanding of the solar atmosphere, by considering it static (Fig. 1.4). However, the solar atmosphere is a temporally and spatially dynamic area, with structures of inhomogeneous and non-equilibrium plasma deviating from the basic density and temperature of the static model (Wedemeyer-Böhm et al. 2009).

The solar atmosphere: Chromosphere

The *chromosphere* ('sphere of color', from $\chi\rho\acute{\omega}\mu\alpha$) is the layer right above the photosphere, extending up to 2.5 Mm. Its name derives from the red colour that is apparent during eclipses. The density of the chromosphere goes from

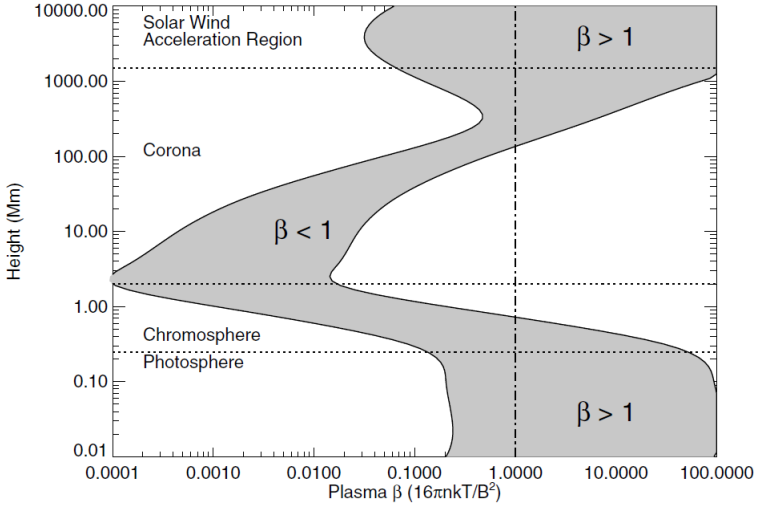

Figure 1.5: Plasma β in the solar atmosphere for two assumed field strengths, 100 G ($\beta > 100.$) and 2500 G ($\beta > 0.2$). In the solar chromosphere, transition region and corona the plasma is magnetically dominated ($\beta < 1$), following the motion and morphology of the magnetic field. Credit: Aschwanden (2004)

10^{-3} to 10^{-11} kg m^{-3}, while its temperature decreases from the inner boundary of about 6000 K to a minimum of approximately 3800 K, before increasing to the order of 10^4 K at its outer boundary.

Its low density, and the brightness of the underlying photosphere do not allow us to properly view the chromosphere in visible light, unless in the case of a full solar eclipse. The higher ionization level of plasma in the chromosphere leads to its spectrum consisting of emission lines.

By defining the gas pressure over the magnetic pressure as β (see Chapter 2 for a more detailed definition), we see in Fig. 1.5 that in the chromosphere $\beta < 1$. The magnetic pressure in the chromosphere is higher than the gas pressure, meaning that the plasma there is magnetically dominated. The magnetic field of the underlying photosphere extends upward into the chromosphere, creating various structures connected to those in the layer below. Observations in lines, such as CaII and Hα, show magnetic structures like the chromospheric network, spicules and fibrils.

The chromospheric network is the extension of the photospheric network, being connected with supergranulation (Simon & Leighton 1964). The most common

feature is the presence of spicules and fibrils (De Pontieu et al. 2007a; Pasachoff et al. 2009; Judge et al. 2011; Skogsrud et al. 2014). Spicules are small jet-like structures, seen in chromospheric spectral lines in the solar limb. These structures drive plasma into the solar corona with high velocities, with a temperature of $5000 - 15000$ K and a duration of around 10 minutes. The fibrils seem to be the equivalent structures observed on the solar disk, and are associated to the underlying magnetic flux concentrations (Rouppe van der Voort et al. 2009).

The solar atmosphere: Corona

The outermost layer of the solar atmosphere is the *solar corona*. The Sun's corona (Latin, 'crown') extends millions of kilometres from the solar surface, with its outer parts being expelled away from the Sun in the form of the *solar wind*. The corona can be observed in visible light during the total solar eclipses, where a 'crown' of light is seen surrounding the Sun and the overlapping Moon.

The light of the corona comes from three primary sources, i.e. sunlight scattering off free electrons (K-corona), sunlight bouncing off dust particles (F-corona) and spectral emission lines produced by ions present in the coronal plasma (E-corona). The extreme ultraviolet emission from the E-corona reveals plasma temperatures of the order of 10^6 K, which is three orders of magnitude higher than the temperatures of the photosphere (first observations by Grotrian 1939; Edlén 1943). The plasma in the solar corona is fully ionized, while the magnetic pressure dominates over the gas pressure ($\beta < 1$). This results in the plasma being confined inside magnetic flux tubes, anchored to the underlying photosphere.

The *transition region* is a thin layer ($\sim$ 200 km) located between the chromosphere and the overlying corona. The temperature shows a very steep increase in this layer, going from chromospheric (10^4 K) up to coronal (10^6 K) temperatures. The transition region consists of a highly dynamic plasma, and does not occur at a well-defined altitude. Instead, it forms a 'nimbus' around chromospheric features such as spicules.

The solar corona is of particular interest to us, since it is directly connected with the solar wind and with space weather. The corona is not a static layer, but is instead filled with non-uniform plasma, and is dependent on the solar cycle. Qualitatively, we can separate the corona in coronal holes, active regions and the quiet Sun.

During periods of low magnetic activity (Solar minimum) we can see extended coronal holes covering the polar regions. Coronal holes are areas of low-density

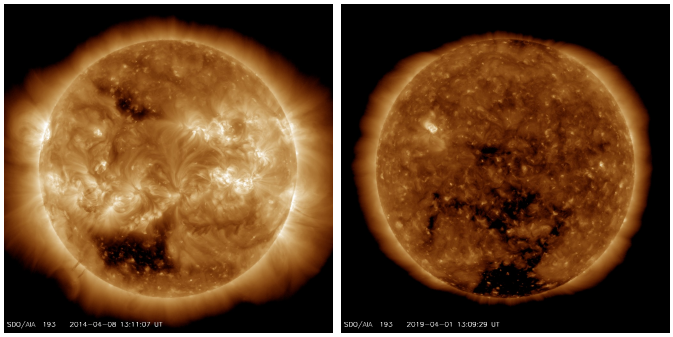

Figure 1.6: Images of the solar corona in the 193 Å channel, from the SDO AIA. *Left panel*: picture taken during the solar maximum of April 2014. *Right panel*: picture taken during the beginning of the new cycle (April 2019). Credit: SDO data (https://sdo.gsfc.nasa.gov/data/aiahmi/)

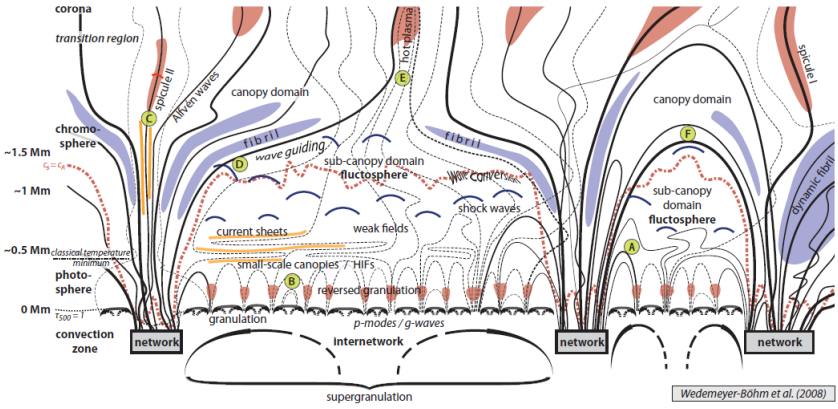

Figure 1.7: Simplified schematic reconstruction of the lower solar atmosphere. With bold black lines we see the magnetic field, anchored in the convection zone, extending through the photosphere up to the chromosphere and the lower corona. Credit: Wedemeyer-Böhm et al. (2009)

plasma, located in open magnetic field regions[1]. Coronal holes are the source of the fast solar wind (for a review see Cranmer 2002), and they are the site of different phenomena such as jets (Moreno-Insertis & Galsgaard 2013) and polar plumes (Wilhelm et al. 2011).

[1]The unipolar field lines connect from the solar surface directly to interplanetary space.

During the solar maximum, the active region corona is prominent over regions with increased sunspot activity (Fig. 1.6). Because of the low plasma β, the active region corona is dominated by the magnetic field structures emerging from the lower layers. In the active region corona we can observe the manifestation of the magnetic field in the form of coronal loops, which represent the connection between regions of different polarity, as we will see in the following section. Other important structures are the prominences and filaments, which are essentially one and the same phenomenon, observed at different line of sight (LOS) angles. Prominences are often treated as chromospheric phenomena due to their chromospheric-level temperatures, are usually connected with emerging magnetic flux ropes, and are observed in the same lines as the chromosphere.

An important aspect of the active region corona is magnetic reconnection. Magnetic reconnection is the topological restructuring of the magnetic field, which leads to particle acceleration and turns magnetic field energy into thermal and kinetic energy. Reconnection is responsible for flares, highly energetic phenomena that give strong X-ray emission. Connected with the active region corona are also Coronal Mass Ejections (CMEs), which are considered to be the main drivers of space weather (Koskinen & Huttunen 2006). Other phenomena connected to active regions are the coronal streamers, which are regions of open magnetic field near the equator, caused by magnetic reconnection above active regions.

By definition, the quiet solar corona is the part of the coronal plasma not included in coronal holes or active regions. During the solar minimum, it is confined near the solar equator, but it expands to greater parts of the solar atmosphere during the solar maximum.

We need to stress here that the solar atmosphere is a very dynamic and inhomogeneous multi-scale system. The traditional view of the clearly defined layers at specific heights, and with specific properties, is questioned in light of modern studies and observations (Wedemeyer-Böhm et al. 2009; Peter et al. 2014). The solar magnetic field, generated in the convection zone, emerges through the photosphere, forming active regions and deforming granules. The active region magnetic field extends upwards through the chromosphere and the lower corona, creating different structures at each layer (Fig. 1.7), and eventually connecting these different layers.

The solar atmosphere: Coronal loops

Coronal loops are some of the basic structures of the solar corona and transition region, and are the emitting manifestation of the coronal magnetic field. These loops appears more prominent in the active region corona (Fig. 1.8), where the

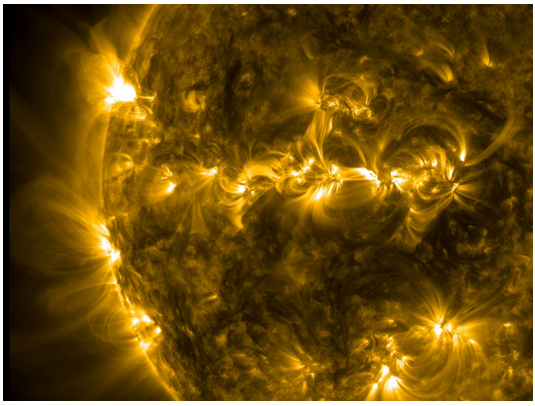

Figure 1.8: A series of active regions were all lined up one after the other as they rotated into view over three days ($\sim 24^{th}$ of September 2012). Image taken at the 171 Å channel of AIA instrument of SDO. Credit: SDO gallery (https://sdo.gsfc.nasa.gov/gallery/main/item/161)

magnetic field is expected to be the strongest. For a review on the observation and modelling of such systems, the reader may refer to Reale (2014).

Since coronal loops are anchored below the photosphere and extend up to the lower corona, they are effectively connecting the atmospheric layers that they cross. This makes them ideal environments to study the transfer of energy between the different layers of the solar atmosphere. Observations of active regions in the EUV and X-ray band from observatories like SOHO, Hinode, TRACE and SDO/AIA reveal temperatures of $\log T \geqslant 6.5$ for plasma confined into compact loops (Testa & Reale 2012). These observations guide the study of coronal heating towards areas of structured magnetic fields.

Coronal loops often form arches, which is a typical shape of magnetic field topology, and display a near constant cross-section along their length (Peter & Bingert 2012), above the transition region. Loops are often classified with respect to their temperature as *cool* ($0.1 - 1$ MK), *warm* ($1 - 1.5$ MK) and *hot* (> 2 MK) loops, with flaring loops going as hot as > 10 MK. Earlier classifications involved the environments where they were detected (bright points, active-region loops etc.). The length of coronal loops spans over three orders of magnitude (between 1 and 1000 Mm, for bright point loops and giant arches respectively), and their densities range between 10^{14} m^{-3} up to 10^{18} m^{-3} for flaring loops Reale (2014).

A phenomenon connected to coronal loops is *coronal rain*. Coronal rain consists

of cool dense plasma 'blobs' that form, due to competition between heating and radiative cooling, in warm active region loops and later fall along the magnetic field (Schrijver 2001; Vashalomidze et al. 2015; Antolin et al. 2015; Xia et al. 2017). Due to their lower temperatures they are usually observed in chromospheric and transition region lines, but they can also be observed in absorption in EUV spectra.

Extensive studies have been performed over the fine structure of coronal loops, trying to reveal their, often under-resolved, thermal and spatial structure (Reale & Peres 2000; Peter & Bingert 2012; Antolin & Rouppe van der Voort 2012; Goddard et al. 2017). Studies with models of such multi-stranded coronal loops have managed to explain some observed properties like the near constant cross-section (Peter & Bingert 2012), while the propagation of energy with waves in such systems has been considered by Van Doorsselaere et al. (2008, 2014a). Peter et al. (2013) have argued that the loop substructure should have a scale below 15 km, without excluding the possibility of monolithic loop profiles (i.e. no sub structure), while a numerical study by Magyar & Van Doorsselaere (2016) has proven the variable nature of such systems in the presence of propagating waves.

Other numerical studies of coronal loops have shown the development of Kelvin-Helmholtz instability (KHI) from strong shear velocities at the loop boundary layers (Terradas et al. 2008; Magyar & Van Doorsselaere 2016; Karampelas et al. 2017), affecting their characteristics (Goddard et al. 2018). The KHI was found to lead to the manifestation of strand-like structures in synthetic images (Antolin et al. 2014) despite the initially monolithic loop cross-section. Additional studies for footpoint driven loops (Karampelas & Van Doorsselaere 2018; Karampelas et al. 2019a; Guo et al. 2019b) have shown that the KH induced turbulent layer spreads across the loop cross-section, fully deforming it. These results complement those from Magyar & Van Doorsselaere (2016), indicating that we should not expect the existence of loops that remain monolithic or multi-stranded throughout their lifetime.

The solar atmosphere: Waves in the solar corona

The solar corona contains a large ensemble of structures that are sites of oscillations and waves. Observations from the Coronal Multi-channel Polarimeter (CoMP), the Solar Dynamics Observatory (SDO) spacecraft, STEREO (Solar Terrestrial Relations Observatory) and the Hinode Solar Observatory have revealed the existence of ubiquitous transverse perturbations along coronal loops, prominence threads and greater areas of the corona. For a

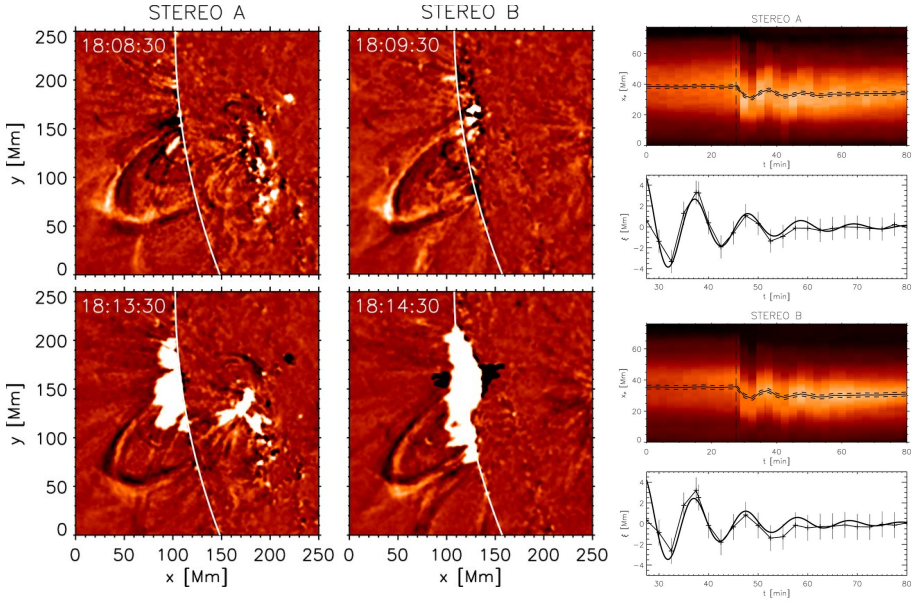

Figure 1.9: Adapted from Verwichte et al. (2009): On the left we have four panels from the STEREO spacecrafts, showing the intensity of the NOAA 10962 active region loop. The pattern indicates the existence of the transverse oscillation. On the right we show time-distance maps of the oscillating loops from STEREO, and the respective detrended oscillation amplitudes. Fitted are the profiles of a damped oscillation.

review on the observations of waves and their application to the field of coronal seismology, the reader is referred to De Moortel & Nakariakov (2012).

Some of the first observations of coronal loop oscillations were made in the EUV with the Transition Region and Coronal Explorer (TRACE) observatory. These were standing transverse (kink) oscillations in coronal loops (Aschwanden et al. 1999; Nakariakov et al. 1999), which showed a damping profile over time. Additional observations have proved the common nature of these phenomena not only in coronal loops (e.g. Aschwanden et al. 2002; Schrijver et al. 2002; Verwichte et al. 2004, 2009, 2010; White & Verwichte 2012; White et al. 2012) but also in prominence threads (e.g. Okamoto et al. 2007, 2015), and they have connected these oscillations with very energetic phenomena (i.e. flares) in active regions (see Fig. 1.9).

Another category of transverse waves observed in the lower solar corona is that of propagating transverse waves. The ubiquitous nature of these waves in the

solar atmosphere have been proven through observations by CoMP (Tomczyk et al. 2007; Tomczyk & McIntosh 2009). These quasi-periodic fluctuations were interpreted as field-aligned incompressible propagating Alfvén waves, and were observed both for open and close magnetic field lines. In Tomczyk et al. (2007) it was also suggested that these waves may carry enough energy to support the energy losses from the Quiet Sun (Withbroe & Noyes 1977). Additional observations (McIntosh et al. 2011; Morton & McLaughlin 2013; Morton et al. 2016) have also shown that propagating transverse waves are a common phenomenon in coronal loops and greater parts of the solar corona.

Alongside the high amplitude, externally initiated, decaying transverse oscillations in coronal loops, a new group of small-amplitude decayless transverse oscillations waves have been identified in coronal loops (Nisticò et al. 2013; Anfinogentov et al. 2013, 2015). These oscillations (Fig. 1.10) have amplitudes between $\sim$ 0.1-0.4 Mm, smaller than the average amplitudes in decaying oscillations, and they have not yet been connected with any external excitation mechanism. These loop oscillations where found by Nisticò et al. (2013) to have periods similar to those of standing large-amplitude oscillations, while recent analysis has proven the existence of higher harmonics (Duckenfield et al. 2018).

Although this study is focused on transverse waves, other wave modes are also observed in the solar corona and the solar atmosphere in general. In Jess et al. (2009), observations of torsional Alfvén waves in the photosphere and chromosphere has been hypothesised to transfer energy into the lower corona. Observed oscillations propagating along coronal loops have been interpreted as slow magnetosonic waves by (Berghmans & Clette 1999; De Moortel et al. 2000), with additional identifications along active region loops been made by Krishna Prasad et al. (2012a). Observations of standing slow modes in coronal loops have been also reported (e.g. Wang et al. 2003b,a; Mariska 2006). Propagating slow waves have are also observed in open coronal structures (DeForest & Gurman 1998; Krishna Prasad et al. 2012b, 2014, 2015). Propagating disturbances have also been observed in plumes by Pant et al. (2015). Liu et al. (2011) have interpreted detected propagating oscillations in the lower corona as fast magnetosonic waves, while fast sausage modes have been observed in the solar chromosphere, and have been suggested to carry energy into the solar corona (Morton et al. 2012).

The importance of waves and oscillations in the solar atmosphere is two-fold. Through the methods of coronal seismology, they can provide us with valuable information on the characteristics of plasma structures in the solar atmosphere (Nakariakov & Ofman 2001; Aschwanden et al. 2003), using the theory of MHD waves and the damping mechanisms of resonant absorption and phase mixing. At the same time, the aforementioned mechanisms are important for the study of energy dissipation and wave heating, all of which will be described in the

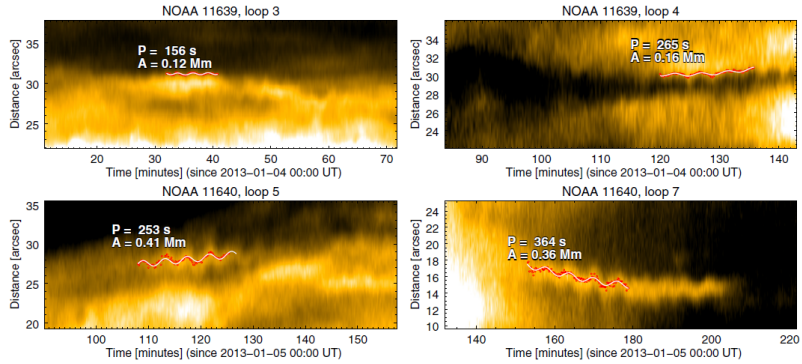

Figure 1.10: From (Anfinogentov et al. 2015): Time-distance maps of decayless loop oscillations found in the analysed active regions (here shown for NOAA 11639 and NOAA 11640). The oscillations are fitted with a sine function (white curves), while red dots indicate the positions of the loop centres estimated by the Gaussian fitting. Also included in the panels are the periods and amplitudes of the detected oscillations.

next chapter.

Observational studies of transverse and torsional waves in the solar chromosphere and corona (De Pontieu et al. 2007b; Tomczyk & McIntosh 2009; Morton et al. 2012; Jess et al. 2009) suggest the existence of enough energy flux to sustain the radiative losses of ~ 100 W m^{-2} for the non-active region corona (Withbroe & Noyes 1977). This makes these waves candidates for a heating mechanism in the solar atmosphere. A debate exists over the capabilities of these waves to heat the solar corona, with recent numerical studies (Pagano & De Moortel 2017; Pagano et al. 2018; Pagano & De Moortel 2019) reporting the lack of sufficient energy, while other studies suggesting the possibility of additional underlying energy, hidden through LOS effects (De Moortel & Pascoe 2012; Antolin et al. 2017).

The solar atmosphere: Coronal heating

One of the open questions regarding the nature of the solar atmosphere is explaining its very high temperatures. The high temperatures ($> 10^6$ K in the corona) are up to three orders of magnitude higher than those in the photosphere, as we see in Fig. 1.4. This behaviour contradicts our everyday experience where temperature is supposed to get lower the further away we are from a heating

source, which would be the solar core. This phenomenon is puzzling scientists for many decades and is commonly known as the coronal heating problem.

In the context of the coronal heating problem, it is of great importance to identify the heating source(s) that are able to balance losses owing to thermal conduction and radiation. As it was already mentioned, the magnetic field dominates the dynamics of the lower solar corona ($\beta < 1$), creating plasma structures like coronal loops. Thus, the coronal heating models are associated with the evolution of the magnetic field. Coronal heating models are usually classified into direct current (DC) and alternating current (AC) models.

In DC models like Ohmic dissipation of current sheets and magnetic reconnection, the evolution of the magnetic field happens over time scales large enough for the coronal structures, such as loops, to adjust in a quasi-static way, leading to explosive reconfigurations. Heating is induced by magnetic field braiding in timescales much larger than the Alfvén crossing time along a coronal loop (Parker 1988; Cargill & Klimchuk 2004; Klimchuk 2006; Chitta et al. 2018). Thus, the coronal currents are almost direct ones. On the other hand, alternating current models focus on mechanisms with dynamic timescales that are shorter than the Alfvén crossing time along a coronal loop, forcing coronal structures to see an alternating current. The two main AC mechanisms consist of wave energy dissipation models (Hollweg 1981; Ofman et al. 1994a; Pagano & De Moortel 2017; Pagano et al. 2018) and Alfvén wave induced turbulence (van Ballegooijen et al. 2014, 2017; Magyar et al. 2017). For a review on the different heating mechanisms of the solar atmosphere, the reader can refer to Arregui (2015) and De Moortel & Browning (2015).

An additional mechanism, acting alongside other DC and AC mechanisms, is the non-linear mode conversion from Alfvén waves and Alfvénic turbulence. In models by Martínez-Sykora et al. (2017), reconnection at photospheric heights combined with a slingshot effect by the Lorentz force leads to the creation of strong slow mode shocks. This is forcing plasma to move upwards, while heating it to transition region and coronal temperatures. This can potentially explain the formation and fast propagation of type II spicules (De Pontieu et al. 2017b), sending plasma into the transition region and corona, as well as the observations hinting to plasma heating in these spicules to coronal temperatures (De Pontieu et al. 2017a).

Traditionally, coronal heating modelling on large scales has been studied within the MHD framework. This sets limitations on these studies, since any effective dissipation mechanism must involve processes on much smaller scales, at which the fluid approximation is no longer valid. However, this makes quantitative results potentially inaccurate. Simple MHD models can be used to provide qualitative results, such as the location of heating and its dependence upon the

dissipation coefficients. The MHD approach can also be used to describe the proposed DC and AC mechanisms, providing the necessary insight to explain the observations.

During this PhD we focused on the study of wave heating mechanisms, and in particular dissipation from footpoint driven oscillations in coronal loops. The rest of the chapters in this thesis are devoted to the presentation of our past work on this subject. In Chapter 2, we present the MHD theory, and we give a basic description of the different wave modes in straight flux tubes. We also present the numerical tools that we used during our studies. In Chapter 3, we present the our simulation results over wave heating in straight flux tubes, focusing on different temperature configurations. In Chapter 4, we address the problem of spatial confinement of wave heating at the loop edges, for dynamically evolving flux tubes. The results of Chapters 3 and 4 are expanded in Chapter 5, where gravity and additional dissipation coefficients were considered. Chapter 6 contains a parameter study, focusing on the connection between the strength of a driver and the obtained spectra and oscillation amplitudes from synthetic data, that we created through forward modelling. The final remarks of this thesis are presented in the Conclusions.

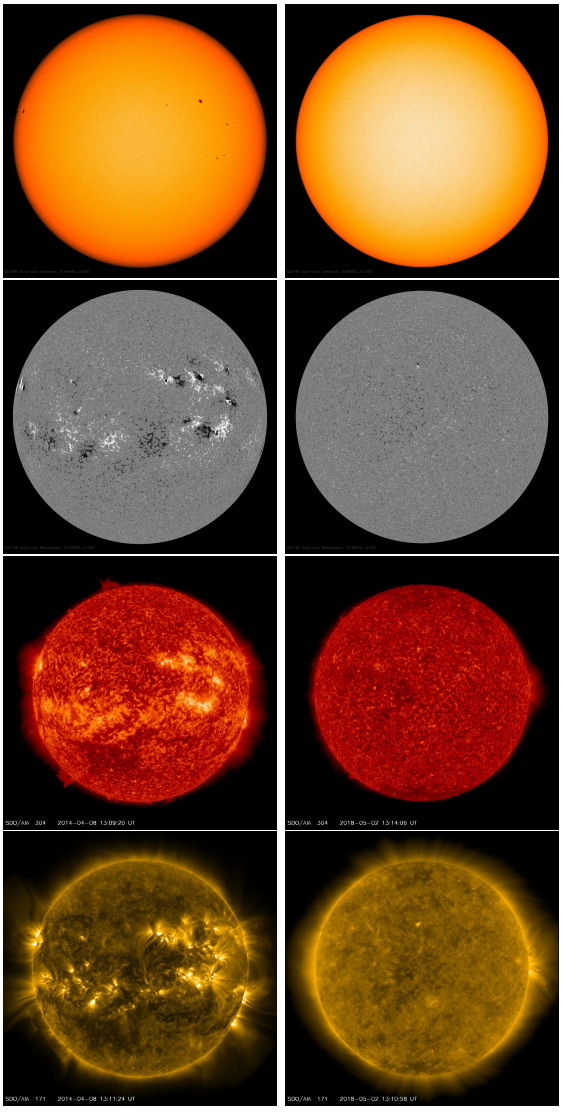

Figure 1.11: Images of the sun at different wavelengths with SDO. From top row to bottom: Intensitygram (photosphere), magnetogram (photosphere), 304 Å (chromosphere and transition region), 171 Å (quiet Sun). *Left column*: At the solar maximum (April 2014). *Right column*: Approaching the solar minimum (May 2018). Credit: SDO data (https://sdo.gsfc.nasa.gov/data/aiahmi/)

Chapter 2

MHD theory and numerical methods

"I know that I know nothing"
The Socratic Paradox

This chapter deals with the theory of MHD waves, as well as the numerical methods employed in our studies. More specifically, we present the theory of magnetohydrodynamics as well as the basic assumptions used for its derivation. Following that, we present the theory of MHD waves for uniform and non-uniform plasmas, introducing the different modes, and the damping mechanisms of resonant absorption, phase mixing and the KHI. Finally, we briefly discuss the numerical methods in the form of the different codes and numerical schemes used during our studies.

2.1 Prologue

A partially or fully ionised gas, known as plasma, is considered the fourth state of matter, after solid, liquid and gas. It is estimated that 99% of the observed matter in the universe is found in this state. In the context of solar physics, the study of plasma is the cornerstone of most of the theories currently in use. The solar interior is composed of a fully ionised plasma, while the solar atmosphere is composed of plasma with different degrees of ionisation for each different layer. In the environment of the solar atmosphere, as well as in the convection

zone, the magnetic field is interconnected with the evolution of the ionised gas. In the solar atmosphere specifically, the magnetic field is of extreme importance when it comes to the evolution of plasma dynamics. The low plasma β (< 1), or ratio of the gas over the magnetic field pressure, means that the magnetic field guides the ionised gas, confining it into structures, such as coronal loops.

There are different approaches in describing an ionised gas, for instance the kinetic theory, the magnetohydrodynamics (MHD) and the two-fluid theory. The kinetic theory is relying on microscopic physics, while the MHD theory treats plasma as a fluid. The two-fluid approach treats the neutral plasma as a combination of two different fluids, usually of electrons and protons. The fluid approach of MHD can be derived from the kinetic theory through statistical (average) quantities.

The kinetic approach can describe the physics of magnetised plasma with minimum assumptions, but at the cost of high complexity. Apart from being more complex analytically, the computational cost of numerical methods based on the kinetic approach is prohibiting for simulations of large scale environments, like those expected in the solar corona. On the other hand, the more accessible and cost effective MHD theory breaks down for scales close to the Debye length, which is the maximum distance at which an electron can effectively "feel" the electrostatic forces from a single proton, before the spatial distribution of charge in the plasma "hides" it.

A plasma can be defined as a fluid, if there are frequent enough collisions between the ions for them to reach local thermodynamic equilibrium much faster than the typical macroscopic time scales. In the solar corona, the typical collision time is $\sim 10^{-3}$ s (Goedbloed & Poedts 2004), which is less than the macroscopic observed time scales in the order of seconds. If we define the Debye length (λ_D) and the electron plasma frequency (ω_p, which is the electrostatic oscillation frequency of an electron in a plasma) as

$$\lambda_D = \left(\epsilon_0 \frac{k_B T}{n e^2} \right)^{1/2},$$

and

$$\omega_p = \left(\frac{n e^2}{\epsilon_0 m^2} \right)^{1/2},$$

then the fluid description of plasma is valid for spatial (l) and temporal (t) scales:

$$l \gg \lambda_D, \qquad \text{and} \qquad t \gg 2\pi\omega_p^{-1}.$$

For a more detailed description see Goedbloed & Poedts (2004). If we consider some typical coronal values for the temperature ($T = 10^6$ K) and the electron

number density ($n = 10^{15} m^{-3}$) we obtain a Debye length of $\lambda_D \sim 10^{-3}$ m and a period for the electron plasma oscillation of $2\pi\omega_p^{-1} \sim 10^{-9}$ s. Other typical kinetic scales, like the ion gyroradius (R_{gi}) and the inverse of the ion gyrofrequency (f_{gi}^{-1}) are in the order of meters and sub-milliseconds respectively (Aschwanden 2004). Given that the typical length and observed dynamical time scales in the solar corona are in the order of a few Mm and a few seconds respectively, we deduce that the fluid description of plasma is justified in the solar corona.

2.2 MHD equations

In the context of this thesis, we will study the solar plasma macroscopically, meaning that we treat it as fluid in the presence of electromagnetic fields. We will describe it with the combined use of the Navier-Stokes hydrodynamic equations, Maxwell's theory of electromagnetism and Ohm's law. For a detailed description of the kinetic, two-fluid and MHD theory, and for the derivation of the MHD equations we refer the reader to chapters 2, 3 and 4 of Goedbloed & Poedts (2004).

Three additional hypotheses that we consider for the MHD description of a magnetised plasma are

- we have a quasi-neutral plasma: $|n_e - Zn_i| \ll n_e$,
- the relative velocity of electrons (e) to ions (i) is a lot smaller than the plasma bulk velocity: $|\upsilon_e - \upsilon_i| \ll \upsilon$,
- the plasma bulk velocity is non-relativistic $\upsilon \ll c$, and

The above hypotheses gives us an electrically neutral electron-ion plasma, where currents can still to exist, and the plasma moves as a strongly coupled fluid.

2.2.1 Contribution from electromagnetism

Starting from the *Maxwell's equations* from the theory of electromagnetism, we have Poisson's equation for the electric and magnetic field, Faraday's law and Ampere's (modified) law:

$$\nabla \cdot \boldsymbol{E} = \tau_e / \epsilon_0, \tag{2.1}$$

$$\nabla \cdot \boldsymbol{B} = 0, \tag{2.2}$$

$$\frac{\partial \boldsymbol{B}}{\partial t} + \nabla \times \boldsymbol{E} = 0, \tag{2.3}$$

$$\mu_0 \epsilon_0 \frac{\partial \boldsymbol{E}}{\partial t} - \nabla \times \boldsymbol{B} = -\mu_0 \boldsymbol{J}, \tag{2.4}$$

where $\boldsymbol{E}$ and $\boldsymbol{B}$ are the electric and magnetic fields respectively, ϵ_0 is the permittivity of the vacuum, μ_0 is the magnetic permeability of empty space, $\boldsymbol{J}$ is the current density and τ_e is the charge density. The permittivity and magnetic permeability are connected with the speed of light $c = (\epsilon_0 \mu_0)^{-1/2}$.

Equation 2.1 states that an electric charge can be a source for an electric field, while equation 2.2 states that there are no magnetic charges (also known are magnetic monopoles). However, in a quasi-neutral plasma, the electric field cannot be produced by electric charges, but is instead created by temporal variation of the magnetic field (Eq. 2.3). Equation 2.4 states that a magnetic field can be generated from a time variant electric field and from non-zero currents.

In the non-relativistic limit ($v \ll c$) Eq. 2.3 gives us a quantitative relation between $\boldsymbol{E}$ and $\boldsymbol{B}$:

$$\frac{B}{t} \sim \frac{E}{l}.$$

Applying the same limit on the modified Ampere's law we get:

$$\frac{\mu_0 \epsilon_0 \dfrac{\partial \boldsymbol{E}}{\partial t}}{\nabla \times \boldsymbol{B}} \sim \frac{E/t/c^2}{B/l} \sim \frac{l^2/t^2}{c^2} \sim \frac{v^2}{c^2} \ll 1.$$

This means that the leftmost term of Eq. 2.4 is significantly smaller than the second term on the left side, and is thus taken as zero. Eq. 2.4 can now be rewritten as

$$\nabla \times \boldsymbol{B} = \mu_0 \boldsymbol{J}. \tag{2.5}$$

If we consider the current density $\boldsymbol{J}$ and the electric field $\boldsymbol{E}$ from Maxwell's equations, we can rewrite Ohm's law as:

$$\boldsymbol{J} = \sigma \boldsymbol{E} \iff \boldsymbol{E} = \eta_{\mathrm{r}} \boldsymbol{J},$$

where σ is the conductivity of the given plasma and η_{r} is the electrical resistivity. If the considered plasma moves in the presence of magnetic fields, then the electric field in the rest frame of the material $\boldsymbol{E'}$ is connected to the electric field in the lab frame through the relation $\boldsymbol{E'} = \boldsymbol{E} + \boldsymbol{v} \times \boldsymbol{B}$. Then, the generalised Ohm's law can be rewritten as:

$$\eta_{\mathrm{r}} \boldsymbol{J} = \boldsymbol{E} + \boldsymbol{v} \times \boldsymbol{B}. \tag{2.6}$$

By combining the generalised Ohm's law with the non-relativistic version of Ampere's law, the Faraday's law and Eq. 2.2, we end up with the *induction equation*:

$$\frac{\partial \boldsymbol{B}}{\partial t} = \nabla \times (\boldsymbol{v} \times \boldsymbol{B}) - \frac{\eta_{\rm r}}{\mu_0} \nabla^2 B, \tag{2.7}$$

where we have considered $\eta_{\rm r}$ to be uniform. The first term on the right hand side of the equation (advective term) of the equation couples the magnetic field with the motion of the plasma, while the second or diffusive term describes the break of this coupling, due to resistivity. If we make a dimensional analysis of the ratio of the advective over the diffusive term, we get the dimensionless *magnetic Reynolds number*:

$$R_m = \frac{\mu_0 l v}{\eta_{\rm r}}, \tag{2.8}$$

where l is the characteristic length of the system and v is the characteristic velocity of the system. For $R_m \gg 1$, the plasma acts as fully ideal, and we can neglect diffusive phenomena such as reconnection. For $R_m \ll 1$ then diffusive effects cannot be ignored. In the solar atmosphere, the magnetic Reynolds number is very high, with the exception of very thin plasma structures, like current sheets.

2.2.2 Fluid equations

The first of the fluid equations used in MHD describes the *continuity, or conservation of mass* in a system:

$$\frac{\partial \rho}{\partial t} + \nabla \cdot (\rho \boldsymbol{v}) = 0, \tag{2.9}$$

where ρ is the density and $\boldsymbol{v}$ is the velocity vector.

The balance of forces is given by the *equation of motion, or (near) conservation of momentum*:

$$\rho \left(\frac{\partial}{\partial t} + \boldsymbol{v} \cdot \nabla \right) \boldsymbol{v} + \nabla p + \frac{\nabla B^2}{2\mu_0} - \frac{(\boldsymbol{B} \cdot \nabla)\boldsymbol{B}}{\mu_0} = -\rho \nabla \Phi + \boldsymbol{F}_{visc} + ..., \tag{2.10}$$

where $B^2 \left(2\mu_0\right)^{-1}$ is the magnetic pressure and $\mu_0^{-1} \boldsymbol{B} \cdot \nabla(\boldsymbol{B})$ is the magnetic tension. The force from the magnetic pressure is oblique to the magnetic field lines, and is directed towards lower field strengths. The magnetic tension can be rewritten as $B^2 \hat{n} (\mu_0 R_c)^{-1}$, where R_c is the local radius of curvature for the field lines and $\hat{n}$ is the unit vector normal to the field.

On the right side of the equation we also have source terms, such as gravity $-\rho\nabla\Phi$ and viscosity (Goedbloed & Poedts 2004):

$$\boldsymbol{F}_{visc} \approx \nu\rho\left[\nabla^2\boldsymbol{v} + \frac{1}{3}\nabla\nabla\cdot\boldsymbol{v}\right],$$

where ν is the kinematic viscosity coefficient ($\mathrm{m}^2\ \mathrm{s}^{-1}$).

By following the same method as for the magnetic Reynold's number, we define the regular *Reynold's number*, as the ratio of the inertia over the viscous term:

$$R_e = \frac{\upsilon^2/l}{\mu\upsilon/l^2} = \frac{l\upsilon}{\mu}, \tag{2.11}$$

where μ is the coefficient of dynamic viscosity.

Finally, the ratio of gas over magnetic pressure gives us the plasma β parameter:

$$\beta = \frac{p}{B^2/(2\mu_0)}, \tag{2.12}$$

which shows us the dominant term between the magnetic field pressure and the gas pressure. When $\beta > 1$, the plasma dynamics dominate over the evolution of the magnetic field, as is the case in the solar convection zone, photosphere and lower chromosphere, as well as the solar wind (Fig. 1.5). When $\beta < 1$, the magnetic pressure is stronger than the gas pressure, and the plasma is shaped along the magnetic field lines, as is the case in the upper chromosphere, TR and solar corona (i.e. coronal loops).

We also have the equation of *energy conservation*:

$$\frac{\partial p}{\partial t} + \boldsymbol{v}\cdot\nabla p + \gamma p\nabla\cdot\boldsymbol{v} = \nabla\cdot(\boldsymbol{B}\times\eta\boldsymbol{J}) + Q, \tag{2.13}$$

where $\gamma = 5/3$ is the ratio of specific heats in the non-relativistic case. On the right-hand side of the equation we may consider various terms, describing effects like resistive heating, radiative losses, thermal conduction etc.

Finally, we need an *equation of state*, in order to close the MHD equations. For the duration of this thesis, we consider the equation of ideal gas which simplifies our calculations and is a valid approximation for the high temperature plasma found in the solar atmosphere.

$$p = \rho\frac{k_B}{m}T, \tag{2.14}$$

where $k_B = 1.38\,10^{-23}$ kg m^2 s^{-2} K^{-1} is the Boltzmann constant, and m is the average particle mass.

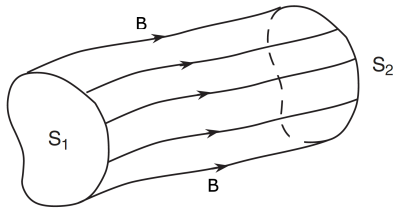

Figure 2.1: A magnetic flux tube. Credit: Figure adapted from Goedbloed & Poedts (2004).

2.2.3 The complete system

One form of the system of the MHD equations is presented in short as follows:

$$\frac{\partial \rho}{\partial t} + \nabla \cdot (\rho \boldsymbol{v}) = 0, \tag{2.15}$$

$$\rho \left(\frac{\partial}{\partial t} + \boldsymbol{v} \cdot \nabla \right) \boldsymbol{v} + \nabla p + \frac{\nabla B^2}{2\mu_0} - \frac{(\boldsymbol{B} \cdot \nabla)\boldsymbol{B}}{\mu_0} = -\rho \nabla \Phi + \boldsymbol{F}_{visc}, \tag{2.16}$$

$$\frac{\partial p}{\partial t} + \boldsymbol{v} \cdot \nabla p + \gamma p \nabla \cdot \boldsymbol{v} = \nabla \cdot (\boldsymbol{B} \times \eta \boldsymbol{J}) + Q, \qquad \gamma = \frac{5}{3}, \tag{2.17}$$

$$\frac{\partial \boldsymbol{B}}{\partial t} = \nabla \times (\upsilon \times \boldsymbol{B}) - \frac{\eta}{\mu_0} \nabla^2 B, \tag{2.18}$$

$$\nabla \cdot \boldsymbol{B} = 0, \tag{2.19}$$

$$p = \rho \frac{k_B}{m} T. \tag{2.20}$$

We need to stress here that the MHD equations are a system of (near) conservation laws. As such, they can also be rewritten and described as a system of conservative equations. This description will be of great interest when we will discuss the concept of numerically solving this system of equations, in order to deal with complicated physical systems.

One immediate physical property resulting from the previous set of equations, is the conservation of magnetic flux. In particular, from equations 2.18 and 2.19, in the limit of $\eta \to \infty$, we can show that the magnetic flux through a surface S that moves with the plasma, is conserved. This means that in ideal MHD the magnetic field lines are tied in to the plasma (frozen in condition), and they either follow the movement of the plasma ($\beta < 1$) or dictate it ($\beta > 1$). This way, the concept of a magnetic flux tube is derived (Fig. 2.1):

$$\Psi = \int_S \boldsymbol{B} \cdot d\boldsymbol{S} = \text{constant along the flux tube.} \tag{2.21}$$

2.3 MHD waves

From the theory of hydrodynamics, we know that pressure fluctuations in fluids can lead to the development of acoustic waves, propagating through the medium. The addition of gravity and the presence of an interface between regions of different densities can also introduce additional waves like surface and internal gravity waves. In the case of magnetised, quasi-neutral plasma an additional restoring force is introduced in the form of magnetic pressure fluctuations and the magnetic tension.

The study of waves is essential in the MHD description of the solar atmosphere, especially in the solar corona. In the transition region and the corona, the plasma β is lower than 1, meaning that the magnetic field dominates the dynamics and evolution of the solar plasma. Therefore, magnetic waves and transverse oscillations should be of great importance in the study of the plasma dynamics and energetics.

2.3.1 Linear MHD waves in a uniform medium

We will start our analysis, by focusing on a uniform infinite plasma. In order to analytically study MHD waves, we need to linearise the system of MHD equations. We linearise our system of equations by splitting the density (ρ), pressure (p), velocity vector ($\boldsymbol{v}$) and magnetic field vector ($\boldsymbol{B}$) into a constant ($\partial/\partial t = 0$) and homogeneous ($\nabla = 0$) background (f_0), and a small perturbation (f_1):

$$f(\boldsymbol{r}, t) = f_0 + f_1(\boldsymbol{r}, t), \qquad (|f_0| \gg |f_1|), \tag{2.22}$$

We also make the assumption that we have no background flows in the system ($\boldsymbol{v}_0 = 0$). By substituting the MHD equations and keeping only the first order terms in the linearised equations, we obtain the following system:

$$\frac{\partial \rho_1}{\partial t} + \rho_0 \nabla \cdot \boldsymbol{v_1} = 0, \tag{2.23}$$

$$\rho \frac{\partial \boldsymbol{v_1}}{\partial t} + \nabla p_1 - \frac{1}{\mu_0} (\nabla \times \boldsymbol{B_1}) \times \boldsymbol{B_0} - \frac{1}{\mu_0} (\nabla \times \boldsymbol{B_0}) \times \boldsymbol{B_1} = 0, \tag{2.24}$$

$$\frac{\partial p_1}{\partial t} + \gamma p_0 \nabla \cdot \boldsymbol{v_1} = 0, \tag{2.25}$$

$$\frac{\partial \boldsymbol{B_1}}{\partial t} - \boldsymbol{B_0} \cdot \nabla \boldsymbol{v_1} + \boldsymbol{B_0} \nabla \cdot \boldsymbol{v_1}, \qquad \nabla \cdot \boldsymbol{B_1} = 0, \qquad \nabla \cdot \boldsymbol{B_0} = 0, \tag{2.26}$$

where we have also neglected the resistive, viscous and other source terms (like gravity), and took advantage of the homogeneity of the background medium and the lack of background flows, in order to simplify our analysis.

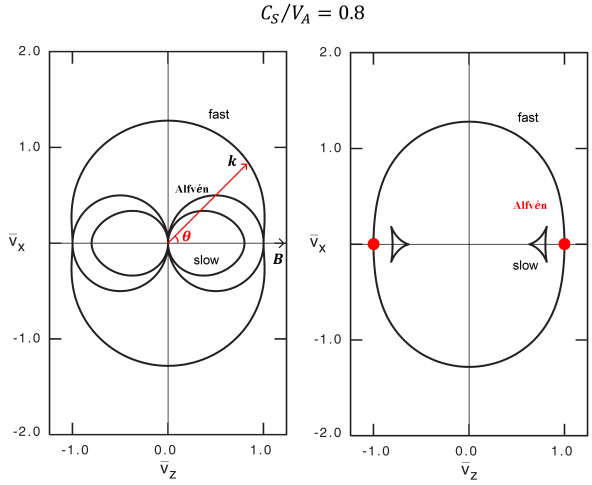

Figure 2.2: The phase (left) and group (right) diagrams for the MHD wave in a uniform and infinite plasma. The ratio of sound over Alfvén speed is 0.8. The magnetic field $\boldsymbol{B}$ is along the z axis and all the velocities are normalised to the Alfvén speed. Credit: Adapted from Goedbloed & Poedts (2004).

By assuming the equilibrium is homogeneous, the coefficients in the differential equations are all constant and the most general solution can be written as a superposition of plane waves:

$$\boldsymbol{v_1},\, \rho_1,\, p_1,\, \boldsymbol{B_1} \propto e^{i(\boldsymbol{k}\cdot\boldsymbol{r}-\omega t)},$$

where $\boldsymbol{k}$ is the wave vector and ω is the wave frequency. By substituting into the system of the linearised equations, we then solve the eigenvalue problem to get the dispersion relation for MHD in homogeneous plasma:

$$\omega^2(\omega^2 - k^2 V_A^2 \cos^2\theta)\left[\omega^4 - \omega^2 k^2 (V_A^2 + C_s^2) + k^4 V_A^2 C_s^2 \cos^2\theta\right] = 0, \qquad (2.27)$$

where θ is the angle between the wave vector $\boldsymbol{k}$ and the background magnetic field $\boldsymbol{B_0}$.

This dispersion relation contains the eight solutions of our system of equations, one of which is a spurious eigenvalue $\omega = 0$, while the other seven are true physical solutions, corresponding to different types of waves (Keppens & Demaerel 2016). For a more detailed analysis, the reader is referred to Goedbloed & Poedts (2004).

a) Entropy wave
The first of the seven physical solutions of Eq. 2.27 (also $\omega = 0$, not to be

confused with the spurious eigenvalue) represents a marginal entropy wave. This is a degenerate solution, since entropy waves do not propagate. In the approximation applied here, these waves also involve no velocity, pressure or magnetic field perturbations, but only an entropy perturbation. The entropy perturbation can only be transferred with a background flow, if we consider one, or thermal conduction.

c) Sound wave
Before continuing with the solutions of our Eq. 2.27, we will deal with the special case when the magnetic field is 0. If we neglect the entropy wave, then the above dispersion relation becomes

$$\omega^2 = k^2 C_s^2. \tag{2.28}$$

This is the relation for sound waves, with $C_s = \sqrt{p_0 \gamma \rho_0^{-1}}$ being the speed of sound in the background medium. Sound waves travel isotropically across the domain.

c) Alfvén wave
The second part of dispersion relation (Eq. 2.27):

$$\omega^2 = k^2 V_A^2 \cos^2\theta, \tag{2.29}$$

describes the Alfvén wave.

Alfvén waves are incompressible ($\boldsymbol{k} \cdot \boldsymbol{v} = 0$), they are transverse with respect to the velocity and magnetic field perturbations, and as a restoring force they 'see' the magnetic tension. Alfvén waves propagate along the magnetic field lines with the phase speed $v_{ph} = \omega k^{-1} = V_A \cos\theta$, where we include the Alfvén speed $V_A = B_0(\mu_0\rho_0)^{-1/2}$. These waves are also anisotropic, since they transfer energy along the magnetic field with the group speed ($v_{gp} = d\omega/dk$. The eigenfunctions of these waves just involve the perpendicular velocity and magnetic field, while the perturbations of the other quantities vanish.

d) Fast and slow magnetoacoustic waves
Taking the biquadratic term of Eq. 2.27:

$$\omega^4 - \omega^2 k^2 (V_A^2 + C_s^2) + k^4 V_A^2 C_s^2 \cos^2\theta = 0, \tag{2.30}$$

we get two solutions for the eigenfrequencies ($\omega_{f,s} = kV_{f,s}$), one for the fast and one for the slow magnetoacoustic wave. These waves are connected with perturbations in both the density and pressure, as well as the magnetic field. These are compressible waves ($\boldsymbol{k} \cdot \boldsymbol{v} \neq 0$) and are related with velocity perturbations both along and across the magnetic field. The phase speed of the

fast (V_f) and the slow (V_s) waves is given by:

$$V_{f,s} = \left\{ \frac{1}{2} \left[V_A^2 + C_s^2 \pm \sqrt{(V_A^2 + C_s^2)^2 - 4V_A^2 C_s^2 \cos^2\theta} \right] \right\}^{1/2}, \tag{2.31}$$

where the + and − correspond to V_f and V_s. The phase and group diagrams for the three pure MHD waves (Alfvén, slow and fast, respectively) can be seen in Fig. 2.2, for $C_s/V_A = 0.8$.

2.3.2 Linear MHD waves in a cylindrical flux tube

The previous analysis done for waves in uniform plasmas needs to be modified, since the solar corona is a highly inhomogeneous medium. In a non-uniform plasma, there are no pure waves, like those mentioned in the previous analysis. Waves can get different properties as they cross different media. We then call them *waves with mixed properties* or *linearly coupled waves* (Goossens et al. 2011). The spatial inhomogeneity introduces modifications in the dispersion relation of waves and oscillations, which depend on the spatial dependence of the plasma quantities like density, pressure and magnetic field.

A very interesting plasma structure in the solar atmosphere is that of a magnetic cylinder, or straight flux tube. Flux tubes have been used to model coronal structures such as loops, filaments, polar plumes, etc. A detailed derivation of the dispersion relation of fast and slow waves in such a cylindrical tube is given in studies by Zajtsev & Stepanov (1975), Ryutov & Ryutova (1976) and Edwin & Roberts (1983), while a review can be found in (Nakariakov & Verwichte 2005). Starting from a plasma structure with two media (which can be a cylinder, a slab, a simple interface etc.), and assuming longitudinal uniformity (i.e. along the contact surface between the two media), a pressure equilibrium has to exist between the 'internal' (i) and the 'external' medium (e):

$$p_i + \frac{B_i^2}{2\mu_0} = p_e + \frac{B_e^2}{2\mu_0}. \tag{2.32}$$

After linearising the MHD equations in cylindrical coordinates, for a cylindrical coordinate system with centre the axis of the cylinder, and applying perturbations of the form $f(r)\exp\left[i(k_z z + m\phi - \omega t)\right]$ we obtain the system of equations:

$$D\frac{d(r\xi_r)}{dr} = (C_A^2 + C_s^2)(\omega^2 - C_T^2 k_z^2)\left(\kappa^2 + \frac{m^2}{r^2}\right) rP', \tag{2.33}$$

$$\frac{dP'}{dr} = \rho_0(\omega^2 - C_A^2 k_z^2)\xi_r,$$

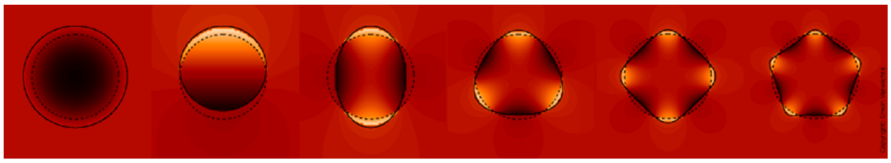

Figure 2.3: Snapshots of MHD wave modes in a cylindrical flux tube, where the ratio of the density pertubation over the background density is depicted. Lighter colours represent higher values of this ratio. From left to right, we see the sausage ($m = 0$), kink ($m = 1$), and fluting or ballooning modes ($m = 2, 3, 4,$ and 5). Credit: Dr. Erwin Verwichte, https://warwick.ac.uk/fac/sci/physics/research/cfsa/research/wpc/vis/

$$\rho_0(\omega^2 - C_A^2 k_z^2)\xi_\phi = -\frac{im}{r}P', \tag{2.34}$$

where P' is the perturbation of the total pressure ($P' = p' + BB'(\mu_0)^{-1}$), $\xi_{r,\phi}$ are the components of the Langrangian displacement, and

$$D = \rho_0(C_A^2 + C_s^2)(\omega^2 - C_A^2 k_z^2)(\omega^2 - C_T^2 k_z^2). \tag{2.35}$$

We can reduce the obtained system into one equation for each medium (Sakurai et al. 1991):

$$\left[\frac{d^2}{dr^2} + \frac{1}{r}\frac{d}{dr} - \left(\kappa_{i,\,e}^2 + \frac{m^2}{r^2}\right)\right] P' = 0. \tag{2.36}$$

The transverse wave number κ is defined as

$$\kappa^2(\omega) = -\frac{(\omega^2 - C_s^2 k_z^2)(\omega^2 - C_A^2 k_z^2)}{(C_A^2 + C_s^2)(\omega^2 - C_T^2 k_z^2)}, \tag{2.37}$$

where C_T is the cusp speed (a.k.a. tube speed), which is a combination of the sound and Alfvén speeds:

$$C_T = \frac{C_s C_A}{(C_A^2 + C_s^2)^{1/2}}. \tag{2.38}$$

For an equilibrium with a straight magnetic field, the perturbation of the total pressure P' couples the Alfvén waves to the magneto-sonic waves for $m \geq 1$ (Goossens et al. 2011). For $m = 0$, Eq. 2.34 decouples from Eqs. 2.33,

$$\rho_0(\omega^2 - C_A^2 k_z^2)\xi_\phi = 0, \tag{2.39}$$

leading to torsional Alfvén waves in a non-uniform cylindrical plasma for a longitudinal magnetic field.

Equation 2.36 is a modified Bessel equation. External (e) and internal (i) solutions of this equation have to be matched by the use of jump conditions for total pressure and the normal velocity, or the radial displacement (ξ_r):

$$[f] = \lim_{r \to r_A} \{f_i - f_e\}. \tag{2.40}$$

External and internal solutions have to agree with mode localisation. Modes outside of the flux tube need to decay as $r \to \infty$, thus we consider $\kappa_e > 0$. Modes inside the flux tube are bounded at $r = 0$. Modes with $\kappa_i > 0$ are called *surface modes*, and modes with $\kappa_i < 0$ are called *body modes*. The pressure perturbations inside (P_i') and outside (P_e') the tube are then:

$$P_i'(r) = \begin{cases} I_m(\kappa_i r), & \kappa_i^2 > 0 \\ i^m J_m(|\kappa_i| r), & \kappa_i^2 < 0 \end{cases}$$

and

$$P_e'(r) = A_e K_m(\kappa_e r),$$

where J_m is the Bessel function of the first kind, I_m is the modified Bessel function of the first kind, and K_m is the modified Bessel function of the second kind of order m. The derived dispersion relation for the surface waves in this system is:

$$\rho_e(\omega^2 - k_z^2 C_{Ae}^2)\kappa_i \frac{I_m'(\kappa_i R)}{I_m(\kappa_i R)} - \rho_0(\omega^2 - k_z^2 C_{A0}^2)\kappa_e \frac{K_m'(\kappa_e R)}{K_m(\kappa_e R)} = 0, \tag{2.41}$$

and for the body waves:

$$\rho_e(\omega^2 - k_z^2 C_{Ae}^2)|\kappa_i| \frac{J_m'(|\kappa_i| R)}{J_m(|\kappa_i| R)} - \rho_0(\omega^2 - k_z^2 C_{A0}^2)\kappa_e \frac{K_m'(\kappa_e R)}{K_m(\kappa_e R)} = 0. \tag{2.42}$$

I_m', J_m' and K_m' are the derivatives of the respective I_m, J_m and K_m functions. The integer m defines the azimuthal modal structure, with its sign describing the direction of . Waves with $m = 0$ (symmetric) are called *sausage* modes, waves with $m = 1$ are called *kink* modes, and waves with ≥ 2 are called *fluting* or *ballooning* modes (Fig. 2.3). When considering flux tubes of finite length with fixed boundaries, modelling coronal loops, then the longitudinal wave number k_z will be prescribed by these boundary conditions. For the standing modes that are then formed, those with the lowest wave numbers are called *global* or *fundamental*, while the rest are the *higher order harmonics*.

In the limit of a long wavelength - thin cylinder, known as *thin tube* approximation ($k_z R \ll 1$), the arguments of the Bessel functions are small, leading to:

$$|\kappa_i| \frac{J_m'(|\kappa_i| R)}{J_m(|\kappa_i| R)} \approx \frac{m}{R} \quad \text{and} \quad \kappa_e \frac{K_m'(\kappa_e R)}{K_m(\kappa_e R)} \approx -\frac{m}{R},$$

and the phase speed of all modes with $m > 0$ becomes equal to the *kink speed*

$$C_K = \left(\frac{\rho_0 C_{A0}^2 + \rho_e C_{Ae}^2}{\rho_0 + \rho_e} \right)^{1/2}, \tag{2.43}$$

which corresponds to the density weighted average Alfvén speed of the interior and exterior plasmas.

In the context of this thesis, we focus on the excitation and study of kink waves in straight flux tubes, as well as the non-linear dynamics that emerge in the interface between the loop and the exterior plasma. The motivation for this are the observations of the past twenty years, that have revealed the ubiquitous existence of transverse waves in the solar atmosphere. The first identification of transverse oscillation in coronal loops were performed by Aschwanden et al. (1999) and Nakariakov et al. (1999). Ever since then, observations by the Coronal Multi-channel Polarimeter (CoMP), the Solar Dynamics Observatory (SDO), and Hinode spacecraft have further sustained the interest in areas of the solar atmosphere where waves are found in abundance. A large number of studies has already proven the ubiquity of transverse perturbations along coronal loops (Verwichte et al. 2005; McIntosh et al. 2011; Nisticò et al. 2013), prominence threads (Okamoto et al. 2007) and greater areas of the corona (Tomczyk et al. 2007; Tomczyk & McIntosh 2009; Thurgood et al. 2014; Morton et al. 2016, 2019).

The initial hypothesis that described these as Alfvén waves was questioned by Van Doorsselaere et al. (2008), who proposed that they are in fact kink waves. This proposal was inspired by the fact that there have been observed travelling along flux tubes in the solar atmosphere, rather than in a homogeneous plasma as it would be expected of pure Alfvén waves, and showed large transverse displacements from the equilibrium position. The Alfvénic nature of those kink waves in magnetic flux tubes has also been proven in Goossens et al. (2009).

2.4 Wave damping mechanisms

The wave solutions considered so far are characterised by a constant amplitude. However, the observed waves in the solar corona, with the exception of the already mentioned decayless waves, exhibit damping (Aschwanden et al. 1999).

If the equilibrium parameters of the plasma vary continuously across the magnetic field, then the eigenfrequencies of the previously derived modes can also vary continuously, giving rise to two distinct ranges of continuously varying frequencies, the slow and Alfvén continua. In the solar corona, we focus on

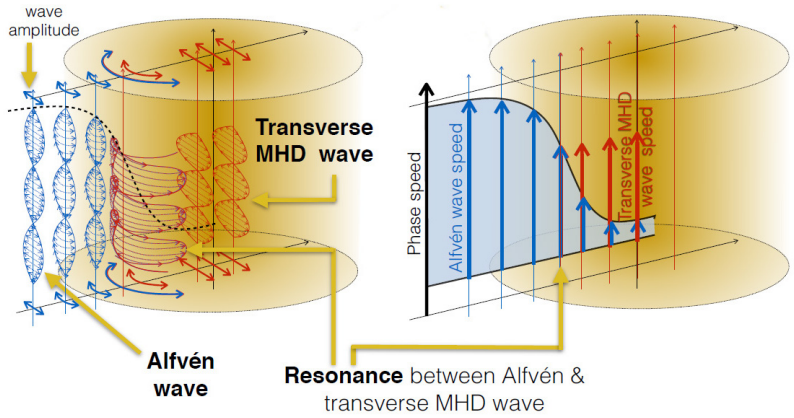

Figure 2.4: Schematic representation of the spatial evolution of resonant absorption of transverse kink waves in a flux tube. Credit: Dr. Patrick Antolin, Dr. Joten Okamoto (JAXA), http://www.isas.jaxa.jp/e/topics/2015/0828a.shtml

the Alfvén continuum, due to the dominant nature of the magnetic field. Two effects associated with wave modes from these continua are resonant absorption and phase-mixing. These two mechanisms are associated with the observed damping of the waves in the solar atmosphere and have been extensively used in the context of coronal seismology.

Resonant absorption (or dissipation) (Sakurai et al. 1991; Goossens & Poedts 1992; Goossens et al. 1992; Ruderman & Roberts 2002; Aschwanden et al. 2003; Goossens et al. 2011) takes place when an excited mode has a frequency that falls within the range of one of the two continua (here we consider the Alfvén continuum), for a smooth transverse profile of Alfvén speed, leading to $D = 0$ from Eq. 2.35. The physical location of the resonance is called the resonant layer, and it is traditionally expected to be located near the radial shell in the case of cylindrical flux tubes, where the Alfvén frequencies continuously vary. The excited mode has a peak amplitude at the point of resonance (Nakariakov & Verwichte 2005; Goossens et al. 2011, for a review). A schematic representation of this process is shown in Fig. 2.4.

Resonant absorption can only take place for modes with $m \geq 1$, because for $m = 0$ Eq. 2.34 decouples from Eqs. 2.33, making resonance impossible. When we have resonance, Eqs. 2.33 and 2.34 produce a singularity, which can be removed by switching to resistive MHD near the resonant layer. This leads to a fourth-order differential equation, which we can avoid through the use of

jump conditions across the resonant layer, and by assuming that we have a thin non-uniform layer, known as the *thin boundary* approximation ($l_{\rm layer} \ll R_{\rm tube}$). By using Taylor series expansion on Eqs. 2.33 and 2.34, and applying the jump conditions across the singularity for P' and ξ_r, we obtain the following:

$$[P'] = 0, \tag{2.44}$$

$$[\xi_r] = -i\pi \frac{m^2}{r_0^2 \rho_0 |\Delta|} P', \tag{2.45}$$

where ρ_0 is the density at the resonant point (or layer) r_0 and $\Delta = d(\omega^2 - \omega_A^2)/dr|_{r=r_0}$.

We see that the jump condition for the displacement perturbations (ξ_r) is complex, which leads to complex frequencies from the dispersion relation, providing us with damped wave solutions. These are natural modes in resistive MHD, and they are called *quasi-modes* in ideal MHD (Poedts & Kerner 1991). By considering the *thin tube* ($k_z R \ll 1$) and *thin boundary* ($l_{layer} \ll R_{tube}$) approximations for a sinusoidal resonant layer, the damping time τ_D is equal to Ruderman & Roberts (2002); Goossens et al. (2002):

$$\tau_D = \frac{2}{\pi} \frac{R}{l} \frac{\rho_0 + \rho_e}{\rho_0 - \rho_e} P_{\rm kink}, \tag{2.46}$$

where $R\,l^{-1}$ is the ratio of the loop width over the inhomogeneous layer width, and $P_{\rm kink}$ is the period of the kink mode at the fundamental harmonic:

$$P_{\rm kink} = \frac{2L}{C_K}, \tag{2.47}$$

with L being the length of the cylindrical flux tube.

We need to stress that resonant absorption is not a true energy dissipation mechanism, but a damping mechanism. Resonant absorption is an ideal MHD method to transfer energy from the global mode to the localised Alfvén wave, leading to damping of the global mode. In the solar atmosphere, the Reynold's numbers are $\gg 1$, except in regions where smaller scales are present. One method of producing smaller scales from Alfvén waves, leading to dissipation is the mechanism of phase mixing.

Phase mixing takes place in a medium where a continuous inhomogeneity profile exists across the magnetic field, leading to large gradients in the Alfvén velocity (Heyvaerts & Priest 1983; Soler & Terradas 2015). If we excite shear Alfvén waves with frequencies that lie in the range of the Alfvén continuum, then the different magnetic field lines will end up oscillating out of phase with each other. This will eventually lead to the creation of gradually smaller scales across the

inhomogeneity. Once the scales become small enough, then the Reynold's and magnetic Reynold's number will reach the range where dissipation becomes important ($R_{e,m} \approx 1$). By considering an interface along the x-axis, the Alfvén waves, if they are polarised in the y-direction, are described by the wave equation:

$$\left(\frac{\partial^2}{\partial t^2} - v_A^2(x) \frac{\partial^2}{\partial z^2} \right) v_y = 0, \tag{2.48}$$

which has solution

$$v_y = \Psi(x) f(z \mp v_A(x) t), \tag{2.49}$$

with $\Psi(x)$ and $f(z)$ giving the initial wave. This wave solution quantifies the aforementioned procedure of small scales generation.

In the presence of finite dissipation, we need to introduce an additional term $\nu\, \partial/\partial t\, \nabla^2 v_y$ in the right hand side of the wave equation 2.48. The coefficient ν can describe either viscosity of resistivity. In the developed stage of phase mixing, described by ($\partial/\partial x \gg \partial/\partial z$) perturbations of different magnetic surfaces become uncorrelated with each other, and the velocity perturbations decay according to Heyvaerts & Priest (1983) as:

$$v_y \propto v_y(0) \exp \left\{ -\frac{v k_z^2}{6 C_A^3(x)} \left[\frac{dC_A(x)}{dx} \right]^2 z^3 \right\}, \tag{2.50}$$

for propagating and

$$v_y \propto v_y(0) \exp \left\{ -\frac{v k_z^2}{6} \left[\frac{dC_A(x)}{dx} \right]^2 t^3 \right\}, \tag{2.51}$$

for standing Alfvén waves.

As mentioned before, the resonant layer in magnetic cylinders is considered to be at the flux tube radial shell. This also confines the effects of phase mixing in the same layer, leaving the inner parts of the flux tubes without a heating source (Cargill et al. 2016). This would lead to the inevitable radiative cooling of the flux tube. A way to bypass this problem, which will be considered in Chapter 4, is the Kelvin-Helmholtz instability (KHI).

The *Kelvin-Helmholtz instability* is developed when there is a velocity jump gradient an interface (Fig. 2.5). Let us consider two homogeneous plane plasma layers at $z \in [-\alpha, \alpha]$, separated by an interface at $z = 0$. These layers have embedded constant magnetic fields $\boldsymbol{B_1} = (B_{1x}, B_{1y}, 0) = const$ and $\boldsymbol{B_2} = (B_{2x}, B_{2y}, 0) = const$, constant velocity fields $\boldsymbol{V_1} = (V_{1x}, V_{1y}, 0) = const$ and $\boldsymbol{V_2} = (V_{2x}, V_{2y}, 0) = const$, background densities ρ_1 and ρ_2 and pressures p_1 and p_2.

We can then study this instability through a similar way that we study wave modes at an interface. Starting from the ideal MHD equations (we consider gravity $\boldsymbol{g} = -g\hat{z}$), we perform a normal mode analysis of this configuration, with Fourier harmonics in the ignorable directions $\boldsymbol{\xi} \sim \exp\left[i(k_x x + k_y y - \omega t)\right]$ and apply jump conditions across the interface, namely the condition for the total pressure balance and continuity of the normal velocity:

$$[P_{tot}] = 0 \quad \text{and} \quad [\boldsymbol{n} \cdot \boldsymbol{\xi}] = 0 \quad ,$$

where n is the unit vector normal to the interface, in order to enforce continuity across the interface. An additional boundary condition is derived by keeping the velocity finite away from the interface:

$$[\boldsymbol{v}] = \text{ finite} \quad \text{at} \quad z \to \pm\alpha.$$

In the limit of small wavelength perturbations for incompressible plasmas, the resulting dispersion relation (Goedbloed et al. 2010) has solutions of the form

$$\omega = \frac{\rho_1\Omega_1 + \rho_2\Omega_2}{\rho_1 + \rho_2} \pm \sqrt{\frac{\rho_1\omega_{A1}^2 + \rho_2\omega_{A2}^2}{\rho_1 + \rho_2} - \frac{\rho_1\rho_2(\Omega_1 - \Omega_2)^2}{(\rho_1 + \rho_2)^2} - k_0 g\frac{(\rho_1 - \rho_2)}{\rho_1 + \rho_2}}, \tag{2.52}$$

where we $\omega_{Ai} = \boldsymbol{k_0} \cdot \boldsymbol{V_{Ai}}$ is the Alfvén frequency in each medium, and $\Omega_i = \boldsymbol{k_0} \cdot \boldsymbol{V_i}$. If the expression under the square root is negative, this solution represents an instability and a damped wave. The instability is driven by a destabilizing Kelvin–Helmholtz contribution when $V_1 \neq V_2$, a stabilizing magnetic field contribution when $\omega_{A1} \neq 0$ and (or) $\omega_{A2} \neq 0$, and finally, a destabilizing Rayleigh–Taylor contribution when $\rho_1 > \rho_2$ (or stabilizing when $\rho_1 < \rho_2$).

While studying the damping mechanisms for Alfvén waves in the boundary layers of flux tubes, Heyvaerts & Priest (1983) predicted the existence of Kelvin-Helmholtz Instabilities (KHI) in the resonant layer, through a non-linear connection with phase mixing. The strong shear velocities generated by the azimuthal Alfvén waves (like the local Alfvén modes in resonant absorption) can give rise to Kelvin-Helmholtz turbulence. Propagating waves are expected to be Kelvin-Helmholtz stable, while the instability is more likely in standing oscillations (Zaqarashvili et al. 2015).

If we consider a cylindrical discontinuous interface, like in the case of a flux tube, for two homogeneous stationary rotating fluids, the growth rate of the Kelvin-Helmholtz instability is connected to the azimuthal wave number m for each value of the velocity shear (Terradas et al. 2008). For typical values of oscillating flux tubes, the growth rate of the KHI is found to be only a fraction of an oscillation period (Antolin et al. 2014). Hillier et al. (2019) have demonstrated that oscillating MHD shear flows, like those expected in oscillating

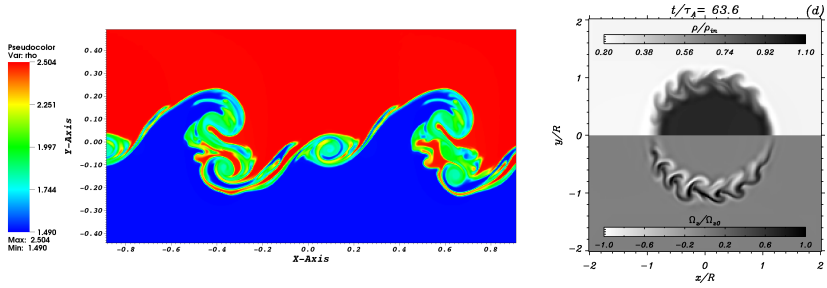

Figure 2.5: On the left panel: Kelvin-Helmholtz instability in a 2D simulation of a magnetised plasma. Snapshot is taken for density. On the right panel, snapshot of a 3D simulation of a coronal loop at the apex from Terradas et al. (2008). The density (upper half) and vorticity (lower half) are depicted at time $t = 63.6\tau_A$, where τ_A is the Alfvén crossing time across the flux tube, for an Alfvén velocity of the order of 10^6 m s^{-1}.

coronal loops, are also unstable to the KH instability, as well to parametric instabilities involving surface Alfvén waves. In Barbulescu et al. (2019) it was shown that the magnetic twist at an interface does not prevent the onset of the KH instability at the boundary of an oscillating magnetic tube.

Three dimensional simulations in straight flux tubes confirmed the non-linear connection between resonant absorption, phase mixing and KHI for azimuthal Alfvén waves (Uchimoto et al. 1991; Ofman et al. 1994c; Poedts & Goedbloed 1997; Poedts et al. 1997) and for standing kink waves (Terradas et al. 2008; Antolin et al. 2014; Magyar & Van Doorsselaere 2016; Howson et al. 2017a; Karampelas et al. 2017). Additional work has been performed in order to develop methods of identifying the effects of KHI in oscillating loops (Goddard et al. 2018; Van Doorsselaere et al. 2018). The presence of KHI and its connection to turbulence has also been studied in chromospheric jets (Kuridze et al. 2015, 2016) as an explanation of the observed, non-thermal, line broadening.

2.5 Computational MHD

Unlike most fields of hard sciences (like mathematics, chemistry, solid state physics etc.), astrophysics have a very important shortcoming. We are unable to test the validity of our hypotheses and the strengths of our theories through proper experiments. This is the result of the enormous scales of the systems of interest, the distance of those systems from us, as well as the extreme conditions that are present as a background to the processes that we need to test. To

circumvent this, astrophysics and solar physics rely heavily on observations and computational physics. While observations can provide us with valuable data on the systems that we are interested in, numerical analysis provides us with insight when explaining the aforementioned observations and the underlying physics.

Computational methods have become very popular, following the increasing demand for quantitative results on realistic models and the availability of computational resources. In general, they are used whenever a mathematical model is too complex to properly solve analytically. This principle is also applied in magnetohydrodynamics, where numerical codes and parallel computations are extensively used in the study of astrophysical systems. A large number of highly advanced, modular codes exist that solve the system of the (M)HD equations, in a Newtonian and (special) relativistic frame. Some of the most popular codes that utilise the fluid description are FLASH[1], MPI-AMRVAC[2], PLUTO[3], PENCIL[4] and LARE3D[5].

2.5.1 Conservative MHD equations

In our studies we used the MPI-AMRVAC (Keppens et al. 2012; Porth et al. 2014) and PLUTO (Mignone et al. 2012, 2018) codes. These are modular frameworks, aimed at solving the (M)HD system of partial differential equations by a number of different numerical schemes. These codes emphasize on (near) conservation laws and on shock-capturing schemes, while numerical tests that we performed with them have shown that both codes conserve the total energy of the system effectively.

Focusing on the MHD framework, both of these codes solve the following form of the MHD equations for density ρ, momentum density $\rho\boldsymbol{v}$, total energy density e and the magnetic field $\boldsymbol{B}$:

$$\frac{\partial \rho}{\partial t} + \nabla \cdot (\rho \boldsymbol{v}) = 0, \tag{2.53}$$

$$\frac{\partial \rho \boldsymbol{v}}{\partial t} + \nabla \cdot (\rho \boldsymbol{v}\boldsymbol{v} - \boldsymbol{B}\boldsymbol{B} + \boldsymbol{I} p_{tot}) = 0, \tag{2.54}$$

$$\frac{\partial e}{\partial t} + \nabla \cdot (\boldsymbol{v} e - \boldsymbol{B}\boldsymbol{B} \cdot \boldsymbol{v} + \boldsymbol{v} p_{tot}) = 0, \tag{2.55}$$

[1] http://flash.uchicago.edu/site/flashcode/
[2] http://amrvac.org/
[3] http://plutocode.ph.unito.it/
[4] http://pencil-code.nordita.org/
[5] https://warwick.ac.uk/fac/sci/physics/research/cfsa/people/tda/larexd/

$$\frac{\partial \boldsymbol{B}}{\partial t} + \nabla \cdot (\boldsymbol{v}\boldsymbol{B} - \boldsymbol{B}\boldsymbol{v}) = 0, \tag{2.56}$$

$$e = \rho\frac{\upsilon^2}{2} + \frac{p}{\gamma - 1} + \frac{B^2}{2},$$

which are derived from Eqs. 2.15-2.18, but written in their *conservative form*:

$$\frac{\partial U}{\partial t} + \nabla \cdot \boldsymbol{F}(U) = 0, \tag{2.57}$$

with U being the *conservative variables* and $\boldsymbol{F}(U)$ the *fluxes*. In the previous system of the MHD equation, $\boldsymbol{B}$ is the magnetic field with the absorbed $1/\sqrt{\mu_0}$ terms, $\boldsymbol{I}$ is the unit tensor of rank 3, and the product of two vectors (i.e. $\boldsymbol{v}\boldsymbol{B}$) is the dyadic product. We have neglected gravity and dissipation terms in order to simplify the current analysis.

2.5.2 Finite volume method

Both MPI-AMRVAC and PLUTO codes utilise shock capturing *finite volume* methods in order to solve the above conservative equations. In finite volume schemes, the computational domain is discretized into small cells, with the values of the conservative values defined inside the cells and the fluxes defined on the side surfaces (Fig. 2.6). Finite volume methods solve Eq. 2.57, or in particular its integral form over small volumes V_i:

$$\frac{\partial}{\partial t}\int_{V_i} U dV = -\int_{V_i} \nabla \cdot \boldsymbol{F}(U) dV = -\oint_{S_i} \boldsymbol{F}(U) \cdot d\boldsymbol{S} = 0. \tag{2.58}$$

In the following example we will consider the 1D case, and we will treat the 'volume' V_i as a line with length $\Delta x_i = x_{i+1/2} - x_{i-1/2}$. Discretizing Eq. 2.58 and keeping only the first order terms gives us:

$$\frac{dU_i}{dt} + \frac{1}{\Delta x_i}\left(F_{i+1/2} - F_{i-1/2}\right), \tag{2.59}$$

where we have used the volume averaged variable:

$$U_i = \frac{1}{\Delta x_i}\int_{x_{i-1/2}}^{x_{i+1/2}} U(x,t)dx.$$

In order to properly solve the above discretized equation (Eq. 2.59), codes like MPI-AMRVAC and PLUTO utilize various methods to accurately perform the spatial and temporal integration of U and F. The different methods are the

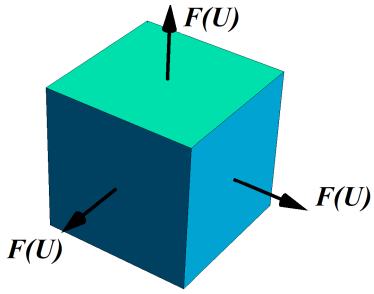

Figure 2.6: Schematic representation of a cell inside a $3D$ numerical domain, in Cartesian coordinates. The primitive cell averaged quantities are $U_{i,j,k} = U$. For sipmlicity, the cell is considered cubic, and the fluxes $F_{i,j,k\pm1/2}$ along the x, y and z axes through the cell interfaces are all taken equal to $F(U)$.

time integrators, the *solvers* and the *flux limiters* (for a more detailed analysis, the reader is referred to Toro 2009).

Time integrators are responsible for the temporal integration of Eq. 2.59. Depending on their accuracy and steps required for the time integration, they can be a simple 'onestep' or Eulerian method, a 'twostep' corrector-predictor method, a higher order Runge-Kutta method etc, or other types of methods that contain additional approximations and corrections for stability and efficiency reasons. During time integration for the 1D case, the time step[6] $\Delta t = t^{n+1} - t^n$ is controlled through the Courant-Friedrichs-Lewy (CFL) condition:

$$C = \frac{u\Delta t}{\Delta x_i} \leq C_{max}, \tag{2.60}$$

where u is the magnitude of the velocity. The CFL condition ensures convergence in numerical integration schemes, and is used for stability reasons. For the 1D case and for an explicit time integration scheme $C_{max} = 1$. This ensures that the information will not travel across more than one cell during an integration cycle. For higher dimension problems and different time-integrators, the maximum value of the Courant number C_{max} can be smaller than 1. In the case where implicit integration methods are used, then stability is inherently ensured, at the cost of computations, and C_{max} can be larger than 1.

Solvers are the methods used to perform the spatial integration of Eq. 2.59, and more specifically the value of the fluxes F across a cell surface. The solvers have to deal with the spatial *reconstruction* of the solution as well as the calculation of the fluxes themselves. Reconstruction methods set the spatial

[6]Here t^n only denotes the specific moment in time, not a power to the nth

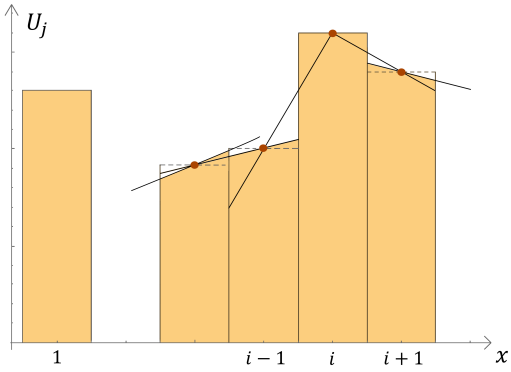

Figure 2.7: 1D piecewise discretization of the conservative variable U_j. The slopes σ_i of the lines connecting the different values of U_j are determined by the slope limiters, to ensure stability. In the case of different signs of the slopes (as in $x = i$), the constant extrapolation switches on. The reader is referred to Toro (2009) and Goedbloed et al. (2010) for a detailed analysis.

order of integration, and they usually are flat, linear, or higher second and third order methods, depending on the number of points on the stencil considered.

For the calculation of the fluxes, the most common methods are the Godunov schemes. These methods are based on the work originally made by Godunov (Godunov 1959). That method considered the cell averaged values U_i^n at time t^n as piecewise constant data throughout the cells, and then solved the discontinuous Riemann problems that would arise at each cell interface, deriving the fluxes. However, in MHD this can not be done analytically, forcing us to use approximate solvers like the Roe solver (which solves the linearised problem), the HLL, HLLC and HLLD (for MHD) approximate solvers, the more diffusive Lax-Friedrich solver etc.

Flux or *slope limiters* are used in order to avoid spurious oscillations that would otherwise occur with high order schemes due to shocks, discontinuities or sharp changes in the solution domain. Flux limiters are used when we try to estimate the values of the variables U_i to be used by the solver for the calculation of the corresponding fluxes. In finite volume methods, this evaluation of fluxes at the cell edges requires some form of extrapolation to take place from the volume averaged values of U_i. For a given cell interface at $x_{i+1/2}$, we can use the following extrapolation left and right of the interface (Goedbloed et al. 2010):

$$U^L_{i+1/2} = U_i + \frac{\sigma_i}{2}, \tag{2.61}$$

$$U^R_{i+1/2} = U_i - \frac{\sigma_{i+1}}{2}, \tag{2.62}$$

where $\sigma_i = U_{i+1/2} - U_{i-1/2}$ is the slope used for the linear extrapolation inside the cells left and right of the interface (Fig. 2.7). The corresponding fluxes are then taken as the average:

$$F_{i+1/2} = \frac{F(U^L) + F(U^R)}{2}. \tag{2.63}$$

This raises the order of integration to second order, but can also lead to spurious numerical oscillations in our solutions. To counter this, *slope limiters* are used to modify σ_i, suppressing these errors. Different slope limiters in use by MPI-AMRVAC and PLUTO are the 'minmod' (most diffusive) to the monotonized central difference limiter and 'superbee' (least diffusive limiters).

2.5.3 Enforcing the $\nabla \cdot B = 0$ condition

Due to the approximations used in the above analysis, errors can manifest in the solutions. Such errors in the magnetic field will eventually violate the $\nabla \cdot B = 0$ condition, leading to non-physical solutions. Since this condition is not included in the above analysis for the finite volume schemes (or any other numerical scheme on that matter), we need to treat it independently. For more information on the different $\nabla \cdot B = 0$ control strategies proposed in literature, see also the review by Tóth (2000).

One method that has been used in our studies was Powell's scheme or Eight-Wave Formulation (Powell et al. 1999). In this cell-centred approach, we consider again Eqs. 2.53-2.56, only we now introduce the following source terms on the right-hand side of those equations (one for each corresponding equation):

$$S_{\mathrm{MHD}} = -\nabla \cdot \boldsymbol{B} \left\{0,\, \boldsymbol{B},\, \boldsymbol{v} \cdot \boldsymbol{B},\, \boldsymbol{v}\right\}^T.$$

Powell's method is a very stable, cost-effective method, that gives sufficiently good results on most occasions. However, it does NOT keep the divergence close to zero down to machine accuracy. This may cause accumulation of errors in the presence of strong discontinuities, shocks or prolonged computations.

The second and more accurate method that was used in our studies was Dedner's scheme (Dedner et al. 2002) or mixed GLM hyperbolic/parabolic correction. In this method the induction equation and the divergence of the magnetic field are modified, in order to include the generalized Lagrangian multiplier ψ (GLM):

$$\frac{\partial \boldsymbol{B}}{\partial t} + \nabla \times \boldsymbol{E} + \nabla \psi = 0, \tag{2.64}$$

$$\frac{\partial \psi}{\partial t} + u^2 \nabla \cdot \boldsymbol{B} = -\frac{u^2}{c_p^2}\psi, \tag{2.65}$$

where u is the maximum speed allowed from the CFL condition, $c_p = \sqrt{\Delta l_{\min} u/\alpha}$ and α is a parameter that sets the effectiveness of the damping (and affects numerical stability). With this method, the errors are advected away towards the boundaries of the problem, while they are damped at the same time. The advantage of this scheme is that it uses the conservative form of the MHD equations (no additional source terms are introduced), all variables are cell-centred and standard solvers can be utilized.

In the following chapters, we make use of the numerical methods presented in here in order to study the development of the KH instability in simulations of footpoint driven oscillations of straight flux tubes. The effects of the KHI, resonant absorption and phase mixing on the efficiency energy dissipation and wave heating are examined in simulations in Chapters 3 and 5. Different temperature configurations were considered, with and without the use of gravity and physical dissipation parameters. In Chapter 4, we address the problem of spatial confinement of wave heating at the loop edges, for dynamically evolving flux tubes through the development of KH eddies. Finally, chapter 6 studies the effects of the KHI on synthetic emission data from simulations of oscillating coronal loops.

Chapter 3

Heating by transverse waves in coronal loops

"Nothing happens until something moves."
Albert Einstein

Abstract
In the current chapter we study the effects of wave heating from driven and standing transverse waves in a coronal loop. Past studies of oscillating flux tubes have already established the significance of resonant absorption in damping transverse oscillations in coronal loops. The non-linear nature of the mechanism has been examined alongside the Kelvin-Helmholtz instability, which is expected to manifest in the resonant layers of flux tubes. While both processes have been hypothesized to contribute to wave heating through the dissipation of wave energy into smaller scales, the occurring mixing with the hotter surroundings can potentially hide this effect. Using the MPI-AMRVAC code, we perform ideal, three dimensional MHD simulations of both (a) footpoint driven and (b) free standing oscillations in a straight coronal flux tube, in the presence of numerical resistivity. We observe the development of Kelvin-Helmholtz eddies at the loop boundary layer of the models considered here, as well as an increase of the volume averaged temperature inside the loop. The main heating mechanism in our setups is Ohmic dissipation, as indicated by the higher values for the temperatures and current densities located near the footpoints. The introduction of a temperature gradient between the inner tube and the surrounding plasma, suggests that the mixing of the two regions, in the case of hotter environment, greatly increases the temperature of the tube at the site of the strongest turbulence, beyond the contribution of the aforementioned wave heating mechanism.

This chapter is based on the work by Karampelas et al. (2017).

3.1 Introduction

Since the discovery of transverse magnetohydrodynamic (MHD) oscillations (Aschwanden et al. 1999; Nakariakov et al. 1999), they have been the topic of many studies, both observational and numerical. Stretching from the lower chromosphere up to the solar corona, the physical characteristics of loops allow them to act as waveguides, effectively transferring energy between those different layers. Analytical studies on the nature of the transverse oscillations in cylindrical flux tubes (Zajtsev & Stepanov 1975; Ryutov & Ryutova 1976; Edwin & Roberts 1983) have described the different modes expected in a non-uniform plasma with cylindrical symmetry.

Observations from the Coronal Multi-channel Polarimeter (CoMP), the Solar Dynamics Observatory (SDO) spacecraft and Hinode Solar Observatory have revealed the existence of ubiquitous transverse perturbations travelling along coronal loops, prominence threads and greater areas of the corona (Tomczyk et al. 2007; Okamoto et al. 2007; Tomczyk & McIntosh 2009; McIntosh et al. 2011; Nisticò et al. 2013; Anfinogentov et al. 2015). Due to their high speeds and apparent incompressible nature, Tomczyk et al. (2007) have considered these perturbations to be Alfvén waves, travelling in the solar corona. Considering the energy budget of these propagating waves, Tomczyk et al. (2007) estimated an energy flux four orders of magnitude smaller than needed to balance the radiative losses of the quiet solar corona. However, there has been a lot of uncertainty regarding the estimated energy carried by the waves in the solar atmosphere (De Pontieu et al. 2007b; McIntosh et al. 2011; Goossens et al. 2013; Van Doorsselaere et al. 2014b; Thurgood et al. 2014; Morton et al. 2016), with the line of sight (LOS) being a particularly important factor (McIntosh & De Pontieu 2012; De Moortel & Pascoe 2012). Meanwhile, the nature of these oscillations has been under debate, with Van Doorsselaere et al. (2008) proposing that they are in fact Alfvénic, transverse surface (kink) waves, since they have been observed travelling along flux tubes in the solar atmosphere, rather than in a homogeneous plasma as it would be expected of Alfvén waves. The Alfvénic nature of those kink waves in magnetic flux tubes has also been proven in Goossens et al. (2009).

For the proposed heating of the solar atmosphere a dissipation mechanism is necessary for the observed oscillations to transfer their kinetic energy into internal energy of the plasma. Tomczyk & McIntosh (2009) reported significant

spatial attenuation in the power of the aforementioned observed propagating waves. Additional observational evidence was presented in Verth et al. (2010), while in Terradas et al. (2010), the mechanism of resonant absorption was used to analytically explain this spatial attenuation. The analogous mechanisms of resonant absorption (Sakurai et al. 1991; Goossens & Poedts 1992; Goossens et al. 1992; Goossens et al. 2002; Ruderman & Roberts 2002; Arregui et al. 2005; Goossens et al. 2006; Goossens et al. 2011) and mode coupling (Pascoe et al. 2010, 2012; De Moortel et al. 2016) have been thus considered responsible for the damping of transverse waves in flux tubes. Through resonance, the energy of the global kink mode is transferred to local azimuthal Alfvén modes in the boundary layer at the loop edges, reducing the amplitude of the oscillations. In the case in which multiple frequencies are excited (for example, should a broad-band driver be considered or in the case of non-linear effects due to resistivity and viscosity), smaller scales are created through the mechanism of phase mixing (Heyvaerts & Priest 1983; Poedts & Boynton 1996; Soler & Terradas 2015). The connection between resonant absorption and the heating of loops has been studied in the past (Ofman et al. 1994a,b; Poedts & Boynton 1996; Ofman et al. 1998), where resistivity and/or viscosity were considered, in order to dissipate the energy contained into the created smaller scales.

While studying the damping mechanisms for Alfvén waves in the boundary layers of flux tubes, Heyvaerts & Priest (1983) predicted the existence of Kelvin-Helmholtz Instabilities (KHI) in the resonant layer, through a non-linear connection with phase mixing. They argued that the strong shear velocities generated by the azimuthal Alfvén waves can give rise to Kelvin-Helmholtz turbulence, which in turn reinforces the effects of phase mixing through the creation of smaller scales. Propagating waves were predicted to be Kelvin-Helmholtz stable, while standing oscillations should be unstable near the positions of the velocity antinodes. Zaqarashvili et al. (2015) have also predicted that the higher values of azimuthal velocities at loop edges near these velocity antinodes would make standing kink modes and torsional Alfvén waves Kelvin-Helmholtz unstable. The presence of KHI and its connection to turbulence has also been studied in chromospheric jets (Kuridze et al. 2015, 2016) as an explanation of the observed, non-thermal, line broadening.

Three dimensional simulations in straight flux tubes confirmed the non-linear connection between resonant absorption, phase mixing and KHI for driver generated azimuthal Alfvén waves (Uchimoto et al. 1991; Ofman et al. 1994c; Poedts & Goedbloed 1997; Poedts et al. 1997). More recent numerical studies (Terradas et al. 2008; Antolin et al. 2014, 2015; Antolin et al. 2016; Magyar et al. 2015; Magyar & Van Doorsselaere 2016) have confirmed the development of Kelvin-Helmholtz induced turbulence in straight flux tubes even for small amplitude standing kink waves. In particular, Antolin et al. (2014), through

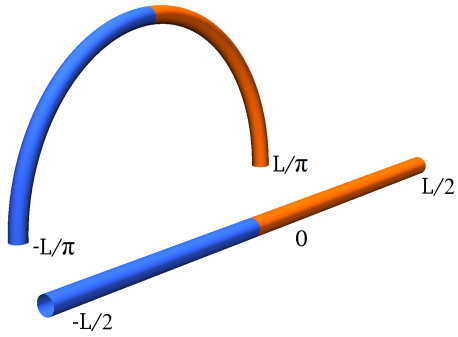

Figure 3.1: Graphical representation of a semicircular loop and its equivalent model of a straight flux tube. The part of the flux tube used in our simulations (from one footpoint to the apex) is shown in orange. The same area is highlighted with orange on the semicircular loop. Credit to Mingzhe Guo, for the data on the semicircular loop.

the use of forward modelling, proved that KHI can create apparent strands along flux tubes, as a LOS effect, providing us with a potential method to indirectly observe this instability in coronal loops. Additionally, Magyar & Van Doorsselaere (2016) showed that the developed KHI can lead to faster damping of standing transverse waves than analytically predicted from resonant absorption, further proving its effectiveness.

Following the idea that resistive and viscous dissipation contributed to heating, Antolin et al. (2014) suggested that the developed Kelvin-Helmholtz instabilities at the resonant layer could lead to an increase in the flux tube temperature. The profiles of his tube cross-section at the antinode position revealed the existence of small length scales in z-current density, similar to those created by the Kelvin-Helmholtz eddies. However, Magyar & Van Doorsselaere (2016) pointed out that the mixing between the colder flux tube and the hotter surrounding plasma led to higher average temperatures than those expected from the increase of the internal energy for the given simulation time.

In the current work, we focus on the temperature evolution in both driven and freely transversely oscillating flux tubes, due to non-linear dissipation of wave energy. Physical resistivity is not included in our three dimensional MHD models, but the effects of numerical resistivity are present and are used in the study of wave energy dissipation. We consider models of equal temperature inside and outside of the flux tube, so that we can isolate the mechanisms of wave heating from the effects of mixing between regions of different temperature.

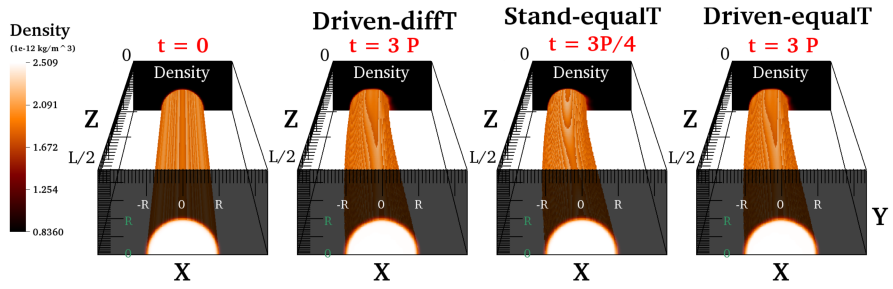

Figure 3.2: 3D density plot, measured in 10^{-12} kg m^{-3}, of our basic setup (t = 0), and of the three different models at later times. The cross sections on the $x-y$ planes at the footpoint ($z = L/2 = 100$) and the apex ($z = 0$ Mm) are shown. The region with the highest refinement level is defined by $0 \leq z \leq 100$ Mm, $|x| \leq 2.33$ Mm and $y \leq 2.33$ Mm. Animations of these figures, showing the oscillations for the three models, are available in the online version of Karampelas et al. (2017, movies 1-3).

The effects of mixing are considered in a third case, where we introduced a temperature gradient across the tube axis. We briefly discuss the dynamics of our driven oscillating tubes, as well as the implication of their dynamical evolution on the spatial evolution of the loop heating.

3.2 Numerical models

3.2.1 Equilibrium

The basis of our $3D$ numerical models consists of a straight, density-enhanced magnetic flux tube, in a low-β coronal environment (see Fig. 3.1 for a connection of this model with a semi-circular loop). Our setup follows closely the one in Antolin et al. (2014), with the values of our physical parameters listed in Table 3.1. The index i (e) denotes internal (external) values.

Initially, the system is permeated by a uniform magnetic field $B_0 \approx 22.8$ G directed along the flux tube, meaning in the z direction. We take a continuous and steep radial profile for density, given by the relation:

$$\rho(x,y) = \rho_e + (\rho_i - \rho_e)\zeta(x,y), \tag{3.1}$$

$$\zeta(x,y) = \frac{1}{2}(1 - \tanh((\sqrt{x^2+y^2}/R - 1)\, b)), \tag{3.2}$$

Table 3.1: Values of principal physical parameters used in the simulations. The index i (e) denote internal (external) values.

Parameter	Value
Loop length (L)	200 Mm
Loop minor radius (R)	1 Mm
Loop density (ρ_i)	$2.509 \cdot 10^{-12}$ kg m^{-3}
ρ_i/ρ_e	3
Loop temperature (T_i)	$9 \cdot 10^5$ K
Magnetic field (B_z)	22.8 G
Plasma β	0.018

where $\rho_e = 10^9 \mu m_p$ cm^{-3} ($\mu = 0.5$ and m_p is the proton mass). By x and y we denote the coordinates in the plane perpendicular to the loop axis, z along its axis (Fig. 3.2) and b sets the width of the boundary layer. In our setups, we take $b = 20$, which gives us an inhomogeneous layer of width $\ell \approx 0.3R$. We choose a density ratio of $\rho_e/\rho_i = 1/3$, which is within the range of estimated ratios, as derived from observational data in Aschwanden et al. (2003). This ratio is expected to lead to a fast damping rate of the kink mode through resonant absorption, and thus is suitable for rapid transfer of energy from transverse to azimuthal motions.

The three different cases considered in the current work are:

1. A model of propagating waves in a loop continuously driven from the footpoint, with no temperature variation between itself and the background plasma (Driven-equalT model).

2. A model of propagating waves in a loop continuously driven from the footpoint, in hydrostatic equilibrium between itself and the background plasma, where we take a temperature ratio of $T_i/T_e = 1/3$ (Driven-diffT model).

3. A model of a standing wave in a loop with an initial velocity perturbation and no temperature variation between itself and the background plasma (Stand-equalT model).

These temperature profiles are very useful in dealing with the underlying heating mechanisms in the solar corona. By choosing a gradient of $T_i/T_e = 1/3$, we are effectively modelling a coronal loop during a cooling phase, as observed for loops in thermal non-equilibrium (Froment et al. 2015, 2017), and we can directly compare to previous work dealing with the structure and observational

signatures of transverse waves in coronal loops (Antolin et al. 2014; Antolin et al. 2017). Similarly, setting $T_i = T_e$ helps us identify the effects of the wave heating, no matter how subtle they might be. For the two models with no initial temperature variation ($T_i = T_e$), due to the pressure gradient between the tube and the environment, we introduced a slight decrease in the magnetic field within the tube, thus restoring total pressure equilibrium. The external Alfvén speed for all three models is equal to $v_{Ae} = 2224$ km s^{-1}. The internal Alfvén speed is $v_{Ai} = 1284$ km s^{-1} for the model with $T_i/T_e = 1/3$, and $v_{Ai} = 1276$ km s^{-1} for the two models with $T_i = T_e$.

3.2.2 Grid

The three dimensional magnetohydrodynamic (MHD) equations are solved using the MPI-AMRVAC code (Keppens et al. 2012; Porth et al. 2014), where Powell's scheme is employed to keep the solenoidal constraint on the magnetic field. We use the implemented second-order 'onestep' TVD method with the Roe solver and 'Woodward' slope limiter. Our domain dimensions, in Mm, are $(x, y, z) = ((-8, 8), (0, 8), (0, 100))$, with four levels of refinement present, which leads to an effective resolution of $512 \times 256 \times 64$. This translates into cell dimensions of $31.25 \times 31.25 \times 1562.5$ km, thus the resolution is higher in the $x - y$ plane, to resolve the small-scale phenomena that appear around the loop edge. The loop footpoint for each model is located at $z = 0$ and the apex at $z = 100$ Mm. Numerical resistivity is present in our model and has a value many orders of magnitude larger than the expected one in the solar corona, which can only be reduced through the use of an ever-more refined computational grid. Using a parameter study in all three models, we have estimated the maximum effective numerical resistivity ($\eta_{\rm nr}$) to be of the order of $8.5 \cdot 10^{-9}$ s (in CGS). These calculations give a Lundquist number:

$$S = \frac{4\pi}{c^2} \frac{lv}{\eta_{\rm nr}} \geq 2.1 \cdot 10^4, \tag{3.3}$$

and a corresponding resistive time scale is $\tau_{\rm nr} = 4\pi l^2/(c^2 \eta_{\rm nr}) = 1.65 \cdot 10^4$ s. Here we considered a characteristic velocity $v = 1.3$ Mm s^{-1} $\approx v_{Ai}$ and a characteristic length $l = 1$ Mm.

3.2.3 Driver

Our tubes are driven from the footpoint ($z = 0$ Mm), using a continuous, monoperiodic 'dipole-like' driver, inspired by the one used by Pascoe et al. (2010). The period of the driver is $P \simeq 2L/c_k \simeq 254$ s for both models, coinciding with

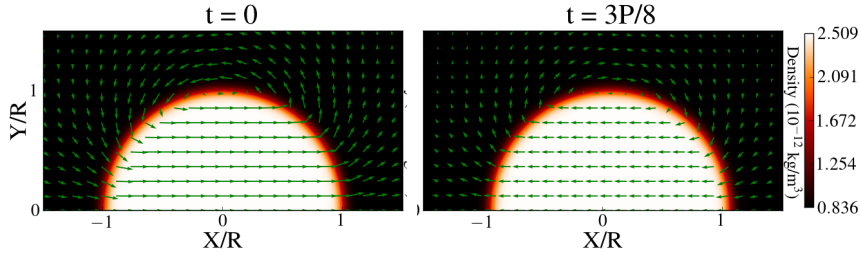

Figure 3.3: Contour of our tube density profile on the $x - y$ plane, at the footpoint. The vector field represents the spatial dependence of our driver for time (*left panel*) $t = 0$ and (*right panel*) $t = 3P/8$. $P = 254$ s is the driver period. The arrow lengths represent the normalized velocity, with respect to v_0, of our driver.

their corresponding fundamental eigenfrequency (Edwin & Roberts 1983). The Stand-equalT model also has the same fundamental eigenfrequency, as the other two models, enabling us to directly compare between the driven and non-driven oscillations.

The driver velocity is uniform inside the loop and time varying:

$$\{v_x, v_y\} = \{v(t), 0\} = \{v_0 \cos(\frac{2\pi t}{P}), 0\}, \tag{3.4}$$

where v_0 is the peak velocity amplitude. Here we choose $v_0 = 2$ km s^{-1}, which is close to the observed photospheric motions, like those caused by the buffeting action on flux tubes in the intergranular lanes by external granules (Hasan et al. 2000). Outside the loop, the velocity follows the relation:

$$\{v_x, v_y\} = v(t)R^2\{\frac{x^2 - y^2}{(x^2 + y^2)^2}, \frac{2xy}{(x^2 + y^2)^2}\}, \tag{3.5}$$

which mimics two-dimensional incompressible dipole plasma flows around a flux tube, which is moving with a $v_x = v_0$ velocity. This flow corresponds to the $m = 1$ mode in cylindrical coordinates (Pascoe et al. 2010). To avoid any numerical instabilities due to jumps in the velocity, a transition region between the two areas exists, the shape of which matches that of the density profile. Furthermore, our driver follows the movement of the tube, ensuring that the base of the tube and only that, is always inside the central region of uniform velocity (Fig. 3.3).

For comparison, we also ran a simulation with no driver but with an initial velocity perturbation (Stand-equalT model) of the form:

$$\{v_x, v_y, v_z\} = \{v(x, y, z), 0, 0\} = \{v_0 \cos(\frac{\pi z}{L})\, \zeta(x, y), 0, 0\}, \tag{3.6}$$

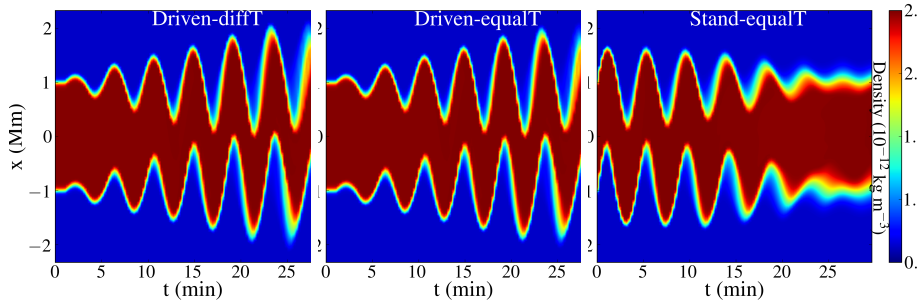

Figure 3.4: Time-distance maps of density at the apex for: (*left panel*) the Driven-diffT model, (*middle panel*) the Driven-equalT model and (*right panel*) the Stand-equalT model.

where $v_0 = 25$ km s^{-1}. This way, the loop is subject to a perturbation mimicking a fundamental kink mode.

3.2.4 Boundary conditions

For all three models, the velocity component parallel to the z axis (v_z) is antisymmetric at the bottom boundary in order to prevent flow of mass from the tube into, what would be, the photosphere (or 'out of the loop'). This allows us to focus on the effects of wave heating independently from the interaction with the different layers of the solar atmosphere. The rest of the physical variables there obey a Neumann-type, zero-gradient, condition, except the v_x and v_y velocities for the Driven- models, which are defined by the driver. Our aim is to study the fundamental standing kink mode for an oscillating flux tube. Taking advantage of this mode inherent symmetries, as well as the symmetric nature of our driver, we simulated only one quarter of the loop (Fig. 3.2). Along the axis, we went from one footpoint to the apex. We kept v_z, B_x and B_y antisymmetric, in the $x - y$ plane at the apex, while all the other quantities are symmetric. Additionally, we took into account the symmetric nature of our driver along the y axis, v_y and B_y are antisymmetric in the $x - z$ plane, while the other quantities are symmetric. Therefore, our computational time is reduced four-fold in total for all three cases. At the three lateral boundaries, we apply outflow (Neumann-type, zero-gradient condition) conditions, which allow waves to leave the domain. To minimize their influence on the dynamics, we placed them at a safe distance from the loop (8 R in the x and y direction).

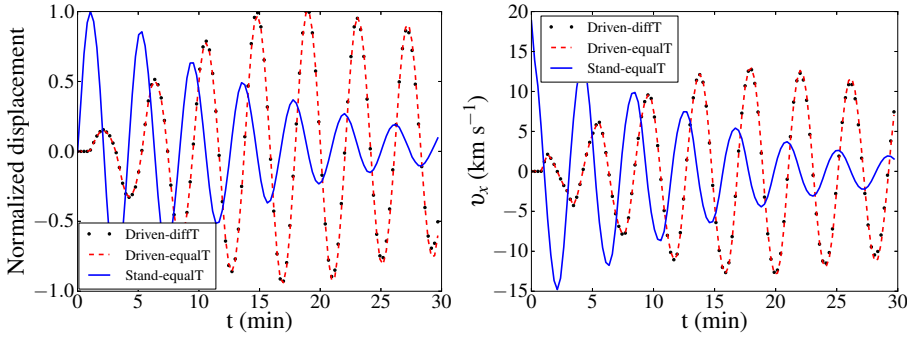

Figure 3.5: *Left panel*: Normalized amplitude of the loop displacement, for the three models, calculated by tracking the centre of mass at the apex ($z = 0$). *Right panel*: Through centre of mass tracking at the apex, we calculate the v_x velocity in km s^{-1}. The continuous line represents the tube oscillating as a standing wave with $T_e = T_i$ (Stand-equalT model), the dashed line represents the tube with the driver for $T_e = T_i$ (Driven-equalT model) and the dotted line the tube with the driver for $T_e = 3\,T_i$ (Driven-diffT model).

3.3 Results and discussion

For the rest of our analysis we focus on a sub-region of our computational domain, defined by $0 \leq z \leq 100$ Mm, $|x| \leq 2.33$ Mm and $y \leq 2.33$ Mm. This region exhibits the maximum effective resolution, and contains the loop for the whole duration of the simulation, for all three models. Inside this region, we defined the core of the loop, based on (Goossens et al. 2014), as the part of the tube cross-section where $\rho \geq 0.976\,\rho_i$. Furthermore, we defined the inhomogeneous layer of the tube ($0.335\,\rho_i < \rho < 0.976\,\rho_i$), the whole tube cross-section ($\rho > 0.335\,\rho_i$) and, the 'corona' ($\rho \leq 0.335\,\rho_i$), all inside the same region defined previously.

We ran all of our simulations for a total time of seven periods ($7P \sim 1782$ s). Focusing on the driven cases, the first waves to reach the apex ($z = 0$), after ≈ 150 s, are the azimuthal Alfvén waves at the boundary layer of our tube, thanks to their higher propagation speed, followed by the propagating kink waves. The period of the driver is equal to the analytically predicted value for the standing fundamental kink oscillations of a uniform flux tube for our given densities (Edwin & Roberts 1983). Considering the symmetry at the apex, the propagating waves from each footpoint superpose, forming a standing wave. By choosing that corresponding frequency for our driver, we forced the loop to perform an oscillation resembling the fundamental standing mode for the kink

wave, with the site of the loop apex being the location of the antinode of the x-velocity. The animations of the tube oscillations for all three of our models are shown in the electronic version of Karampelas et al. (2017), for Fig. 3.2.

In Fig. 3.4, we have the time-distance maps of the density at the apex, for our three different cases. By examining them, we can see that, for the models with the driver, the oscillation seems to saturate after reaching its peak value in amplitude, around $t \sim 1200$ s. After that point, the inner, denser part of both oscillates with a smaller amplitude, while the lower density edges maintain the maximum amplitude of the oscillation. The same drop in oscillation amplitude is present in Fig. 3.5, where we plot the normalized transverse displacement as well as the v_x velocity (given in km s^{-1}), for the centre of mass at the apex. We see that the amplitude of the oscillation, for the driven cases, reaches a maximum after ~ 4.5 periods (of the driver), in agreement with the time distance maps for the density. The same lower density region at the edge of the tube also develops at later times for the Stand-equalT model. The normalized display and the centre of mass velocity also reveal a damping profile, in agreement with previous works (Magyar et al. 2015; Magyar & Van Doorsselaere 2016).

As mentioned before, the superposing propagating waves quickly form a footpoint driven standing wave with a velocity antinode at the apex, which can be Kelvin-Helmholtz unstable (Heyvaerts & Priest 1983; Zaqarashvili et al. 2015). In fact, approximately two periods time after the apex started to oscillate, the Kelvin-Helmholtz instability (KHI) manifests there because of the high shear velocities (Terradas et al. 2008; Antolin et al. 2014, 2015; Antolin et al. 2016; Magyar et al. 2015; Magyar & Van Doorsselaere 2016). From a linear analysis of a simplified model resembling ours, (following the analysis of Terradas et al. 2008) we find a growth rate for the instability equal to $0.248\,P$, for shear velocity ≈ 18 km s^{-1}. In Fig. 3.6, we plot the spatial profiles of the temperature and density for our three models, at the apex. The KHI develops, creating strong shear flows and smaller scales, in addition to spatially extended eddies, the Transverse Waves Induced Kelvin-Helmholtz (TWIKH) rolls. These TWIKH rolls result in extensive mixing of plasma from the loop, with the surrounding corona, as indicated by the profiles of temperature (T) and density (ρ) at the apex. This extended turbulent layer is the low density tube edge, which we saw developing in Fig. 3.4.

Focusing on the Driven-equalT and Stand-equalT models, we observe the manifestation of temperature fluctuations at the tube layer. These perturbations appear immediately after the tubes are set in motion, and are getting stronger once the Kelvin-Helmholtz instability sets in, as seen in Fig. 3.6. They are connected to the density and pressure fluctuations and are not the result of energy transfer between those different regions. Antolin et al. (2017) also observed these temperature perturbations for a flux tube oscillating as a standing

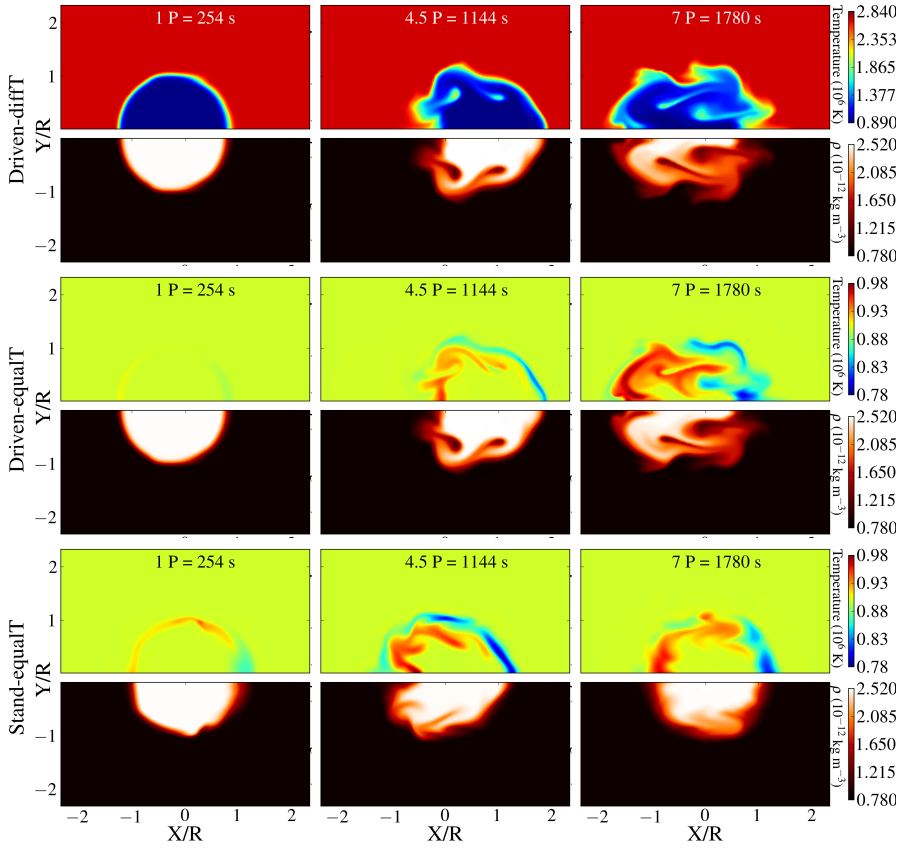

Figure 3.6: Cross-section of the apex ($z = 0$) showing the (*upper half*) temperature and (*lower half*) density profile for the three different models we studied. From top to bottom rows: (a) the Driven-diffT model, (b) the Driven-equalT model and (c) the Stand-equalT model.

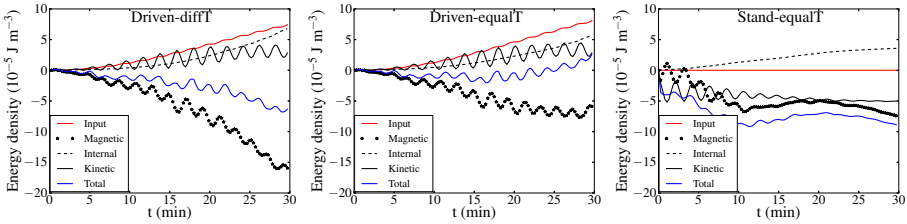

Figure 3.7: Time profiles for the internal, magnetic and kinetic energy density variations relative to the initial state, the total (internal + magnetic + kinetic) energy density difference and the energy density provided by the driver. All the quantities are volume averaged for the region with $0 \leq z \leq 100$ Mm, $|x| \leq 2.33$ Mm and $y \leq 2.33$ Mm. From left to right: (a) the Driven-diffT model, (b) the Driven-equalT model and (c) the Stand-equalT model.

wave, and characterized them adiabatic in nature. Thus, we refer to this mechanism as adiabatic heating (and cooling). Here, we prove that similar patterns for adiabatic cooling and heating appear, both for a tube with a standing oscillation and for a footpoint driven one. Adiabatic in nature temperature fluctuations can also be observed at the footpoints of our models as well, but they are more uniform and extended, probably originating from the large scale loop dynamics caused by the standing (or standing-like) oscillations. These adiabatic processes are existing alongside other heating mechanisms, which we are studying in the current work.

In order to investigate the drop of the normalized driven oscillation amplitudes, in Fig. 3.7 we plot the perturbations in internal and magnetic energy densities, the kinetic energy density and the total input energy densities for our models. Focusing on a region of constant volume, the changes in the energy densities are directly translated into changes in the energies. The total energy density (in J m^{-3}) provided by the driver, following Beliën et al. (1999), is calculated from the formula:

$$S(t) = -\frac{1}{V}\int_0^t \int_A \mathbf{S} \cdot d\mathbf{A} dt', \tag{3.7}$$

where $\mathbf{S}$ is the Poynting flux from the lower boundary ($x - y$ plane), where the driver is located. $\mathbf{A}$ denotes the surface element (of the lower $x - y$ boundary plane) and V is the total volume of the studied region. As we see from the diagrams of energy, the input in the Driven-diffT and Driven-equalT models are very similar, as it was expected. The kinetic energy density shows a saturation in both cases after a time around 20 min., that is in agreement with what we saw in the time density maps for the density. The fact that the kinetic energy saturates, indicates that the previously mentioned drop in the normalized amplitude (see

Fig. 3.5) is not caused by an actual drop of the oscillation amplitude, but rather by the development of smaller scale motions in the loop cross-section, which affect the position of the centre of mass.

It is also interesting to note here that the input energy, while sufficient to explain the rise of the kinetic energy, is less than the sum of internal and kinetic energy. The extra energy seems to be provided by the drop of the magnetic energy, due to the existence of the effective numerical resistivity. The same drop is higher in the case of the Driven-diffT model, but it does not drastically increase the internal energy for that model. As result, both models with the footpoint driver are expected to have very similar dynamical evolution over time. For the Stand-equalT model, the input is practically zero, as expected, and both the kinetic and magnetic energies decrease in time.

We note here the different behaviour of the magnetic energy density difference between the three models. In all three models, not all of the available magnetic energy density turns into internal energy. From the equation for the energy density evolution in resistive MHD, we see the existence of a resistive source term, and of fluxes. The resistive term is the one responsible for transforming the magnetic energy into internal energy, while the fluxes transfer energy into ('Input' in Fig. 3.7) and out of our domain. The Poynting flux through the side boundaries, which are simulated as open, is responsible for the extra drop of the magnetic energy.

For the cases of uniform temperature, only a small part of the magnetic energy density is dissipated this way, as we can see by comparing its drop to the rise of the internal energy density. For these two cases, the magnetic energy density drops at almost the same levels, due to the identical initial conditions for the magnetic fields and the plasma pressure in these two models. The long-term oscillatory behaviour of the Stand-equalT model magnetic energy density is caused by the initiation of the slow wave, which was mentioned before. The small rise observed near the end of the simulation for the magnetic energy of the Driven-equalT model is caused by the continuous energy input from the driver. However, the Driven-diffT model exhibits a greater drop, when compared to the other two cases. This drop cannot be adequately explained by the bigger rise of internal energy for that model (Fig. 3.7), and is caused by the stronger Poynting flux through the side boundaries. Finally, we need to stress that the effects of numerical resistivity, as well as the inevitable development of non-zero $\nabla \cdot B$ were taken into account during our analysis.

In Fig. 3.8 we plot the difference of the volume averaged temperature and of the volume averaged internal energy relative to the initial state, over the area defined by $0 \leq z \leq 100$ Mm, $|x| \leq 2.33$ Mm and $y \leq 2.33$ Mm, for all three models. We see that for the Driven-equalT and Stand-equalT models, both

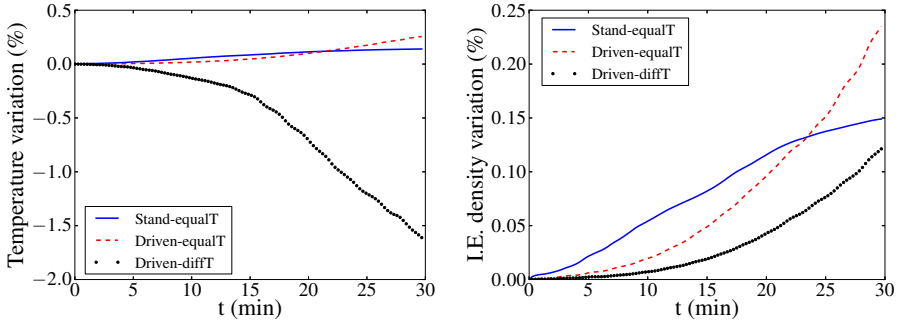

Figure 3.8: Percentage of the: (*left panel*) volume averaged temperature variation and (*right panel*) volume averaged internal energy variation, over a greater region (tube+corona) including the loop ($0 \leq z \leq 100$ Mm, $|x| \leq 2.33$ Mm and $y \leq 2.33$ Mm). The continuous line represents the Stand-equalT model, the dashed line represents the Driven-equalT model and the dotted line the Driven-diffT model.

the temperature and internal energy show the same relative increase. This is consequence of the heating mechanisms present in our simulations, which we are going to further study in the next figures. In the case of the Driven-diffT model, the temperature exhibits a drop larger than 1.5% while the internal energy density shows a rise of about 0.12%. As we explain later, this is due to the mixing between the cold tube and the hotter environment, that we considered in that particular model.

To further study the differences in the internal energy - temperature connection among our models, we will examine the temperature profiles along the z-axis, over time, in Fig. 3.9. For the model of the driven standing wave inside the tube in temperature equilibrium, we observe a gradual increase of the average temperature over time ($\sim 3.4\%$), the closer we get to the footpoint. The temperature towards the apex increases as well, but by a relatively smaller amount. A similar behaviour is obtained by the temperature profiles of both the greater region (tube + corona) and for the surrounding corona. Regarding this model, the lower changes in the average temperature for the 'tube + corona' area and for the surrounding corona are attributed to the larger area studied, while the heating is located only inside and at the boundary of the loop. This is also in agreement with our findings in Fig. 3.8 for this model.

Studying the corresponding temperature profiles for the standing oscillating loop, we observe again the highest average temperatures towards the footpoints. The new phenomenon that we did not encounter in the previous case, is a long

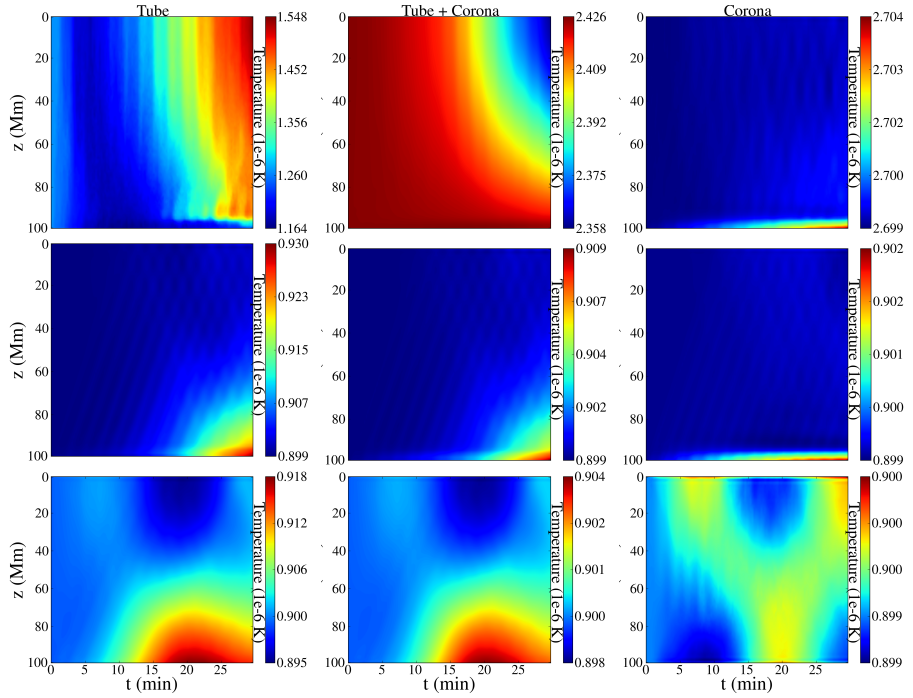

Figure 3.9: Average temperature along the z-axis: (*left column*) inside the tube (for $\rho \geq 0.84 \cdot 10^{-12}$ kg m^{-3}), (*centre column*) for the whole greater region (tube+corona) including the loop ($0 \leq z \leq 100$ Mm, $|x| \leq 2.33$ Mm and $y \leq 2.33$ Mm) and (*right column*) for the surrounding plasma outside the loop. From top to bottom: (a) the Driven-diffT model, (b) the Driven-equalT model and (c) the Stand-equalT model. The apex is located at $z = 0$.

period oscillation of the average temperature. This oscillation, mostly prominent at the apex, is due to the longitudinal slow mode triggered by the large initial velocity perturbation (Terradas et al. 2011; Magyar & Van Doorsselaere 2016). In the case of the driven waves, this mode is not observed, the reason being probably the gradual energy input from the footpoint. Despite the presence of this mode, however, the temperature profile for the tube oscillating as a standing wave still indicates heating along a large part of the loop, with the highest temperatures seen towards the footpoint. As before, the same temperature evolution is observed in the greater region, whereas a similar trend is observed in the surrounding corona, although affected by the effects of the long period slow mode.

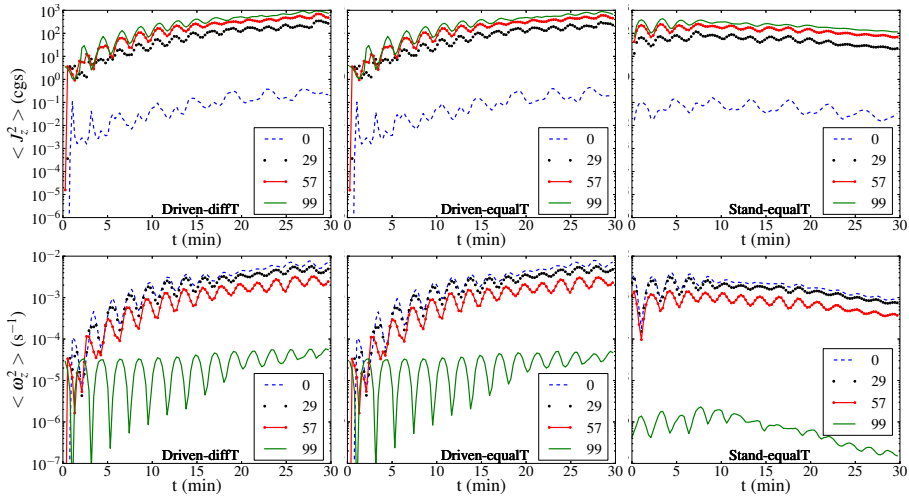

Figure 3.10: Top and bottom panels correspond to time profiles for the average square z-current density J_z^2 and the average square z-vorticity ω_z^2, respectively, at different heights. The apex is located at $z = 0$ and the volume averaging takes place only inside each tube ($\rho > 0.335\,\rho_i$). From left to right: (a) the Driven-diffT model, (b) the Driven-equalT model and (c) the Stand-equalT model.

Before addressing the Driven-diffT model, we will try to recognize the different dissipation mechanisms involved by plotting, in Fig. 3.10, the average square z-vorticity (ω_z^2) and the average square z-current density (J_z^2) for different heights inside our three different loops. These plots are focused on the area inside the tubes, defined by density $\rho > 0.335\,\rho_i$. It is obvious from all three models that the square z-vorticity gains its highest values at the apex, which is the position of the velocity antinode and the part of the loop where the Kelvin-Helmholtz generated turbulence is the strongest. The higher velocities observed there, due to the larger amplitude of the oscillation, lead to greater values of the squared z-vorticity. This can also be verified by the periodicity of ω_z^2. Its period is half that of the wave, which gives a period for the ω_z vector equal to that of the wave. Also, for the Stand-equalT model, we observe a drop of the vorticity oscillation amplitude, as well as of its mean value. This is mainly due to damping of the kink wave. The square z-vorticity also seems to be connected to the induced turbulence in our tubes. As the tubes start oscillating, the minimum values of ω_z^2 grow and gain non-zero values through the creation of smaller scale structures (like TWIKH rolls). This, 'base value' is larger at the apex, where the KHI, and the induced turbulence, are at their strongest. Therefore, ω_z^2 can be used as a measure of turbulence.

The z-current density, however, is increasing towards the footpoint, where it becomes three orders of magnitude larger than at the apex, for all three models. This consistency is caused by the geometry of the resulting oscillations. As we have already mentioned, after the superposition of the counter-propagating waves from each footpoint, we have the manifestation of a footpoint driven standing wave which resembles the fundamental standing kink mode of the flux tube. By writing the magnetic field and the current density in cylindrical coordinates, we see that the main contribution on J_z is from the radial variation of azimuthal component of the magnetic field $\partial B_\phi / \partial r$, which for the case of the fundamental kink mode has a cosine dependence along the z axis, following B_ϕ. Thus, the z-current density will get its highest values near the footpoints of such oscillating loops (Van Doorsselaere et al. 2007). As we mentioned in the introduction, in that paper, Van Doorsselaere et al. have proven that for line-tied loops the viscous and resistive heating mechanisms can be observationally distinguished by the site of the heating. Ohmic dissipation, due to resistivity, is more prominent at the footpoints of oscillating loops, while viscous dissipation is stronger towards the apex. Combining the above with the value of the resistive time scale for our models, we conclude that in both equalT-models, the stronger rise of temperature at the footpoint is an indication of Ohmic heating due to numerical resistivity. The lower increase of the average temperature at the apex could be potentially caused by viscous dissipation. However, the temperature gradient between the apex and the footpoint, for these two models, suggests that resistive heating is the dominant heating mechanism in our models.

For the model of the driven wave inside the tube with a temperature gradient, from Fig. 3.9, we observe a gradual increase of the average temperature over time, the closer we get to the apex. This phenomenon seems to contradict the results we have got so far about the wave heating mechanisms, since this model is dynamically the same as the model of propagating waves inside the tube in temperature equilibrium. It is however consistent with the findings of Magyar & Van Doorsselaere (2016) for the standing kink, where it was observed that the internal energy rise at the layer was not enough to explain the rise of the temperature at the layer. Initially, as we see in Fig. 3.11, for this model, the hotter boundary layer ($0.335\,\rho_i < \rho < 0.976\,\rho_i$) shrinks over time. The overall volume of the tube is reduced and an initial drop of the volume average temperature inside the tube is caused, since the relative contribution from the colder inner parts of the loop increases. As the simulation runs, however, the development of the turbulence and the manifestation of the TWIKH rolls lead to extensive mixing with the surrounding area, expanding the turbulent layer both inwards and outwards. The shrinking of the colder core region and the expansion of the hot turbulent layer is what causes the tube to become hotter over time. It is no coincidence that the greatest rise of temperature takes place at the apex, where the average vorticity (or in our case the average square vorticity)

takes its highest values, as seen in Fig. 3.10. The apex is the location of the velocity antinode, where the oscillation amplitude and the induced turbulence are the strongest. Therefore, the mixing is also more extensive there, leading to a further apparent temperature increase of the loop. The footpoint ($z = 0$) does not show any rise in temperature. On the contrary, the shrinking of the hotter layer, and thus the increase of the colder core contribution, drops the temperature to a point where Ohmic heating, which is also present in this model, is not adequate to sustain the initial average temperature.

Studying the greater area ($0 \leq z \leq 100$ Mm, $|x| \leq 2.33$ Mm and $y \leq 2.33$ Mm) for the Driven-diffT model in Fig. 3.9, we observe a temperature drop close to the apex. This behaviour, which is also connected to our findings in Fig. 3.8, is caused by the extensive mixing between the loop and the hotter (in this model) environment. The temperature profile has the opposite evolution than before, decreasing near the apex and increasing near the footpoint. This is a confirmation of the assumption about the mixing. Through the loop expansion, both the colder core as well as the warm layer contribute more to the average temperature, than they initially did. Both the layer and the core are colder than the surrounding plasma. This causes the volume average temperature to drop. However, this does not mean that the environment cools down. From the temperature spatial profiles in Fig. 3.6, we can see a rise in temperature of the surrounding plasma, as we approach the turbulent layer. Plotting the average temperature along the z-axis over time (Fig. 3.9), for the surrounding area, this slight heating of the corona becomes obvious. It is worth noting that even in this case, the footpoint reaches slightly higher temperatures than the apex, which again can be explained through the effects of resistive heating at the tube-corona interface, at the edges of the boundary layer.

The Driven-equalT model also exhibits the same evolution regarding the different areas studied, but unlike the Driven-diffT model, the changes of the tube cross-section do not affect the average temperature of each region. Instead, the wave dissipation mechanisms, in particular resistive heating, are the ones responsible for the temperature fluctuations. The same is valid also for the tube oscillating as a standing wave. Finally, we stress that the results of the mixing on the apparent heating (cooling) of the tube (tube + environment) depend on the temperature gradient between the environment and the loop; they could significantly change should we consider different initial temperature gradients.

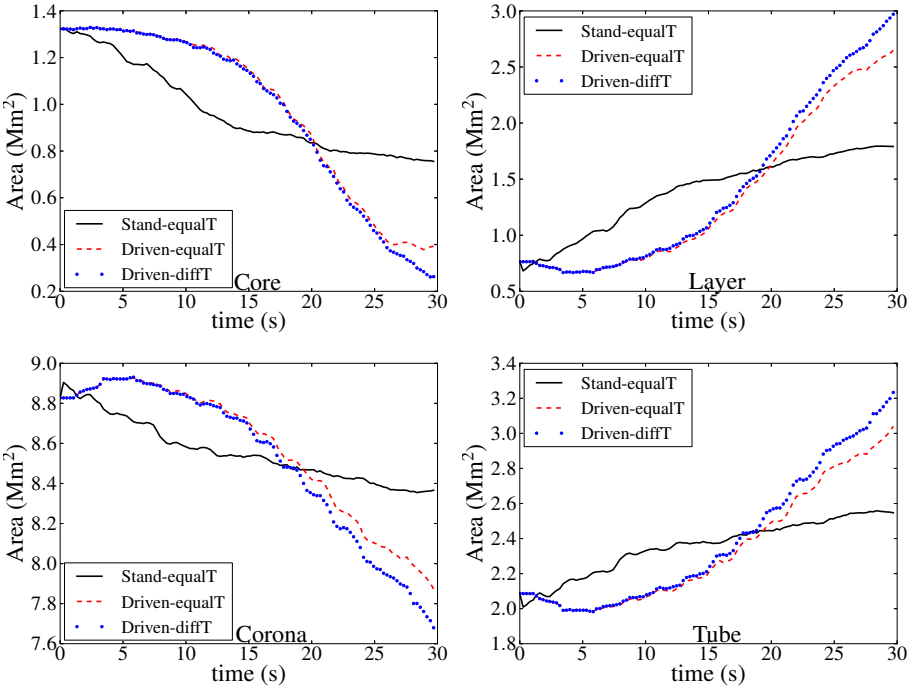

Figure 3.11: Time evolution of the core ($\rho \geqslant 0.976\,\rho_i$), layer, corona ($\rho \leqslant 0.335\,\rho_i$) and whole tube ($\rho > 0.335\,\rho_i$) surface areas (in Mm^2) for our three loops, at the apex. The continuous line represents the Stand-equalT model, the dashed line represents the Driven-equalT model and the dotted line the Driven-diffT model.

3.4 Conclusions

We were interested in studying the heating produced by transverse waves in coronal loops. We performed numerical simulations for a 3D, density enhanced straight tube, by solving the MHD equations. Numerical resistivity is present in our model, and has an effective value many orders of magnitude larger than the expected values in the solar corona. We studied two models of driven standing waves, for a continuous, monoperiodic, footpoint driver. One model had a uniform temperature throughout the domain, while the other had a temperature difference between the loop and the environment. The velocity amplitude of our driver was of the order of 2 km s^{-1}, while the period of the driver was equal to the analytically predicted value for the standing fundamental kink oscillations

of a uniform flux tube for our given densities (Edwin & Roberts 1983). By choosing that corresponding frequency for our driver, and considering symmetry at the apex, the initially generated propagating waves superpose and form the fundamental standing mode of a kink oscillation. As predicted by the theory of driven mechanical oscillations, the original increase of our oscillation amplitude and of the corresponding v_x velocity, due to the continuous input of energy, gave way to a saturation point in both models. The noticeable difference in the magnetic energy density profiles between the two models did not seem to affect the dynamics of the two systems. Notably, the internal energy density variation relative to the initial state, as well as the kinetic energy density were similar in both models. Additionally, considering a uniform temperature model of a tube oscillating as a standing wave, with an initially sinusoidal perturbation in the velocity, we reproduced a damping profile similar to those in Magyar & Van Doorsselaere (2016).

For all three of our models, we reported the creation of turbulence at the edges of our loop and the development of Transverse Waves Induced Kelvin-Helmholtz (TWIKH) rolls. These rolls resulted in extensive mixing of plasma between the inner loop and the surrounding corona, as shown in the profiles of temperature (T) and density (ρ) at the apex. By considering an initial temperature equilibrium between the loop and the environment, we see that the KHI produces both a temperature increase and a decrease in the turbulent layer. These temperature fluctuations take place at the location of the TWIKH rolls and, as reported by Antolin et al. (2017), they are not caused by the transfer of energy between the different TWIKH rolls. Instead they are connected to the pressure and density fluctuations caused by the turbulence, thus being adiabatic in nature. Similar temperature fluctuations can be observed at the footpoints of our uniform-temperature models as well, likely caused by the large scale dynamics due to the waves examined.

In the two models with the uniform initial temperature, the increase of the volume averaged energy density of the tubes was the same in percentage to the corresponding rise in temperature. This proved that there is indeed a wave dissipation mechanism that causes conversion of magnetic and kinetic energy to thermal energy. Studying the temperature profiles along the loop axis and over time, we observed a site of heating near the loop footpoints that is present both in the case of the driven standing wave and the impulsively excited standing wave. The profiles of the square volume averaged z-current density near the footpoints (three orders of magnitude higher at the footpoint than at the apex), indicated a strong contribution of Ohmic heating, due to numerical resistivity. A careful study of the temperature profiles for the case of the driven oscillation indicated a slight increase of temperature near the apex, were the turbulence is the strongest, and the square z-vorticity gets its highest values for all of

our models. These higher values near the apex, are due to both the higher velocities encountered there and the creation of more prominent smaller scale structures, such as TWIKH rolls. Further studies must be done in order to estimate the contribution from viscous heating there, as well as the effects of actual, physical, resistivity. However, the greater increase of the average temperature that is observed near the footpoints, is caused by the currents generated at the turbulent layer. This suggests that resistive dissipation is the main mechanism for heating (Van Doorsselaere et al. 2007).

For the model without the driver, we end up with the same preference of resistive over viscous heating, with the highest temperatures and z-current densities observed near the footpoint. The observed long period oscillation of the temperature in this case, is due to the longitudinal slow mode initiated, triggered by initial the perturbation (Magyar & Van Doorsselaere 2016). In the case of the driven standing waves, this mode was not observed in our models, probably because of the gradual energy input from the footpoints. The overall lower available energy from the standing oscillation, alongside the effects of the observed slow mode, eventually led to a lower increase of the loop volume averaged temperature. In comparison, despite their slower initial heating, the driven waves produced higher temperatures after the oscillations entered their assumed saturation point.

Finally, testing the effects of temperature variation between the flux tube and the environment for the driven oscillations, we observed that the perturbation in the internal energy and the evolution of the temperature follow different profiles over time. We reached the conclusion, that extensive mixing between plasmas of different temperatures can potentially hide the effects of the wave heating mechanisms. This apparent heating (or cooling, not considered here) is generally determined by the initial temperature difference between the flux tube and the environment, meaning that varying results should be expected for different gradients. This has to be taken into account when dealing with observations, since a higher calculated temperature would not necessarily mean actual heating of the whole loop-atmosphere system. In our model of propagating waves of a cold tube in a hotter environment, the rise of temperature was the highest at the apex, where the z-vorticity also took its highest values. The resulting temperatures were far greater than those produced by the wave heating in the model of temperature equilibrium, in agreement with Magyar & Van Doorsselaere (2016).

Chapter 4

Simulations of fully deformed loops

Prof. Smith: *I want you to xxxxx the yyyyyy data using the zzzzz formula for wwww integral and vvvvv coding.*
Doctoral student: *Yes, of course Prof. Smith*
Doctoral student (to himself): *What did all those terms mean????*
PHD Comics,
http://phdcomics.com/comics/archive.php?comicid=2023

Abstract
In this chapter, we study the importance of KHI in addressing the expected confinement of energy dissipation, near the outer layers of loops, leaving their denser inner parts without a heating mechanism. Using the MPI-AMRVAC code, we performed ideal, three dimensional MHD simulations of footpoint driven transverse oscillations of a cold, straight coronal flux tube, embedded in a hotter environment. The developed Transverse Wave Induced Kelvin-Helmholtz (TWIKH) rolls expand throughout the tube cross-section, and cover it entirely. This alters the initial monolithic density profile, leading to a fully deformed cross section. As a consequence, both the resistive and viscous heating rate increase over the entire loop cross section. The resistive heating rate takes its maximum values near the footpoints, while the viscous heating rate at the apex. We conclude that even a monoperiodic driver can spread wave heating over the whole loop cross section, potentially providing a heating source in the inner loop region. Despite the loop's fully deformed structure, forward modelling still shows the structure appearing as a loop.

This chapter is based on Karampelas & Van Doorsselaere (2018).

4.1 Introduction

Heating of coronal loops by transverse magnetohydrodynamic (MHD) waves has been an extensively studied topic ever since the proof of their ubiquity in the solar atmosphere (Aschwanden et al. 1999; Tomczyk et al. 2007). The main theory of wave damping is based on the mechanism of resonant absorption for the case of standing and propagating waves (Ionson 1978; Goossens et al. 1992; Arregui et al. 2005; Terradas et al. 2010; Goossens et al. 2011; Pascoe et al. 2010; De Moortel et al. 2016). In both mechanisms the energy of the large-scale oscillation is transferred, through resonance, to local azimuthal Alfvén modes. In the case in which multiple frequencies are excited, smaller scales are created through phase mixing (Heyvaerts & Priest 1983; Soler & Terradas 2015). By including dissipation mechanisms, such as resistivity or viscosity, resonant absorption and mode coupling can lead to heating (Ofman et al. 1998; Pagano & De Moortel 2017).

However, the effects of wave heating by global oscillations were expected to be confined in the resonant layer. As shown in Cargill et al. (2016), this localized heating is not capable of sustaining a fixed density gradient between the loop and the environment. Radiative cooling will inevitably lead to draining of the loop's denser inner parts, unless additional heating mechanisms are considered. A possible solution could be the use of a broad-band driver for transverse waves. In such a case (Ofman et al. 1998), we would see the development of multiple narrow resonance layers. These layers can move across the loop cross-section as the density profile changes, but heating would still be concentrated in near-discrete locations.

The previous issue could also be potentially addressed by the Kelvin-Helmholtz Instability (KHI) for standing modes in closed coronal structures (Heyvaerts & Priest 1983; Zaqarashvili et al. 2015). Its existence is predicted by three dimensional simulations in straight flux tubes for driver generated azimuthal Alfvén waves (Ofman et al. 1994c; Poedts et al. 1997), impulsively excited standing kink modes (Terradas et al. 2008; Antolin et al. 2014; Magyar et al. 2015; Magyar & Van Doorsselaere 2016; Howson et al. 2017b), and footpoint driven standing kink modes (Karampelas et al. 2017). The KHI creates a turbulent layer at the loop edges, where resonant absorption and phase mixing can effectively transfer energy to smaller scales. However, even if enough energy is provided to the system, its heating would still be mainly localised in the edge of the loop.

Recently, decayless low-amplitude kink oscillations have been discovered in coronal loops (Nisticò et al. 2013; Anfinogentov et al. 2015). The KHI could play an important role in this physical phenomenon, since the observations suggest that the decayless waves are also standing waves with an average amplitude of ~ 0.2 Mm, but lower than 1 Mm. Antolin et al. (2016) have proposed line-of-sight (LOS) effects due to the KHI and limits in the spatial resolution of our observations, as the cause of this observed decayless motion. Another proposal is the development of standing waves through a driving mechanism near the loop footpoints (Nakariakov et al. 2016), like those simulated in Karampelas et al. (2017).

In the current study, we have expanded on our previous work, aiming to model the low-amplitude, decayless kink waves in active region coronal loops, driven by footpoint motions. In our previous study (Karampelas et al. 2017), we had concentrated on the longitudinal dependence of the heating rate by the Transverse Wave Induced Kelvin-Helmholtz (TWIKH) rolls. Here, however, we have concentrated on an interesting result about the spatial evolution of a loop cross section for standing kink waves generated by footpoint drivers. In particular, we are going to study the effects of the TWIKH rolls on the cross-sectional density profile and the location of wave heating in the cross section of the loop.

4.2 Numerical model

We simulate footpoint-driven transverse waves in a $3D$ straight, density-enhanced magnetic flux tube, in a low-β coronal environment. Our setup follows the work of Karampelas et al. (2017), with a loop length $L = 200$ Mm and a minor radius $R = 1$ Mm. The loop density is equal to $\rho_i = 2.509 \cdot 10^{-12}$ kg m^{-3}, and the loop temperature is $T_i = 9 \cdot 10^5$ K. The index i (e) denotes internal (external) values. The magnetic field is $B_z = 22.8$ G and the plasma $\beta = 0.018$. The density profile consists of the continuous function:

$$\rho(x,y) = \rho_e + 0.5\ (\rho_i - \rho_e)\ \{1 - \tanh\left(\left(\frac{\sqrt{x^2+y^2}}{R} - 1\right) b\right)\}, \qquad (4.1)$$

where x and y denote the co-ordinates in the plane perpendicular to the loop axis, z along its axis. For $b = 20$ the inhomogeneous layer has a width $\ell \approx 0.3R$. The density ratio of $\rho_e/\rho_i = 1/3$, inspired by observational data in Aschwanden et al. (2003), leads to swift transfer of energy from transverse to azimuthal motions. In Karampelas et al. (2017) it was found that the dynamics of the oscillations are not sensitive to the value of the temperature ratio. In the current

setup we have effectively modelled a coronal loop during its cooling phase, by choosing a gradient of $T_i/T_e = 1/3$. The external and internal Alfvén speeds are equal to $v_{Ae} = 2224$ km s^{-1} and $v_{Ai} = 1284$ km s^{-1}.

As in the previous study, we have used the MPI-AMRVAC code (Porth et al. 2014), with an effective resolution of $512 \times 256 \times 64$. Since our domain dimensions are $(x, y, z) = (16, 8, 100)$ Mm, the cell dimensions are $31.25 \times 31.25 \times 1562.5$ km. The numerical resistivity is estimated to correspond to a Lundquist number of $S \geq 2.1 \cdot 10^4$.

As before, the tube is driven from the footpoint ($z = 100$ Mm) with the kink period of $P \simeq 2L/c_k \simeq 254$ s (Edwin & Roberts 1983). The driver velocity, at the bottom boundary, is uniform inside the loop and time varying as follows:

$$\{v_x, v_y\} = \{v(t), 0\} = \{v_0 \cos(2\pi t/P), 0\}, \tag{4.2}$$

where v_0 km s^{-1} is the peak velocity amplitude. We considered two different cases, one for a driver with a peak velocity of $v_0 = 2$ km s^{-1}, and one with $v_0 = 0.8$ km s^{-1}. Outside the loop, the velocity follows the relation:

$$\{v_x, v_y\} = v(t)R^2\{\frac{x^2 - y^2}{(x^2 + y^2)^2}, \frac{2xy}{(x^2 + y^2)^2}\}, \tag{4.3}$$

with a smooth transition region between the two areas, matching the outer layer of the cylindrical tube. Following Karampelas et al. (2017), we also set the velocity component parallel to the z axis (v_z) antisymmetric at the bottom boundary, to prevent mass flow through it. The driver sets the values for v_x and v_y at the bottom boundary, while all the other quantities obey a Neumann-type, zero-gradient condition there. Using the given driver frequency ensures that the superposing propagating waves (originating from each footpoint) form the fundamental standing kink mode for our tube. Taking advantage of the symmetric nature of the kink mode, we kept v_z, B_x, and B_y antisymmetric in the $x - y$ plane at the top boundary (apex, $z = 100$ Mm), while all the other quantities are symmetric. Furthermore, through the symmetric nature of our driver we set v_y and B_y antisymmetric in the $x - z$ plane, while the other quantities are symmetric. Therefore, we only simulated one fourth of our tube, as shown in Fig. 4.1. In the rest of the boundaries, a zero-gradient condition was used for all the quantities.

4.3 Results

For the rest of our analysis we focus on the sub-region of our computational domain, defined by $0 \leq z \leq 100$ Mm, $|x| \leq 2.33$ Mm and $y \leq 2.33$ Mm, where

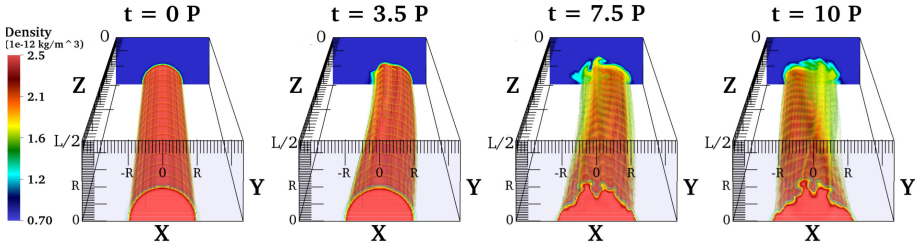

Figure 4.1: Density structure of the flux tube, for a driver with $v_0 = 2$ km s^{-1}. Snapshots are taken for times $t = 0$, $3.5\,P$, $7.5\,P$ and $10\,P$, where $P \simeq 254$ s is the driver period. The loop length is $L = 200$ Mm and the loop radius is $R = 1$ Mm. An animation of this figure, showing the oscillation for our model, is available in the online version of Karampelas & Van Doorsselaere (2018).

the resolution is the highest. We ran a simulation for a total time of ten driving periods ($10\,P \sim 2540$ s).

The loop apex, which is the location of the antinode of the x-velocity, is Kelvin-Helmholtz unstable, as expected from theory (Heyvaerts & Priest 1983; Zaqarashvili et al. 2015). As we see in Fig. 4.2, the KHI manifests at the apex. In addition to that, we have the formation of spatially extended eddies, the TWIKH rolls. A similar feature can be seen in Fig. 4.3, where we show the density cross-section of our tube at the apex for the driver with peak velocity $v_0 = 0.8$ km s^{-1}. The TWIKH rolls are now less prominent, due to the smaller driver velocity amplitude, which leads to slower increase of the shear velocities at the apex. However, letting the driver act for more periods also leads to a deformed cross section at the apex.

By performing forward modelling with the FoMo code (Van Doorsselaere et al. 2016), we observe the manifestation of strand-like structures due to the out-of-phase movements of the TWIKH rolls, which we also see in Fig. 4.1. These strands, resembling those in Antolin et al. (2016) for the impulsively excited standing kink waves, are depicted in Fig. 4.4. Here, we present snapshots of the emission intensity for the Fe XII 193.509 Å line, at times $t = 0$, $3.5\,P$, $7.5\,P$ and $10\,P$. In our setup, the chosen line is better suited to detect the hotter plasma at the loop edge (Antolin et al. 2017). The colour-scale is limited between the minimum and the maximum intensity values of the integrated intensity of the simulations. We consider a line-of-sight plane perpendicular to the loop axis and we set the LOS angle perpendicular to the oscillation direction equal to 0°. By choosing the given LOS angle and studying only the emission intensity, we avoid any missed emission from performing forward modelling in only half the loop cross-section.

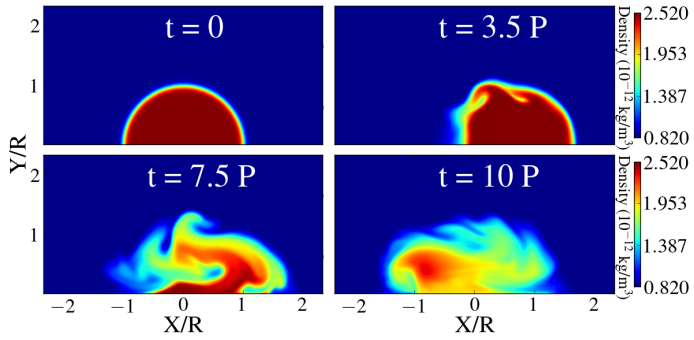

Figure 4.2: Snapshots of density (10^{-12} kg m^{-3}) of the flux tube cross-section at the apex ($z = 0$), for a driver with $v_0 = 2$ km s^{-1}. $P \simeq 254$ s is the driver period.

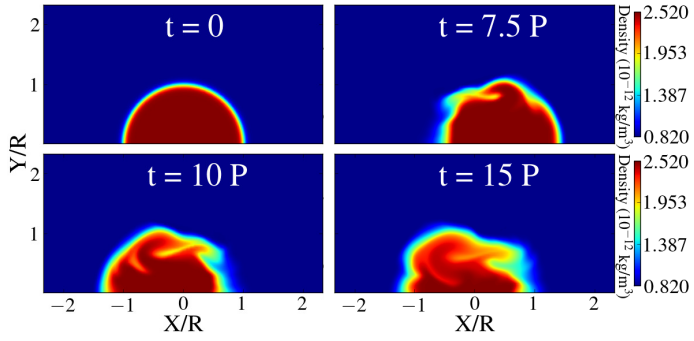

Figure 4.3: Same as Fig. 4.2, but for a driver with $v_0 = 0.8$ km s^{-1}.

In Fig. 4.5 and 4.6, we plot the average density, temperature, resistive heating rate (H_{res}) and the heating by shear viscosity (traced here by square z-vorticity, ω_z^2), as functions of distance from the centre of mass, at the apex and near the footpoint respectively. Initially, the values of H_{res} and ω_z^2 are zero, and remain small for the first few periods. At the apex, both the density and temperature spread across the cross section, as a result of the extended TWIKH rolls, effectively widening the loop boundary layer. Near the footpoint, suppression of the KHI results in less mixing, which is evident from the corresponding density and temperature profiles. The resistive heating rate peaks near the footpoint, in agreement with Karampelas et al. (2017). On the other hand, the viscous heating rate peaks near the loop. Radially, both of them are initially confined to the resonant layer, but later spread out over the entire loop cross section, as we can see in Fig. 4.7 for the ω_z^2 at the apex and the H_{res} at the footpoint, for

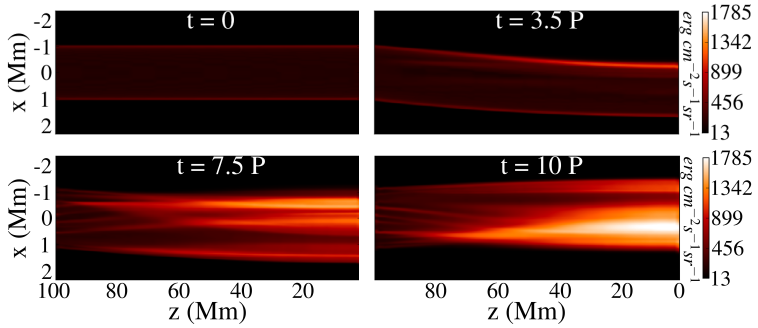

Figure 4.4: Forward modelling images of the integrated emission intensity (in erg $\mathrm{cm}^{-2}\mathrm{s}^{-1}\mathrm{sr}^{-1}$) of the tube for the 193.509 Å line. The observer is at a 0° LOS angle, perpendicular to the oscillatory motion. Half the loop length is modelled ($z = 0 - 100$ Mm). The driver peak velocity is $v_0 = 2$ km s^{-1}, and $P \simeq 254$ s is the driver period.

snapshots at $t = 7.5\,P$.

4.4 Discussion and conclusions

Looking at the loop cross section at the apex (Fig. 4.2), it is interesting to see the gradual deformation of the loop, as the simulation reaches its final stages. In the current model, the site of the highest deformation is located in the area near the loop apex, because the v_x, v_y velocity antinode and B_x, B_y magnetic field node appear there. Previous works have shown that TWIKH rolls create a wide turbulent layer both for impulsive (Magyar & Van Doorsselaere 2016) and driven (Karampelas et al. 2017) standing modes. Here our previous simulations were performed for an extended duration ($t_{max} = 10$ P). The extended TWIKH rolls result in a completely deformed loop cross section, where extensive mixing is taking place across the entire loop. Thus the loop cross section at the apex becomes fully deformed. Studying the results in Fig. 4.3 (and as is intuitively clear), we see that the driver amplitude plays an important role in the development of the KHI and the evolution of the loop cross section. However, we find that the loop cross section also evolves to a fully deformed state, even for the very small driver amplitude ($v_0 = 0.8$ km s^{-1}). Both setups are also showing similar amplitudes of the displacement, once the cross sections of the flux tubes become fully deformed from the KHI. Therefore, it is probably safe to assume that coronal loops have a deformed cross section, if they are driven by transverse footpoint motions for a sufficiently long time.

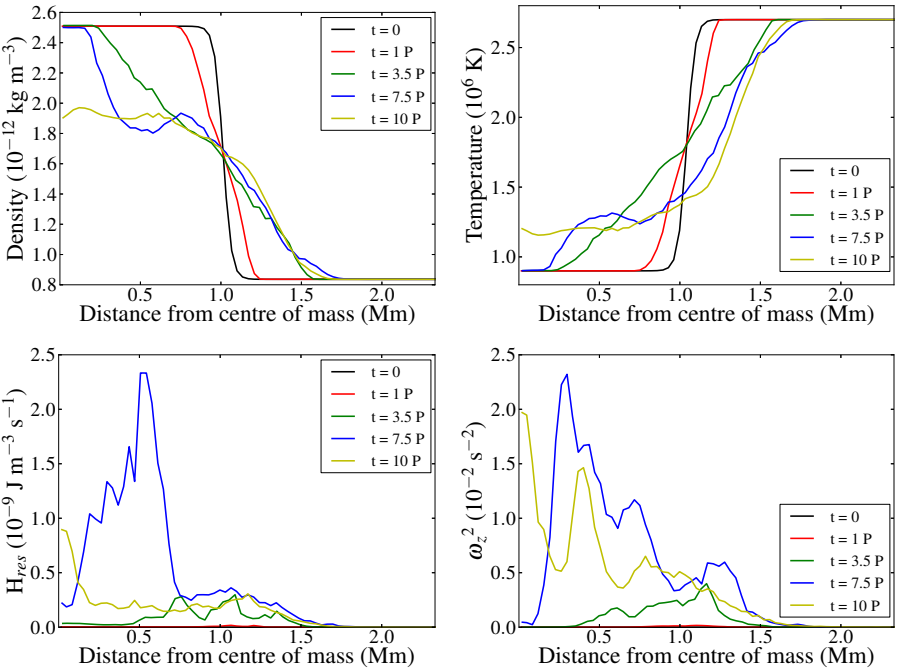

Figure 4.5: Profiles of the average density, temperature, resistive heating rate H_{res} and vorticity ω_z^2 as a function of the distance from the centre of mass, at the apex ($z = 0$). The driver peak velocity is $v_0 = 2$ km s^{-1}, and $P \simeq 254$ s is the driver period.

The turbulent nature of the cross section has a profound impact on the radial structure of the loop. As we see from the panels of Fig. 4.5, the density and temperature profiles near the apex seem to get smoothed over time, in these angle-averaged radial density and temperature profiles. This effect is most prominent between $z = 50$ Mm and the apex (0 Mm). Near the loop footpoint (Fig. 4.6), the smearing of density and temperature profiles is less, because the TWIKH rolls are absent there. Mass flows along the axis of the loop are present, and they are related to the ponderomotive force on loops performing standing oscillations (Terradas & Ofman 2004). However, the overall mass of the system remains constant over time, since the there is no constant mass flows through the boundaries.

The deformation of the loop cross section due to the KHI instability affects the spatial distribution of the resistive and viscous heating rate. Despite the smooth appearance of the density and temperature in Fig. 4.5, the damping of

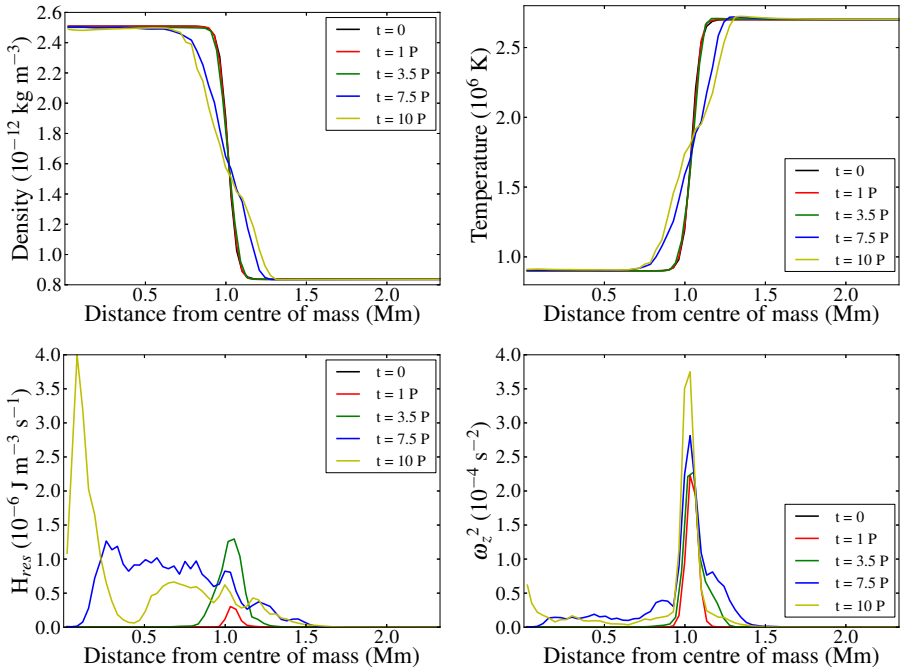

Figure 4.6: Same as Fig. 4.5, but the profiles are taken near the footpoint ($z = 99$ Mm).

the kink wave continues to take place. The resonant layer is now turbulently fragmented into many current sheets or shear layers in the velocity, because of the KHI eddies over the whole cross section. The resistive heating peaks near the footpoints, as we see in Fig. 4.6. H_{res}, which is dominated by the diffusion of the J_z current density (Karampelas et al. 2017), is initially concentrated in the resonant layer. Later, it spreads over the whole tube cross section (Fig. 4.7), even if the loop is not highly deformed near the footpoint. Instead, this is due to the deformed cross section near the loop top affecting the imprint of the current near the footpoint. Likewise, the viscous heating rate is spreading through the entire cross section because of the turbulent deformation (Fig. 4.7). However, in contrast to the resistive heating rate, it finds its maximum near the loop apex (Fig. 4.5).

In our current experiments, there is not enough energy input at the footpoint to balance the energy losses which are to be expected from the plasma (by e.g. optically thin radiation or heat conduction). However, in principle the plasma could be heated if a sufficient energy flux is provided by the driven

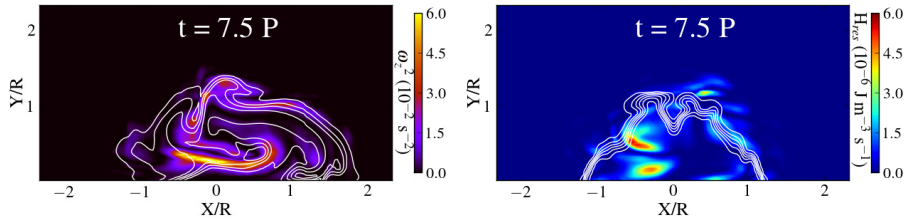

Figure 4.7: Snapshots of the vorticity ω_z^2 at the apex (top) and of the resistive heating rate H_{res} near the footpoint (bottom), for the driver with $v_0 = 2$ km s^{-1}. $P \simeq 254$ s is the driver period. The white lines on both panels represent the density contours at the corresponding heights, showing the circumference of the dense loop.

boundary. The key point of this study is that this heating (be it resistive or viscous) can take place in the entire cross section of the loop, because of its fully deformed nature. While it was earlier refuted by using drivers with a broad-band spectrum, the decade-old argument (Ofman et al. 1998; Cargill et al. 2016) that wave heating can only take place in specific layers in the loop is thus not even true for monoperiodic drivers.

Despite the fully deformed state of the loop cross section, the forward modelling of our simulation (Fig. 4.4) still maintains a loop-like appearance. The only qualitative changes compared to the forward model of a 'laminar' loop (i.e. a straight cylinder) is that (1) strand-like features are formed (as previously pointed out by Antolin et al. 2014), and (2) the overall intensity is increased and spread over a larger layer. The latter is because of the adiabatic expansion during the mixing of the interior and exterior plasma (as previously shown by Antolin et al. 2016; Karampelas et al. 2017). However, the coronal loop structure is clearly distinguishable from its surrounding plasma, and its oscillation remains visible at later times. Thus, the observational identity of a fully deformed loop remains intact, and should be detectable when studying relevant phenomena, such as the decayless loop oscillations from Anfinogentov et al. (2015).

The fact that heating by transverse waves occurs in the entire, deformed loop cross section, provides impetus to more detailed wave heating models, going beyond the qualitative arguments presented in this chapter. The introduction of a realistic atmosphere and thermal conduction in future setups, the inclusion of physical dissipation terms, such as anomalous resistivity, and the use of stronger drivers could provide a viable loop heated by transverse waves in its entirely deformed cross section, further addressing the issues brought up by Cargill et al. (2016).

Chapter 5

Wave heating in gravitationally stratified loops.

"How many of these are just horrible mistakes I made? I mean, maybe I'd stop making so many if I let myself learn from them."
Morty Smith (voice) (Justin Roiland)

Rick and Morty, Season 3: Morty's Mind Blowers

Abstract
In the current chapter, we map the sites of energy dissipation from transverse waves in coronal loops in the presence and absence of gravitational stratification. The effects of different dissipation coefficients such as resistivity and viscosity, as well as the loop physical characteristics are also considered in the context of wave heating. Using the PLUTO code, we performed 3D MHD simulations of kink waves in single, straight, density-enhanced coronal flux tubes of multiple temperatures. We see the creation of spatially expanded Kelvin-Helmholtz eddies along the loop, which deform the initial monolithic loop profile. For the case of driven oscillations, the Kelvin-Helmholtz instability develops despite physical dissipation, unless very high values of shear viscosity are used. Energy dissipation gets its highest values near the apex, but is present all along the loop. We obtain

an increased efficiency of wave heating once the kinetic energy saturates at the later stages of the simulation and a turbulent density profile has developed. The inclusion of gravity greatly alters the dynamic evolution of our systems and should not be ignored in future studies. Stronger physical dissipation leads to stronger wave heating in our set-ups. Finally, once the kinetic energy of the oscillating loop starts saturating, all the excess input energy turns into internal energy, resulting in more efficient wave heating.

This chapter is based on Karampelas et al. (2019a).

5.1 Introduction

One of the open questions regarding the nature of the solar atmosphere is explaining its radial temperature profile. The extreme ultraviolet (EUV) and thermal X-ray emission from the solar corona reveal plasma temperatures above 1 MK, while observations of active regions reveal temperatures of $\log T \geqslant 6.5$ for plasma confined into compact loops (Testa & Reale 2012). These findings guide the study of solar atmospheric heating towards areas of stronger, structured magnetic fields in the context of both the active and the quiet Sun.

Coronal heating models are usually classified into direct current (DC) and alternating current (AC) models. In direct current models like Ohmic dissipation of current sheets and nanoflares, heating is induced by magnetic field braiding in timescales much larger than the Alfvén crossing time along a coronal loop (Cargill & Klimchuk 2004; Klimchuk 2006; Chitta et al. 2018). On the other hand, alternating current models focus on mechanisms with dynamic timescales that are shorter than the Alfvén crossing time along a coronal loop and mainly consist of wave energy dissipation models (Hollweg 1981; Ofman et al. 1994a; Pagano & De Moortel 2017; Pagano et al. 2018) and Alfvén wave induced turbulence (van Ballegooijen et al. 2014, 2017; Magyar et al. 2017).

The increased interest in loop oscillations is also justified by the discovery of transverse magnetohydrodynamic (MHD) oscillations of loops (Aschwanden et al. 1999; Nakariakov et al. 1999). The physical characteristics of the loops allow them to dynamically connect different layers of the solar atmosphere, by acting as waveguides and transferring energy across those layers. The most well-studied loop model is the simple structure of a cylindrical flux tube; the theory of surface waves in Zajtsev & Stepanov (1975), Ryutov & Ryutova (1976), and Edwin & Roberts (1983) described the different modes expected in such a structure. Observations by the Coronal Multi-channel Polarimeter (CoMP), the Solar Dynamics Observatory (SDO), and Hinode spacecraft have

further sustained research interest in the environments where oscillating loops are found in abundance. A large number of studies have already proved the ubiquity of transverse perturbations along coronal loops, prominence threads and greater areas of the corona (e.g. Tomczyk et al. 2007; Okamoto et al. 2007; Tomczyk & McIntosh 2009; McIntosh et al. 2011), and the magnitude of the estimated energy carried by such waves is under strong debate (De Pontieu et al. 2007b; McIntosh et al. 2011; Goossens et al. 2013; Van Doorsselaere et al. 2014b; Thurgood et al. 2014; Morton et al. 2016).

The first step towards energy dissipation from waves in loop structures is the energy transfer to smaller scales, where it can be turned into internal energy of the plasma. The main mechanisms considered responsible for wave damping are resonant absorption (also known as mode coupling) for the case of standing modes (Ionson 1978; Sakurai et al. 1991; Goossens et al. 1992; Goossens et al. 2002; Ruderman & Roberts 2002; Arregui et al. 2005; Goossens et al. 2011; Pascoe et al. 2010; De Moortel et al. 2016; Yu et al. 2017). Both mechanisms use a resonance to transfer the energy of the global mode to local azimuthal Alfvén modes at the resonant layer, reducing the amplitude of the transverse oscillations. In the presence of a varying Alfvén speed profile transverse to the propagation direction, smaller scales are further created through phase mixing (Heyvaerts & Priest 1983; Soler & Terradas 2015). Once the smaller scales have developed, dissipation mechanisms such as resistivity or viscosity can lead to heating (Ofman et al. 1998; Beliën et al. 1999; Pagano & De Moortel 2017). A disadvantage of this approach, however, is the spatial confinement of the resonant layer. Cargill et al. (2016) showed that, unless broadband drivers (Ofman et al. 1998) or additional heating mechanisms are taken into account, this localized heating would not be capable of sustaining a fixed density gradient between the loop and the environment once radiative cooling was considered.

Another way to spread the resonant layer across a flux tube cross section, in the case of standing waves, is the development of the Kelvin-Helmholtz instability (KHI) from strong shear velocities generated by the azimuthal Alfvén waves (Heyvaerts & Priest 1983; Zaqarashvili et al. 2015). The KHI creates a turbulent layer at the loop edges, where resonant absorption and phase mixing can effectively transfer energy to smaller scales. Three-dimensional simulations of straight flux tubes confirmed the non-linear connection between resonant absorption, phase mixing, and KHI for driver generated azimuthal Alfvén waves (e.g. Uchimoto et al. 1991; Ofman et al. 1994c; Poedts & Goedbloed 1997; Poedts et al. 1997). More recent numerical studies (e.g. Terradas et al. 2008; Magyar & Van Doorsselaere 2016; Antolin et al. 2017; Howson et al. 2017a; Terradas et al. 2018; Antolin et al. 2018) have confirmed the development of transverse wave induced Kelvin-Helmholtz (TWIKH) rolls for standing kink waves in flux tubes in different environments, which lead to mixing between the

loop cross section and the surrounding plasma.

Studies of continuous footpoint driven standing waves in flux tubes (Karampelas et al. 2017; Karampelas & Van Doorsselaere 2018), inspired by the recently observed, decayless low-amplitude kink oscillations in coronal loops (Nisticò et al. 2013; Anfinogentov et al. 2015; Nakariakov et al. 2016), have focussed on the effects of KHI on coronal loop heating. The constant input of energy in these simulations causes the developed TWIKH rolls to expand across the loop cross section, leading its initial monolithic density profile into a turbulent state and fully deforming this profile in the process. This deformation spreads the resonant layer, where energy dissipation takes place across the loop in the presence of resistivity and viscosity. Its imprint on the magnetic field near the footpoint also causes the resitive heating rate there to spread gradually inside the loop, leading to energy dissipation and temperature increase. However, this heating is easily masked by the mixing between plasma of different temperatures.

In the current study, we expand upon our previous work, aiming to model low-amplitude, decayless kink waves in active region coronal loops that are driven by footpoint motions. We incorporate gravity into our models to study its effects on the loop dynamics alongside the potential effects on wave heating. Physical resistivity and shear viscosity have been introduced alongside gravity, allowing us to study their effects on the development of the TWIKH rolls for driven oscillations (Howson et al. 2017b, for impulsively oscillating loops without gravity) and on the wave heating process. Finally the energy evolution of different models is considered, giving us insight into the underlying mechanics of wave heating.

5.2 Numerical model

5.2.1 Equilibrium

For our $3D$ simulations, we use straight, density-enhanced magnetic flux tubes in a low-β coronal environment, similar to that in Karampelas et al. (2017). We mainly focus on gravitationally stratified, active region coronal loops in ideal, resistive, and viscous MHD, while also including two models of non-stratified loops in ideal MHD used as reference. Each loop has a full length (L) of 200 Mm and an initial radius (R) of 1 Mm, which is constant with height. In the following analysis, we denote the basic values of our physical parameters with the index i (e) for internal (external) values, with respect to our tube.

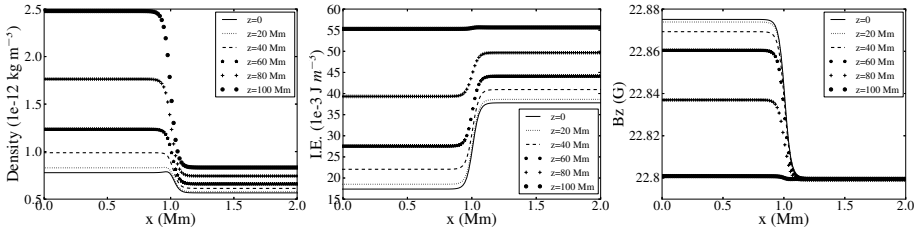

Figure 5.1: Radial profile of density (*left*), internal energy (*middle*), and B_z magnetic field (*right*) for the gravitationally stratified models at different heights after the relaxation period. The profiles are considered before initiating the driver. The apex is located at $z = 0$ and the footpoint at $z = 100$ Mm. $x = 0$ is the centre of the loop at $t = 0$.

The radial density profile, for all models is given by the relation

$$\rho(x, y) = \rho_e + (\rho_i - \rho_e)\zeta(x, y), \tag{5.1}$$

$$\zeta(x, y) = \frac{1}{2}(1 - \tanh((\sqrt{x^2 + y^2}/R - 1)\, b)), \tag{5.2}$$

where ρ_e is the external density and ρ_i the internal or loop density. For the gravitationally stratified loops, we define the internal and external density at the footpoint as ρ_i and ρ_e, with $\rho_e = 10^9 \mu\, m_p$ cm^{-3} $= 0.836 \times 10^{-12}$ kg m^{-3} ($\mu = 0.5$ and m_p is the proton mass). For the non-stratified models, the density radial profile is constant with height. By x and y we denote the coordinates in the plane perpendicular to the loop axis, z along its axis and b sets the width of the boundary layer. We consider $b = 20$, which gives us an inhomogeneous layer of width $\ell \approx 0.3R$. We choose a density ratio of $\rho_i/\rho_e = 3$ for all models at the footpoint, within the range of estimated ratios (Aschwanden et al. 2003), which is suitable for fast transfer of energy from transverse to azimuthal motions, through resonant absorption. For all models studied, we set the initial temperature to be constant with height. Radial dependence of temperature depends on the different cases considered. Finally, we consider an initial uniform magnetic field and parallel to the flux tube axis, along the z-axis ($B_z = 22.8$ G).

In the cases where gravity is included, it varies sinusoidally along the flux tube, taking a zero value at the loop apex ($z = 0$) and maximum absolute value at the footpoints ($z = \pm 100$ Mm). We use this variation per height to model the effects of the curvature along the loop axis, while retaining a straight flux tube. Thus, we have stratification of pressure and temperature along the loop

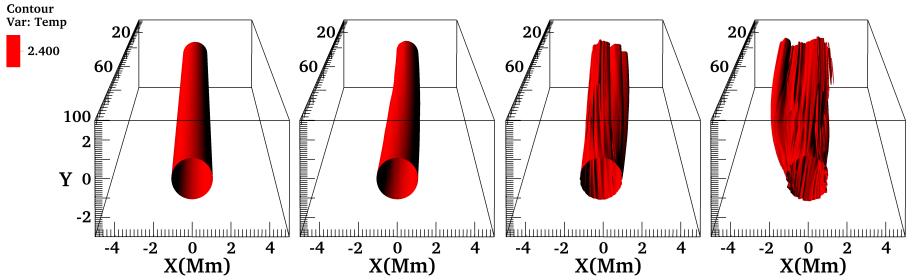

Figure 5.2: Three-dimensional temperature contour plot, measured in 10^6 K, for a gravitationally stratified cold loop in a warm corona (model ColdI). Moving from the left to right: t = 0, 2.5 P, 4.75 P, and 10 P, where $P = 171$ s is the period of the driver. An animation of these figures, showing the oscillation for the model in ideal MHD, is available in the online version of Karampelas et al. (2019a, Movie 1).

according to the hydrostatic equilibrium,

$$\frac{\partial p_{i,e}}{\partial z} = -g\,\rho_{i,e}\,\sin(\frac{\pi z}{L}). \tag{5.3}$$

As a consequence of gravitational stratification, there is a pressure imbalance at the loop boundary, leading to a jump in total pressure. This imbalance is countered by the restructuring of a stratified magnetic field inside the loop, which causes a weak standing oscillation, with velocities of only a small fraction of the amplitude of our driver. By letting our system relax for a period, it reaches a quasi-equilibrium state (Fig. 5.1) and the aforementioned perturbation does not affect the global dynamics of our system. After the relaxation, the magnetic field shows a slight increase towards the apex inside the loop due to the chosen density and temperature configuration. During the relaxation of the systems, temperature, pressure, and density do not deviate significantly from their initial state.

The different cases considered in the current work are as follows:

1. A model of a loop in hydrostatic equilibrium between itself and the background plasma. No gravity is included. We consider a uniform temperature $T_i = T_e = 10^6$ K, and use MHD with an estimated (numerical) magnetic Reynolds number $R_m = 10^6$ and estimated (numerical) Reynolds number $R_e = 10^6$. This model is called "UniT". Total pressure is kept constant along and across the flux tube by changing the magnetic field along the radial direction from $B_{zi} = 22.8$ G for the internal to $B_{ze} = 22.95$ G for the external magnetic field.

2. A loop model without gravity ("ColdIngr") in hydrostatic equilibrium between itself and the background plasma. We consider a temperature ratio of $T_i/T_e = 1/3$ with $T_i = 9 \times 10^5$ K, and estimated numerical dissipation coefficients $R_m = 10^6$ and $R_e = 10^6$.

3. A gravitationally stratified loop ("ColdI") in hydrostatic equilibrium between itself and the background plasma. We consider temperature ratio of $T_i/T_e = 1/3$ with $T_i = 9 \times 10^5$ K, and estimated numerical dissipation coefficients $R_m = 10^6$ and $R_e = 10^6$.

4. Model "ColdR". Same as model ColdI but with the introduction of additional explicit resistivity, leading to $R_m = 10^4$.

5. Model "ColdV". Same as model ColdI but with additional explicit shear viscosity, leading to $R_e = 10^4$.

6. Model "ColdV2". Same as model ColdV but for a lower Reynolds number ($R_e = 10^2$).

All of the gravitationally stratified models start from the same initial state (after the relaxation) shown in Fig. 5.1 before applying the driver and physical dissipation.

A detailed overview of the physical parameters for each model a presented in Table 5.1. The different temperature profiles are useful in identifying and studying the underlying heating mechanisms in the solar corona. Model UniT is a very similar model to the *Driven-equalT* model from Karampelas et al. (2017), but for a stronger driver. We simulated this system to see the effects of numerical diffusion on energy dissipation for our current code and resolution in the same way as in our previous study. Models ColdI, ColdR, ColdV, and ColdV2 are the extensions of the *Driven-diffT* model from Karampelas et al. (2017), when gravity and physical dissipation are introduced. ColdIngr is based on the same model, but for different values of density, which is useful for directly comparing with the gravitationally stratified models, as is demonstrated later. Through these models we want to study the effects of gravity, resistivity, and viscosity on cold flux tubes, for example like the loops in thermal non-equilibrium (Froment et al. 2015, 2017) considered later during their cooling phase.

5.2.2 Grid

The 3D ideal MHD problem is solved using the PLUTO code (Mignone et al. 2012, 2018), where the extended GLM method from Dedner et al. (2002) is employed to keep the solenoidal constraint on the magnetic field. We use

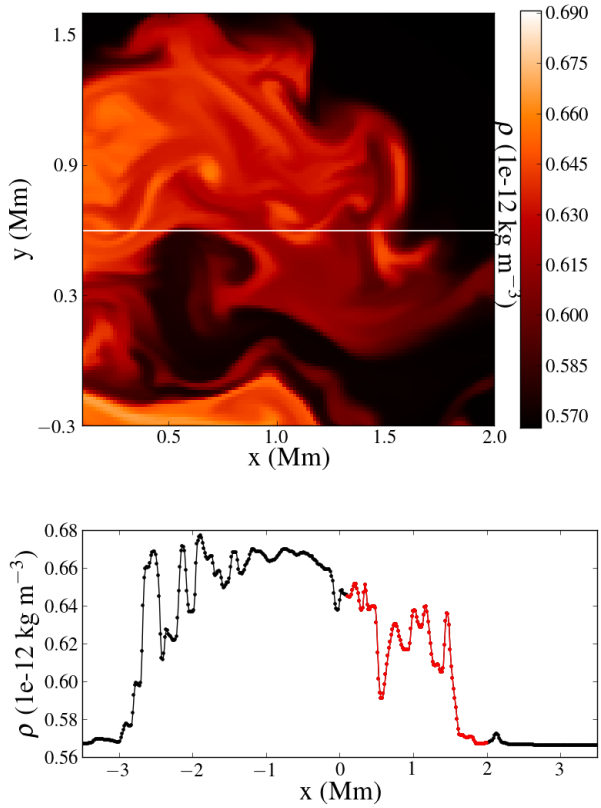

Figure 5.3: *Top panel*: Part of the total density cross section for model ColdI, at the apex. We focus on the area with $-0.3 \leq y$ (Mm) ≤ 1.6 and $0.1 \leq x$ (Mm) ≤ 2.0 to highlight the resolution of smaller scale structures on the $x-y$ plane. *Bottom panel*: The density structure at $y = 0.6$ Mm, along the white line of the top image. The dots represent the grid points along the white line. The red line highlights the part visible in the image above. The plot shows time t $= 10\,P$; $P = 171$ s indicates the period of the driver.

Table 5.1: Overview of the physical parameters for the different models in our simulations. The index i (e) denote internal (external) values, while the index f represent the footpoint values. Density is normalized by $\rho_u = 10^{-12}$ kg m^{-3}.

Name	Gravity	Period	T_i/T_e	T_i	ρ_{if}/ρ_u	β_f	R_e	R_m
UniT	no	256	1	10^6	2.509	0.02	10^6	10^6
ColdIngr	no	171	1/3	9×10^5	1.129	0.08	10^6	10^6
ColdI	yes	171	1/3	9×10^5	2.509	0.018	10^6	10^6
ColdR	yes	171	1/3	9×10^5	2.509	0.018	10^6	10^4
ColdV	yes	171	1/3	9×10^5	2.509	0.018	10^4	10^6
ColdV2	yes	171	1/3	9×10^5	2.509	0.018	10^2	10^6

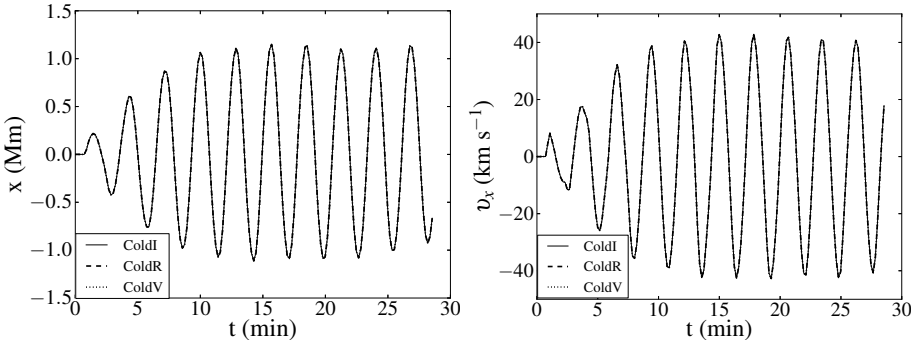

Figure 5.4: Centre of mass displacement (*left panel*) and centre of mass v_x velocity (*right panel*) at the apex for our different models.

the finite volume piecewise parabolic method (PPM) with a second order spatial global accuracy, and the second order characteristic tracing method for calculating the timestep. For the resistivity and shear viscosity, an explicit method for recalculating the timestep is used.

The domain dimensions for models ColdIngr, ColdI, ColdR, ColdV, and ColdV2 are $(x, y, z) = (10, 6, 100)$ Mm. We use a uniform grid with a resolution of $640 \times 384 \times 64$, which translates into cell dimensions of $15.625 \times 15.625 \times 1562.5$ km for all models. For the UniT model we use a domain of $(x, y, z) = (10, 3, 100)$ Mm, which have the same cell dimensions as in the rest of our models. The resolution is higher in the $x-y$ plane, to better resolve the small-scale structures that appear in the loop cross section, as we can see in Fig. 5.3. The resolution on the z-axis can sufficiently model the density stratification, since the lack of radiation or thermal conduction reduces the need for a finer grid along the tube

axis. The footpoint of the loop is located at $z = 100$ Mm and the apex at $z = 0$. In all of our models, we have the inevitable numerical dissipation effects, which lead to an effective resistivity and viscosity many orders of magnitude larger than those expected in the solar corona. Through a parameter study of changing the values of physical resistivity and viscosity, we estimated the effective Reynolds and magnetic Reynolds number to be $R_e = 10^6$ and $R_m = 10^6$. These are the values for the ideal MHD cases in our simulations.

5.2.3 Driver

Our tubes are driven from the footpoint ($z = 100$ Mm), using a continuous, monoperiodic 'dipole-like' driver (Karampelas et al. 2017), inspired by that used by Pascoe et al. (2010). The period of the driver is $P \simeq 2L/c_k$, coinciding with the corresponding fundamental eigenfrequency for each model (Edwin & Roberts 1983; Andries et al. 2005). The values of the periods for each each model are listed in Table 5.1.

The driver velocity is uniform inside the loop and time varying,

$$\{v_x, v_y\} = \{v(t), 0\} = \{v_0 \cos(\frac{2\pi t}{P}), 0\}, \tag{5.4}$$

where $v_0 = 4$ km s^{-1} is the peak velocity amplitude, close to the observed photospheric motions. Outside the loop, the velocity follows the relation

$$\{v_x, v_y\} = v(t)R^2\{\frac{(x-\alpha(t))^2 - y^2}{((x-\alpha(t))^2 + y^2)^2}, \frac{2(x-\alpha(t))y}{((x-\alpha(t))^2 + y^2)^2}\}, \tag{5.5}$$

where $\alpha(t) = v_0\,(0.5\,P/\pi)\,\sin(2\pi t/P)$ is a function that recentres the driver, following the movement of the footpoint. To avoid any numerical instabilities due to jumps in the velocity, a transition region following the density profile exists between the two areas. By moving the driver with the footpoint along the x direction, we keep the base of the loop inside the central region of uniform velocity.

5.2.4 Boundary conditions

We keep the velocity component parallel to the z-axis (v_z) antisymmetric at the bottom boundary ($z = 100$ Mm) to prevent flows of mass through it. We also extrapolate the values for density and pressure, using the equations for hydrostatic equilibrium, while we use a zero normal gradient condition for the

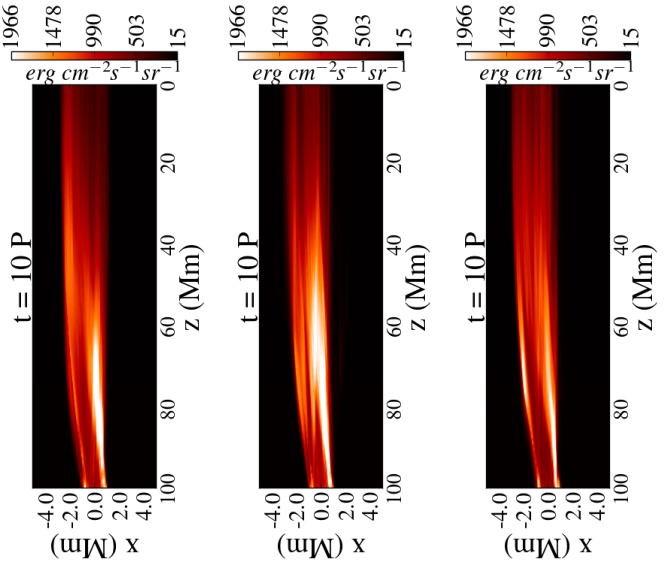

Figure 5.5: Forward modelling images of the integrated emission intensity (in erg cm^{-2}s^{-1}sr^{-1}) of the cold tubes (the models ColdI, ColdR, and ColdV) for the 195.12 Å line. The observer is at a 0° LOS angle, perpendicular to the oscillatory motion. Half the loop length is modelled ($z = 0 - 100$ Mm). From left to right, the ideal case at t = $10\,P$, resisitive case at t = $10\,P$, and viscous case at t = $10\,P$ are shown. The driver period is $P \simeq 171$ s. A movie with the forward modelling for model ColdI is available on-line Karampelas et al. (2019a, Movie 2).

magnetic field,

$$B_i(z = 100) = \frac{1}{11}\left(2B_i(100 + 3dz) - 9B_i(100 + 2dz) + 18B_i(100 + dz)\right), \tag{5.6}$$

to extrapolate the values of each magnetic field component through the bottom boundary. To calculate it, we used a forward finite difference formula for the derivative, on a four-point stencil (corresponding to three ghost cells), and set the gradient to be zero. Finally, the v_x and v_y velocities are defined by the driver. For the UniT and ColdIngr models, where no gravity is considered, we simply use Neumann-type, zero-gradient conditions for the density, pressure, and magnetic field. Studying the fundamental standing kink mode for an oscillating flux tube allows us to take advantage of the inherent symmetries of this mode, as well as the symmetric nature of our driver. In the top boundary ($z = 0$), we kept v_z, B_x, and B_y antisymmetric, in the $x - y$ plane at the apex, while all

the other quantities are symmetric. Thus, only half the loop is simulated along the loop axis.

For the UniT model we also took into account the symmetric nature of the kink mode and our driver along the y-axis. The v_y and B_y are antisymmetric in the $x-z$ plane, while the other quantities are symmetric. Therefore, our computational time is reduced fourfold in total for this model, following our previous work (Karampelas et al. 2017; Karampelas & Van Doorsselaere 2018). At the three lateral boundaries, we apply outflow (Neumann-type, zero-gradient condition) conditions, which allow waves to leave the domain.

For models ColdIngr, ColdI, ColdR, ColdV, and ColdV2, we do not employ the symmetry at the $x-y$ plane. This way, through the inevitable development of numerically induced asymmetries, we allow the loop to evolve in a non-symmetric environment, as we would generally expect in the solar corona. All the side boundaries in these models are set to outflow (Neumann-type, zero-gradient) conditions for all variables, which allow waves to leave the domain.

To minimize their effect on the dynamics of our loops, we placed the x side boundaries (along the direction of the oscillation) at a safe distance from the loop (5 R in x). On the y direction (perpendicular to the oscillation), we placed the boundaries at 3 R from the centre of the loop in order for them to not affect the development of our oscillations.

5.2.5 Forward modelling

We use the FoMo code (Van Doorsselaere et al. 2016) to render spectroscopic images of our simulation data on the different models. We present snapshots of the emission intensities for different lines. In all images, we consider a line-of-sight plane perpendicular to the loop axis and we set the LOS angle perpendicular to the oscillation direction equal to 0°. By choosing to study the emission intensity for the Fe XII 195.12 Å line, we focus on the temperatures found predominately in the turbulent layer developing because of the KHI (Antolin et al. 2016, 2017).

5.3 Results

In the following analysis, we define the flux tube through a density threshold (normalized by $\rho_u = 10^{-12}$ kg m^{-3}) as follows:

$$\rho_{tube} \geq 0.359\,\frac{\rho_i}{\rho_u}\,f(x,y,z) = 0.9\,\exp\left(\frac{-g_0\,L}{R_{\rm spf}\,\pi}\,\frac{\cos\left(\pi z/L\right)}{T(x,y)}\right), \qquad (5.7)$$

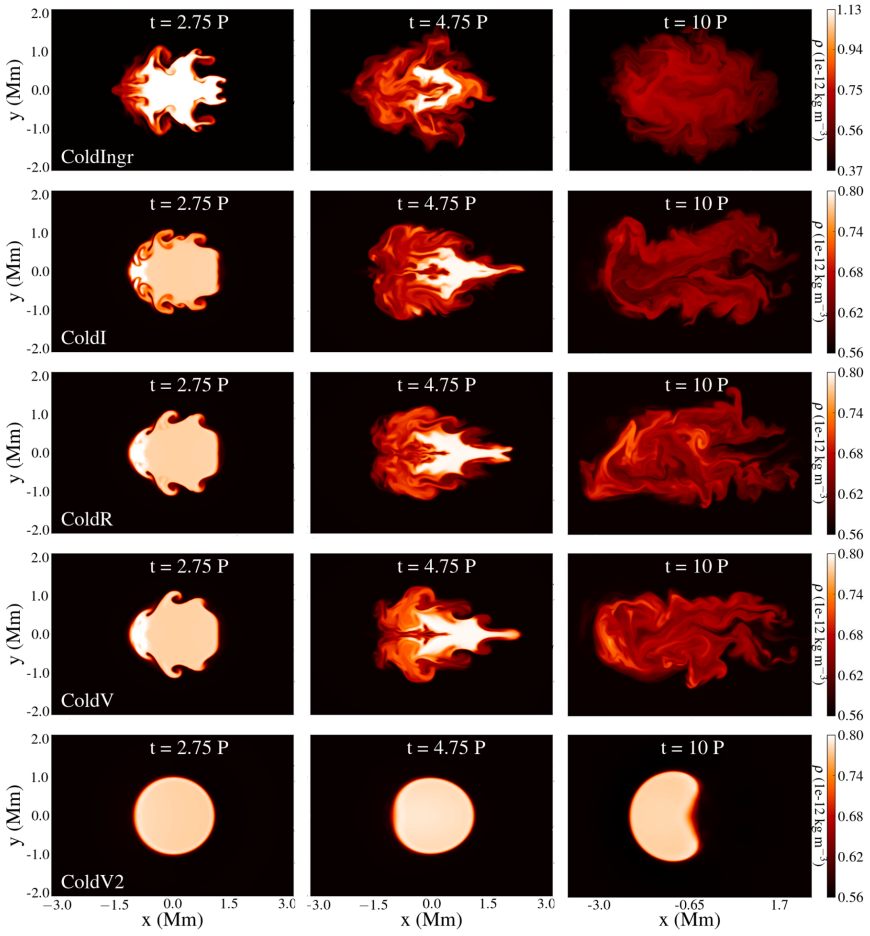

Figure 5.6: Contour plots of the density in the cross section at the apex for five different set-ups of cold loops at three different times. From top to bottom: models ColdIngr, ColdI, ColdR, ColdV and ColdV2. Panels are recentred to keep a clear view of the entire cross section. A different colourscale is chosen for the ColdIngr case, better adjusted to the density profile. All panels have the same dimensions of 6.3 Mm in the x direction and 4.2 Mm in the y direction. The period of the driver is $P = 171$ s. Animations of these plots for the ColdI, ColdR and ColdV are available on-line in Karampelas et al. (2019a, Movies 3, 4 and 5).

where $g_0 = 274$ m s^{-2} is the solar gravitation in the surface of the sun, $R_{\rm spf}$ is the specific gas constant, and $T(x, y)$ is the initial temperature profile for each model, which is independent of height in our set-ups. For models 1 and 2 we have $\rho_{tube}(x, y) \geq 0.359\rho_i/\rho_u$.

Regarding the models of cold loops embedded in a hot environment, our choices of the density profiles and magnetic field ensure that these five models have the same frequency of the fundamental standing kink mode, as we see in Table 5.1. These models all have the same optimal driver frequency, almost the same initial magnetic field, and the exact same driver. As a result, the only differences in the input energy from the driver are due to the different dynamical evolution of the systems. This difference of the input energy eventually affects the evolution of wave dissipation and the development of heating. Therefore, most of the differences are attributed to the presence or absence of gravity for the ideal MHD, and in the different values of R_m and R_e for the gravitationally stratified cases.

5.3.1 Loop dynamics and evolution

We drive our loops for a total of ten periods. As in Karampelas et al. (2017), the first waves to reach the apex ($z = 0$) are the azimuthal Alfvén waves at the boundary layer of our tube, thanks to their higher propagation speed, followed by the propagating kink waves. The propagating waves superpose with the counter propagating waves from the other footpoint (due to the symmetry at the apex), forming a standing wave. By choosing driving frequencies equal to the analytically predicted frequencies for the fundamental kink mode (Edwin & Roberts 1983; Andries et al. 2005), we forced our loops to perform an oscillation resembling the fundamental standing mode for the kink wave. An animation of the ColdI model is available in the electronic version of Karampelas et al. (2019a), for Fig. 5.2, showing the evolution of that oscillation. We note that due to the finite speed of the waves originated at the footpoint, the apex starts oscillating later than the footpoint, where the driver is located. This is shown in Fig. 5.4, where the oscillation at the apex starts later than the start of the driver (at $t = 0$). This leads to a phase difference between oscillation at the footpoint and the apex, similar to that found for the driven models of our previous studies (Karampelas et al. 2017; Karampelas & Van Doorsselaere 2018).

As we see in Fig. 5.4, the centre of mass at the apex shows a maximum displacement of ≈ 1 Mm from the equilibrium position at $t = 0$. This is larger than the $\approx 0.1 - 0.3$ Mm oscillation amplitudes observed for decayless transverse oscillations in coronal loops (Nisticò et al. 2013; Anfinogentov et al. 2015; Nakariakov et al. 2016), and is caused by the strength of the driver used

in the current set-up. We note that the v_x velocity at the location of the centre of mass are $\approx 3.3\%$ of the initial internal Alfvén velocity.

As is expected from theory (Heyvaerts & Priest 1983; Zaqarashvili et al. 2015) and simulations (Terradas et al. 2008; Antolin et al. 2017), the location of the antinode of the x-velocity (here the apex) is Kelvin-Helmholtz unstable. We already know from Karampelas & Van Doorsselaere (2018) that the KHI for driven oscillations leads to the development of spatially extended eddies, the TWIKH rolls. Because of the frozen-in condition, the out of phase movement of the TWIKH rolls create elongated strand-like features along the flux tube, which we see in Fig. 5.2. The same structures are visible in Fig. 5.5, where we present snapshots of the emission intensity for the Fe XII 195.12 Å line at the end of our simulation, for models ColdI, ColdR, and ColdV. This spectral line was chosen because it is better suited to detect the hotter plasma at the loop edges in our set-up (Antolin et al. 2017). The resulting images are very similar to the non-stratified case (Karampelas & Van Doorsselaere 2018), showing that the introduction of gravity does not affect previous results on forward modelling of oscillating loops (Antolin et al. 2016, 2017). Furthermore, the similarity of the results between the ideal, resistive, and viscous MHD models can potentially hinder the observational distinction between the dissipative effects in coronal loops should one focus only on studying the dynamical evolution of these systems.

In Fig. 5.6 we show cross sections at the apex, at multiple oscillation times for models ColdIngr, ColdI, ColdR, ColdV, and ColdV2. For $R_e \geqslant 10^4$ and $R_m \geqslant 10^4$ the presence of higher dissipation such as resistivity and viscosity delays the emergence of the KHI compared to the ColdI model, in agreement with Howson et al. (2017b). However, the instability is fully developed for models ColdI, ColdR and ColdV within the first three driving periods. After almost five periods, the TWIKH rolls have already expanded across the loop cross section, deforming the initial density profile. By the end of the simulation, the loop surface area basically doubles for all three models at the apex, and the TWIKH rolls turn the initial monolithic density profile into a turbulent density profile. This evolution of the cross section is also obtained in most of the other models considered for this study, and is responsible for some of the results regarding the temperature evolution in our models. By simulating the entire loop cross section, we get numerically induced asymmetries in the development of KHI. These become more prominent in the second half of the simulations, creating an non-symmetric turbulent density profile, closer to what would be generally expected in the solar corona. Movies 3, 4, and 5 of Fig. 5.6 show the evolution of the loop cross section for the entirety of the simulation.

The only exception to the aforementioned cases is model ColdV2 ($R_e = 10^2$), where no TWIKH rolls are developed. The high value of the shear viscosity in

that model leads to the complete suppression of the KHI for the duration of our simulation. A similar effect was noted before in Howson et al. (2017b) in impulsively oscillating coronal loops for combined high values of resistivity and viscosity ($R_e = 10^4$ and $R_m = 10^4$). The higher values of dissipation required to suppress the KHI in our work are due to the continuous driving of our loops.

5.3.2 Temperature evolution in cold loops

In Karampelas et al. (2017), we proved that (numerical) resistivity increases the temperature of a non-stratified loop, with uniform initial temperature (Driven-equalT model), near the footpoint. In order to validate our previous results and study the effects of numerical dissipation in the current code to our results, we simulated a similar set-up for an increased resolution (UniT model). In Fig. 5.7, we examine the temperature profiles along the z-axis over time for this model and we plot the average temperature for the flux tube cross section (for $\rho \geq 0.9 \times 10^{-12}$ kg m^{-3}). We observe a gradual increase of the average temperature over time the closer we get to the footpoint and apex. The temperature increase is comparable in both regions and the highest values are obtained near the footpoint, while the area at mid-length of the loop experiences a negligible temperature increase.

At the apex, the higher velocity and the developed KHI leads to stronger viscous heating. Resistive heating is not expected to be as pronounced there because of the lack of strong currents caused by the nature of the fundamental standing kink mode. Ohmic dissipation, however, is stronger near the footpoint, where the average square current densities (dominated by the J_z^2) are at their strongest (Van Doorsselaere et al. 2007). Similar temperature profiles were obtained in Karampelas et al. (2017), but the temperature increase at the apex was not as pronounced. The differences between the present and past results are caused partly by the stronger driver employed and partly by the different numerical dissipation in each code. However, the temperature increases at the apex is expected from our previous analysis, despite the apparent contradiction with the older results. The temperature increase at the footpoint is explained through the higher values of the resistive heating rate there (Karampelas & Van Doorsselaere 2018). The area between the apex and the footpoint is not heated to a similar extent, because neither the currents are continuously as strong as near the footpoint, nor are the velocities and the z-vorticity as high as at the apex (see also Karampelas et al. 2017; Karampelas & Van Doorsselaere 2018).

Considering again our models of gravitationally stratified cold loops embedded in a hot corona, we try to see where the energy dissipation takes place and how this affects the temperature distribution. In Fig. 5.8 the cross sections at the

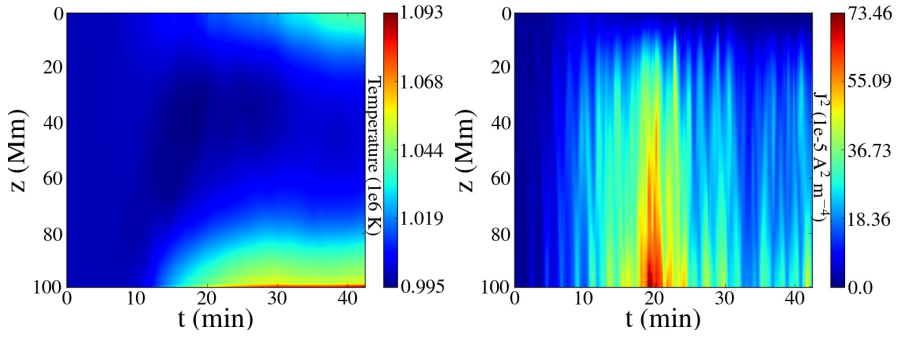

Figure 5.7: *Left panel*: Average temperature of the flux tube for $\rho \geq 0.9 \times 10^{-12}$ kg m^{-3} along the z-axis, for a non-stratified loop with uniform temperature (model 1). *Right panel*: Average square current densities (J^2) of the flux tube for $\rho \geq 0.9\, f(x, y, z)$ for the same model. The apex is located at $z = 0$.

apex of models ColdI, ColdR, and ColdV are shown for density, internal energy density, and temperature. As we see in the contours for internal energy density, the highest values lay on the interface between the expanded TWIKH rolls and the environment, while the internal part of the loop also shows increased values from those derived from the initial conditions (see Fig. 5.1). The highest values are found in the ColdV model, followed by the ColdR model, and finally by ColdI. The same can also be seen in the contours for the temperature and the ColdV case shows the highest values of temperature at the locations of the highest internal energy increase. Because of delayed mixing the viscous set-up also has some of the lowest temperatures in internal areas of the loop when compared to the other two cases. These profiles guide us into treating the obtained temperature increase of $\sim 4.7 \times 10^4$ K mainly as the result of dissipation, rather than the adiabatic temperature fluctuation that was found for loops of uniform temperature (Antolin et al. 2017; Karampelas et al. 2017).

In order to find the location of energy dissipation for models ColdI, ColdR, and ColdV, we plot in Fig. 5.9 the temperature profiles along the z-axis, over time, for the aforementioned models. In the initial stages of the simulation, we see a small temperature increase propagating from the footpoint towards the apex. These paths are attributed to slow waves initiated by the driver, which travel along the loop axis. These propagating slow waves superpose with the counterpropagating ones coming from the other footpoint. Similar counterpropagating slow waves in coronal loops can also be caused by reflections at the loop footpoints, as proven by the existence of standing slow waves in loops (e.g. Wang et al. 2003b,a). Once the KHI manifests, the mixing between the colder loop and the hot corona drops the average temperature of our domain.

This drop is more prominent at the quarter length of the flux tube, where both resistive and viscous heating are expected to have a lesser effect than at the footpoint and apex, respectively. Energy dissipation in that area is not strong enough to counter the apparent temperature drop due to the mixing, which becomes stronger at later stages of the simulation. However, a temperature increase is obtained near the footpoint and apex, as the simulations reach their final stages. This temperature increase becomes even stronger for the ColdR model, reaching its maximum values in the ColdV set-up. As we can observe, all three models show their strongest heating near the footpoint and minimum differences take place for the values of resistivity and viscosity.

Focussing on the ideal MHD case, we see that the internal energy density is increasing all along the flux tube, the highest values are found near the apex, and gradually lower values are found as we travel towards the loop footpoints. Considering the initial gradient of internal energy, we would intuitively expect an apparent drop in the average internal energy from the mixing of the different regions. This, however, is not observed. Instead, a constant increase of the internal energy density along the loop is obtained over time. This increase is a combination of resistive and viscous dissipation due to numerical dissipation, as we have already seen in the UniT model. The highest values near the apex seem to contradict the results of Van Doorsselaere et al. (2007), where it was proved that resistive heating should be the strongest for the fundamental standing mode of transverse oscillations. However, the higher values of temperature near the footpoint are still in agreement with that work. Looking at the flux tube surface area variation over time for model ColdI, we see that the loop is expanding. The highest values of the expansion are found near the apex where the cross-sectional surface area doubles in size as a consequence of the TWIKH rolls. Therefore, we can conclude that this temperature increase is not an apparent phenomenon but the result of wave heating.

In our past study of a cold loop inside a hotter corona without gravity (Karampelas et al. 2017), the mixing effects were effectively masking the results of energy dissipation in that set-up and the average temperature of our domain drops as a result of the cold loops expansion. In the present study, we reproduce the same results for the ColdIngr model, which are shown in Fig. 5.10. The square current density again shows higher values near the footpoint, and an increase of the internal energy is again seen along the loop axis. The heating due to the driver generated propagating slow waves that were found in the stratified case are not prominent in this set-up, which produces only very slight changes in the initial state of the simulations. The temperature shows a slight increase near the footpoint from ohmic dissipation due to numerical dissipation. However, the average temperature shows an apparent drop as we move higher up the loop as a consequence of TWIKH rolls developing in our domain. From

our current results, we see that the introduction of gravity leads to a more complex evolution of the average temperature.

In the gravitationally stratified models of ColdI, ColdR, and ColdV, we see a fluctuation of internal energy near the footpoint. The same fluctuation is clearer in the ColdIngr model, where we also have signs of a low frequency periodic fluctuation of the internal energy at the apex. This periodic fluctuation at the apex was also found in Magyar & Van Doorsselaere (2016) for impulsive standing oscillations in coronal loops, and is associated with the ponderomotive force on loops performing standing oscillations (Terradas & Ofman 2004). This perturbation is comparable to the effects of phase mixing the ColdIngr model. However, its effects are quickly negated by wave heating in the gravitationally stratified cases, while the overall dynamics seem to remain unaffected.

Looking again at models ColdR and ColdV (Fig. 5.9), we see that the highest internal energy is achieved by the viscous case, and both models show stronger heating than the ideal case. The spatial and temporal profile of the internal energy is still the same as in ideal MHD, and there are very small differences between the three models for the values of resistivity and viscosity that we used in this work. These differences are the result of the dissipation parameters on the dynamical evolution of the oscillating loops. The higher temperatures at the apex for the viscous case are what we expected from our past work. Near the footpoint, we would expect the resistive case to lead to the highest temperature increase, since the square current densities (dominated by J_z^2) have their highest values there for all three models. The viscous case also shows higher average temperatures there because of the shrinking of the tube cross section, as shown in the zt profile for the tube surface area of the ColdV model. This shrinking of the cross section of the cold loop increases the contribution of the hot corona in the calculation of the average temperature. This is combined with the resistive heating due to numerical dissipation, resulting in the apparent effect of higher average temperature than in the ideal MHD model.

Another interesting result that we obtain for models ColdR and ColdV are the evolution of the currents. As mentioned before, the J^2 has the highest values near the footpoint ($z = 100$ Mm) for all three models because of the strong J_z currents there. Both the resistive and viscous case show on average a reduced amount of currents, and there are some temporary high values higher up the loop. The spikes in current densities and the reduced amount of ambient low current densities, unlike the ideal case, is similar in the dynamical evolution of these systems. This similarity leads to the conclusion that when we have comparable values for the Reynolds and magnetic Reynolds number in a system, increased resistivity can act as a form of turbulent viscosity and viscosity can disrupt the development of smaller scales and currents comparable to a form of anomalous resistivity.

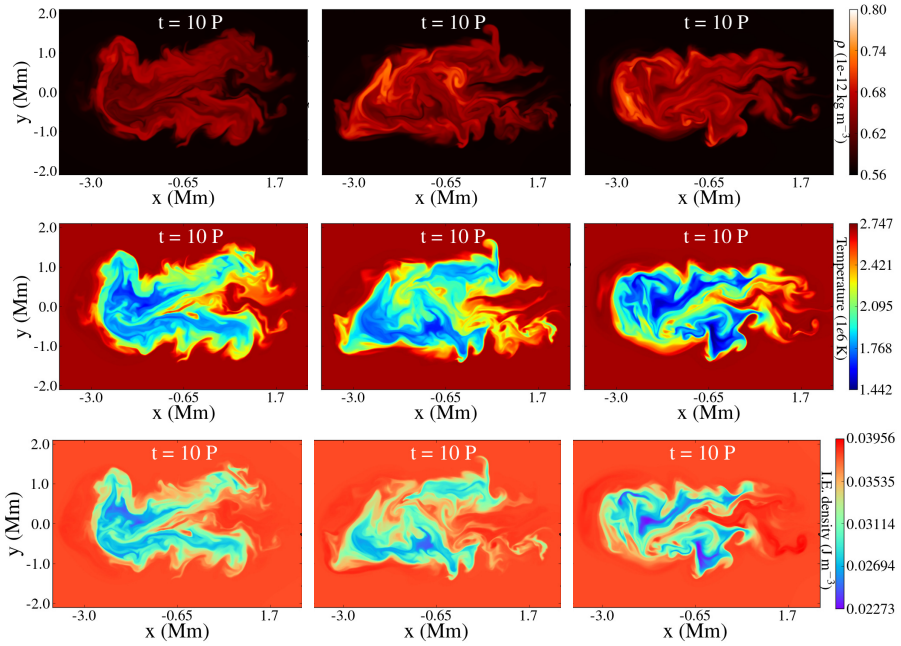

Figure 5.8: Contour plots of density (*top*), temperature (*middle*) and internal energy (*bottom*) at the apex for $-2.1 \leq y$ (Mm) ≤ 2.1, and $-3.8 \leq x$ (Mm) ≤ 2.5. From left to right, the cases for ideal MHD, resistive MHD, and viscous MHD (models ColdI, ColdR and ColdV) are shown. The driver period is $P \simeq 172$ s.

5.3.3 Heating in very viscous cold loops ($R_e = 10^2$)

In order to get a better understanding on the importance of strong energy dissipation for a footpoint driven oscillating loop, and its effects on heating, we examine the temperature evolution of the ColdV2 model separately, as a special case. We have already seen in Fig. 5.6 that the very high value for shear viscosity ($R_e = 10^2$) resulted in a complete suppression of the KHI in that loop. This suppression eventually leads to a different behaviour for temperature. In Fig. 5.11 we plot the average temperature and average internal energy per height and over time, over the entire $x - y$ plane. We observe an increase of the average temperature towards the apex, with a maximum value of 2.4×10^4 K. These values are higher than the corresponding values for the ColdV model in Fig. 5.9, and are the result of the very high values of the shear viscosity. We also get heating of around $10^3 - 10^4$ K near the footpoint. These values are

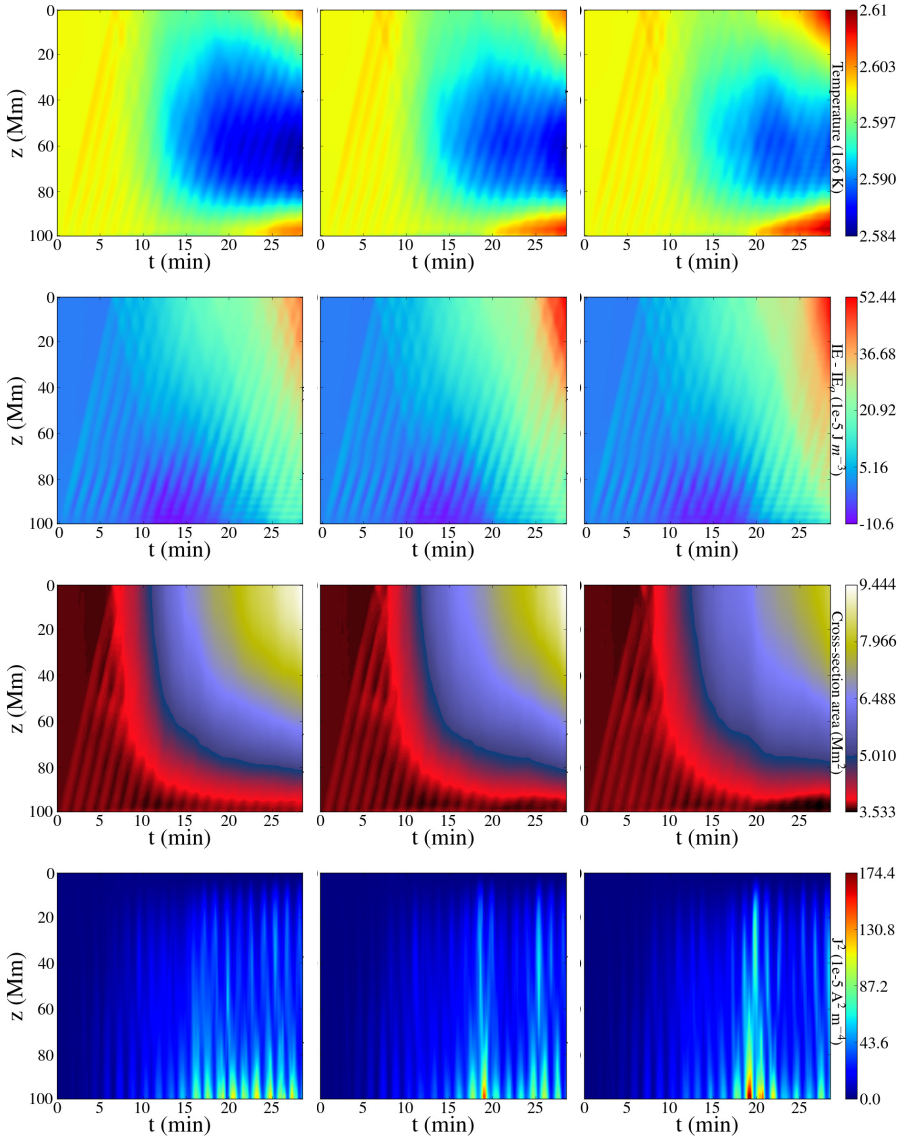

Figure 5.9: From top to bottom row: Average values of temperature or the whole domain, internal energy variation for the whole domain, flux tube cross section surface area for $\rho \geq 0.9\, f(z)$, and square current densities (for $\rho \geq 0.9\, f(z)$) along the z-axis and over time. From left to right, the cases for ideal MHD, resistive MHD, and viscous MHD (models ColdI, ColdR and ColdV) are shown. The apex is located at $z = 0$.

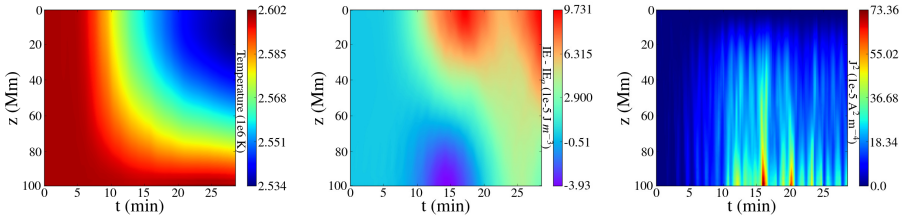

Figure 5.10: Average temperature (*left panel*) and internal energy (*middle panel*) of the entire $x - y$ plane and average square current density (*right panel*) of the flux tube (for $\rho \geq 0.9\, f(z)$) per height and over time. Data depict the ColdIngr model. The period of the driver is $P \simeq 172$ s.

lower than those for the ColdI model, and are caused by the resistive effects of numerical dissipation. The smaller values of currents inside the flux tube ($\rho \geq 0.9\, f(x, y, z)$), as shown in Fig. 5.11, can explain the lower values for temperatures.

The maximum values for temperature at the apex ($\Delta T = 0.298 \times 10^6$ K) are near the boundary of the loop and in the wake behind the oscillating loop, and are caused by the viscous dissipation of energy. This can be seen in the second row of panels in Fig. 5.11 for the cross section at the apex. The heating inside the loop is far less ($\Delta T = 3.2 \times 10^4$ K) and is the effect of energy dissipation, since there is no mixing with the surrounding plasma.

The average internal energy per height and over time of Fig. 5.11 show a similar profile to the corresponding profiles for models ColdI, ColdR, and ColdV. However, the values of the average internal energy are lower than in those cases. This is caused by the lack of any TWIKH rolls for the ColdV2 model, which reduces the amount of smaller scales developing in our loop. Thus the energy dissipation is hindered, and is now confined near the loop boundary layer and the wake that is created behind the oscillating flux tube. The agreement of position between the temperature and internal energy prove that the wave heating is predominately a result of dissipation.

5.3.4 Energy profiles and heating rate

In our attempt to study the energy evolution within our system for models ColdI, ColdR, and ColdV, we need to first calculate the energy fluxes from all the boundaries, including the energy input provided by the driver, and the

energy densities. We start from the MHD equation of energy

$$\frac{\partial e}{\partial t} = \nabla \cdot \left[(e + p_{tot})\, \vec{v} - \frac{\vec{B}\vec{B}}{\mu_0} \cdot \vec{v} \right] = -\nabla \cdot \left(\eta_{\rm r} \vec{J} \times \vec{B} \right) - \nabla \Phi \cdot \rho \vec{v}, \tag{5.8}$$

where the total pressure and gas pressure are given by

$$p_{tot} = p + \frac{B^2}{2\mu_0}, \tag{5.9}$$

$$p = (\gamma - 1) \left(e - \frac{\rho \upsilon^2}{2} - \frac{B^2}{2\mu_0} \right), \qquad \gamma = \frac{5}{3}, \tag{5.10}$$

where $\eta_{\rm r}$ is the electrical resistivity, γ is the ratio of specific heats, and μ_0 is the permeability of vacuum. We rework Eq. (5.8) and reach the following equation, in compact form:

$$K(t) + M(t) + I(t) + G(t) = S_{tot} + F_{tot}, \tag{5.11}$$

where the kinetic ($K(t)$), magnetic ($M(t)$), internal ($I(t)$), and gravitational energy density variations ($G(T)$), the total ($\mathcal{E}(t)$) energy density variation and energy density variation due to the Poynting flux (S_{tot}) and plasma flow (F_{tot}) through the boundaries are calculated as in Beliën et al. (1999) as follows:

$$K(t) = \frac{1}{V} \int_V \frac{1}{2} \rho(t) \upsilon(t)^2 dV' - \frac{1}{V} \int_V \frac{1}{2} \rho(0) \upsilon(0)^2 dV', \tag{5.12}$$

$$M(t) = \frac{1}{V} \int_V \frac{B(t)^2}{2\mu_0} dV' - \frac{1}{V} \int_V \frac{B(0)^2}{2\mu_0} dV', \tag{5.13}$$

$$I(t) = \frac{1}{V} \int_V \frac{1}{\gamma - 1} p(t) dV' - \frac{1}{V} \int_V \frac{1}{\gamma - 1} p(0) dV', \tag{5.14}$$

$$G(t) = \frac{1}{V} \int_V \rho(t) \Phi(t) dV' - \frac{1}{V} \int_V \rho(0) \Phi(0) dV', \tag{5.15}$$

$$\mathcal{E}(t) = K(t) + M(t) + I(t) + G(t), \tag{5.16}$$

$$S_{tot} = -\frac{1}{V} \int_0^t \int_A \left[\eta_{\rm r} \vec{J} \times \vec{B} - \left(\vec{v} \times \vec{B} \right) \times \vec{B} \right] \cdot d\vec{A}' dt', \tag{5.17}$$

$$F_{tot} = -\frac{1}{V} \int_0^t \int_A \left(\frac{\rho \upsilon^2}{2} + \rho \Phi + \frac{\gamma}{\gamma - 1} p \right) \vec{v} \cdot d\vec{A}' dt'. \tag{5.18}$$

The integration is taking place over the whole volume V of our numerical box. The energy input from the driver is the component of Eq. (5.17) from the bottom boundary. The top boundary, which is the location of the apex, has practically zero average input because of the considered symmetry there; the

same amount of energy "enters" and "leaves" the domain through that boundary. From Eq. (5.17) we see that the dominant terms regarding the input energy are the velocities, currents, and magnetic fields. This is a strong hint that once this values are initially the same, the differences in the input energy will be caused by the different dynamical evolution of our systems.

In Karampelas et al. (2017), we plotted the energy density diagrams per time for the total, kinetic, internal, and magnetic energy density, alongside the energy input from the driver. There, we saw the rise of the internal and kinetic energy for the case of the driven oscillations. The observed drop in magnetic energy density there was attributed to the Poynting fluxes through the side boundaries, which had not been considered. In our current analysis, we calculated the energy variation due to Poynting flux (S_{tot}) and plasma flow (F_{tot}) through the side boundaries. After incorporating F_{tot} into the internal energy density variation and S_{tot} into the magnetic energy density variation in our domain, we plot the energy diagrams for the three models of the cold loops (models ColdI, ColdR, and ColdV) in Fig. 5.12. In the calculation of the energy density variations, we consider the entire simulation domain. Since the region of interest has a constant volume, the changes in the energy densities are directly translated into changes in the energies. From now on, we use the terms energy density/energy interchangeably, while discussing the results of Fig. 5.12. Finally, we need to stress an important factor in our analysis. By redefining the internal and magnetic energy variation so that they include the fluxes through the side boundaries, we are essentially calculating the contribution of the input energy to the magnetic and internal energy in each model.

Starting from the magnetic energy (minus the Poynting fluxes from the side boundaries), we obtain a similar and relatively steady linear growth in all three models. Part of the driving energy is used for increasing the energy of the magnetic field. The highest values of the input energy are found for the viscous set-up, and its lowest for the ideal MHD set-up. The reasons for that are the slight differences in the magnetic field (and consequently the current density) at the foot point, as a result of the dynamical evolution of its system. Another reason that causes this difference is the different value for the electrical resistivity in model ColdR.

Studying the kinetic energy in these three models, we get an almost linear growth for a total of six periods, followed by decelerating growth until around the eighth period. After that, the kinetic energy seems to reach a saturation and only small variations of the average values are observed until the end of the simulations. This is an interesting result when combined with the evolution of the (redefined) internal energy. The contribution to the internal energy shows initially only a small and non-steady increase. However, once the kinetic energy enters the phase of decelerating growth and eventual saturation, the internal

energy exhibits a rapid growth. Given the slower growth of magnetic energy compared to the growth of input energy in the three models, once the kinetic energy starts saturating, wave heating gets stronger. The saturation of kinetic energy takes place when the loop cross section becomes turbulent and smaller scales have developed. These smaller scales reinforce energy cascade which in turn leads to more efficient dissipation through (numerical and physical) resistivity and viscosity. Finally, the higher final values of the internal energy for the ColdR and ColdV models are connected to the corresponding higher values of the input energy for these set-ups.

In all three models, we also obtain a similar increase of the gravitational energy. This slight increase is caused by the redistribution of plasma along the loop, where plasma is moving from the footpoint higher up the loop because of the evolution of the scale height. A small oscillation in the profile of the gravitational energy exists owing to the ponderomotive force, but its amplitude is significantly less than the overall increase, which is thus attributed to wave heating. Finally, once we take the energy fluxes through the side boundaries into account, the total energy variation in our domain is equal to the energy input from the driver. The small differences that are observed between the two quantities can be attributed to the accuracy of the calculations and the inevitable creation of small numerical errors ($\nabla \cdot \vec{B} \neq 0$).

In Fig. 5.12, we also plot the time averaged $1D$ power spectra of kinetic energy, magnetic energy, and pressure at the apex, averaged over the last period. This is justified by the fact that small-scale generation is purely perpendicular to the mean magnetic field and is at its peak during the last period of the simulation. We used a similar approach to Magyar et al. (2017), where we used the *python numpy* version of the $2D$ fft routine to calculate $|f_{k_x k_y}|^2$, where $f = \vec{v}$, $\vec{b}$ and p is the Fourier transform of the velocities, magnetic field, and pressure. The power spectra of velocity, magnetic field, and pressure are then calculated by integrating over a unit bandwidth as follows:

$$E_K(k_\perp) = \sum_{k_x k_y} |\vec{v}_{k_x k_y}|^2, \tag{5.19}$$

$$E_B(k_\perp) = \sum_{k_x k_y} |\vec{b}_{k_x k_y}|^2, \tag{5.20}$$

$$\Pi(k_\perp) = \sum_{k_x k_y} |p_{k_x k_y}|^2, \qquad k_\perp = \sqrt{k_x^2 + k_y^2}. \tag{5.21}$$

During the integration, we assumed isotropy and axisymmetry of the turbulence. The slope of the inertial range seen in the power spectra for the velocities and the magnetic field are steeper ($k_\perp^{-2.8}$) than the spectra of $k_\perp^{-5/3}$ for strong

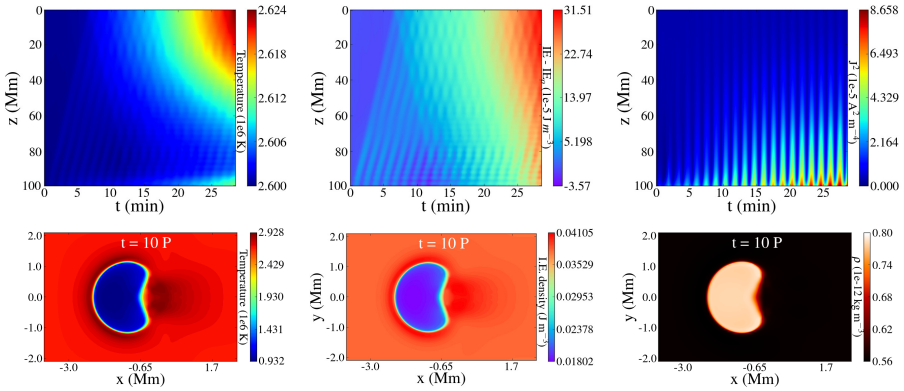

Figure 5.11: *Top row*: Average temperature (*left*) and internal energy (*middle*) of the entire $x-y$ plane and average square current density (*right*) of the flux tube (for $\rho \geq 0.9\, f(z)$) per height and over time. *Bottom row*: Temperature (*left*), internal energy (*middle*) and density (*right*) at the $x-y$ plane at the apex ($z=0$). Data depict the ColdV2 model. The period of the driver is $P \simeq 172$ s.

and $k_{\perp}^{-2}$ for weak incompressible turbulence, making it harder to classify our turbulent spectra. This deviation is most likely caused by our assumption of isotropy and homogeneity, which is not the case in our highly structured domain, as well as the inclusion of compressibility. The isotropy is also violated by the imposition of a directional flow from the continuous driving of the oscillation. The compensated power spectrum for pressure shows a closer proximity to the expected value of $k_{\perp}^{-7/3}$ in the inertial range, and also reveals the effects of dissipation on the length of the inertial range. Including resistivity and viscosity reduces the length of the inertial range.

The differences between the ColdI, ColdR, and ColdV models are relatively small because of the high value of the numerical dissipation. Once we use a very high value for viscosity in the ColdV2 model, we cannot obtain an inertial range any more owing to the limitations of the current resolution. Instead, the spectrum passes rapidly to the dissipation range, even at very small wavenumbers. The amount of energy available at smaller scales is now less than in the other models, hindering dissipation. This can explain the lower values of average internal energy along the loop that we saw in Fig. 5.11.

Finally, in order to explain the differences between the gravitationally stratified and non-stratified models, we plot the time profiles of the input energy for models ColdI and ColdIngr (Fig. 5.13). As we see the total input energy at the end of the simulation is almost three times higher in the ColdI models than

it is in the ColdIngr model. From Eq. 5.17 we know that the dominant terms in the Poynting flux are the velocities, magnetic field and, once considering the existence of physical or effective numerical resistivity, the currents. From our chosen set of parameters for the initial set-ups, both models have the same driver amplitude, driver frequency, an almost identical initial magnetic field and the same eigenfrequency for the fundamental transverse kink mode. As a result, all the differences in the final value for the total input energy are non-linearly caused by the different dynamical evolution of the oscillating loop owing to the presence (absence) of gravity. This energy input difference inevitably affects the energy evolution of the two models. A similar, but less pronounced behaviour is seen between the ColdI, ColdR, and ColdV models as well, which is caused by the differences in the dissipation parameters.

If we consider the last 8.7 minutes of these simulations in Fig. 5.12 and Fig. 5.13, when the curves of both the input and internal energy can be approximated by a linear function, we estimate the following values for the input flux (F_{input} and heating rate (H_r) in our domain:

- $F_{input} = 7.5$ J m^{-2} s^{-1} and $H_r = 2.8$ J m^{-2} s^{-1} $\approx 0.37\, F_{input}$ for the ColdIngr model
- $F_{input} = 42$ J m^{-2} s^{-1} and $H_r = 28$ J m^{-2} s^{-1} $\approx 0.67\, F_{input}$ for the ColdI model
- $F_{input} = 46$ J m^{-2} s^{-1} and $H_r = 37$ J m^{-2} s^{-1} $\approx 0.80\, F_{input}$ for the ColdR model
- $F_{input} = 55$ J m^{-2} s^{-1} and $H_r = 40$ J m^{-2} s^{-1} $\approx 0.72\, F_{input}$ for the ColdV model.

These values are less than half from the $F_{radiative} = 100$ J m$^{-2}s^{-1}$, which is the value for the radiative losses in the quiet corona (Withbroe & Noyes 1977). This shows that the driver in our models does not provide enough energy to sustain the density and temperature profile in the corona. One last observation is the relation between the input energy flux and the heating rate. As we see, the heating rate of the ColdIngr model is $\approx 37\%$ of the corresponding input flux, which is significantly less than the corresponding percentages of the gravitationally stratified models. This is related to the differences in the initial conditions between the gravitationally stratified and non-stratified models, like the internal energy distribution, and higher mass near the apex where the dissipation seems more pronounced. This shows that the inclusion of gravity generally leads to a more effective wave energy dissipation, for our given models, and should be considered in future studies.

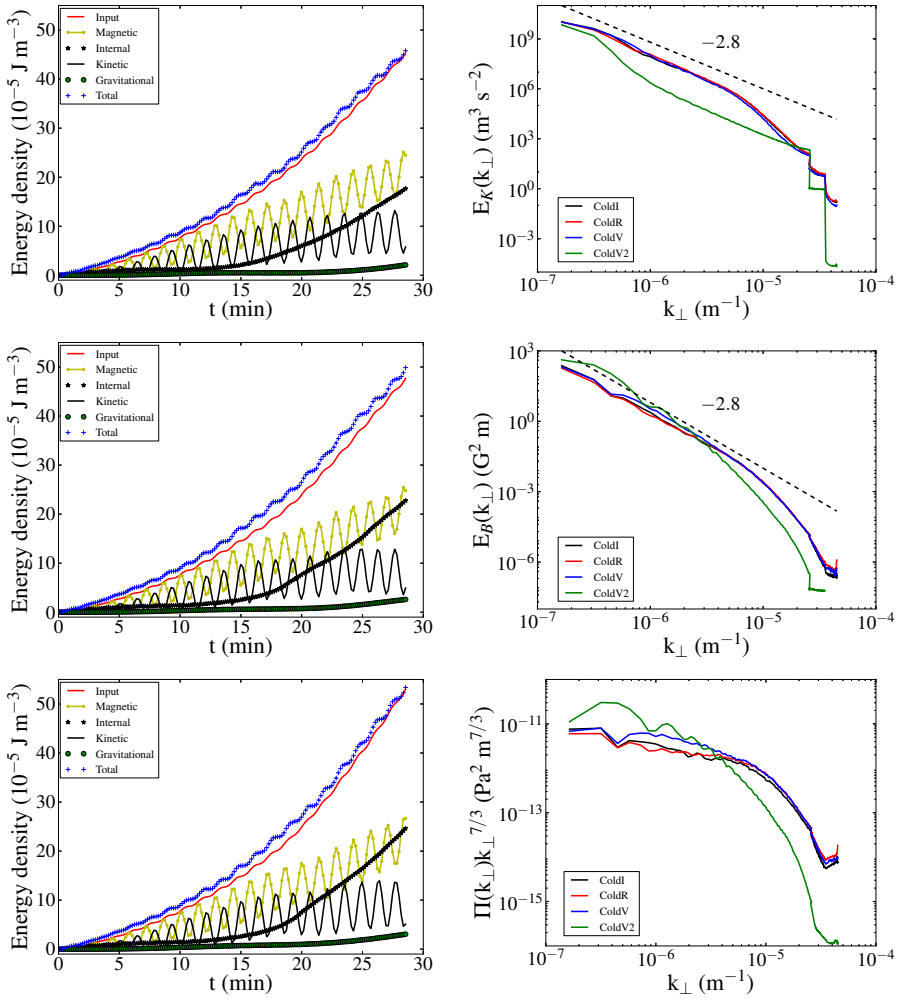

Figure 5.12: *Left column*: Time profiles for the internal, magnetic, kinetic, and gravitational energy density variations relative to the initial state, total (internal+magnetic+kinetic+gravitational) energy density difference, and energy density provided by the driver. All the quantities are volume averaged for the whole computational domain. From top to bottom: ColdI, ColdR, and ColdV models. The contributions from the Poynting flux and energy flux due to the plasma displacement through the side boundaries, have been incorporated to the magnetic and internal energy densities. *Right column*: Time averaged $1D$ power spectra of kinetic energy (*top panel*), magnetic energy(*middle panel*), and pressure (*bottom panel*) at the apex, averaged over the last oscillation period, for the ColdI, ColdR, ColdV, and ColdV2 models.

5.4 Discussion and conclusions

In the current study, we wanted to quantify the effects of gravitational stratification and finite resistivity and viscosity on the magnitude and location of wave heating caused by standing transverse waves in coronal loops. We performed 3D numerical simulations of single 3D, gravitationally stratified, density-enhanced straight flux tubes in ideal, resistive, and viscous MHD. Through a parameter study, we estimated the effective values of numerical resistivity and viscosity present in our set-ups, which are many orders of magnitude larger than the expected values in the solar corona. The effects of physical dissipation, gravity, and driver strength were studied for a cold loop embedded in a hot corona and hot loops inside a colder corona. A non-stratified loop with uniform temperature was used in ideal MHD to determine the effects of numerical dissipation on our results. The standing transverse waves in our models were produced with the use of a continuous, monoperiodic, footpoint driver; the frequency was equal to the analytically predicted value for the standing fundamental kink oscillations of uniform flux tubes (Edwin & Roberts 1983; Andries et al. 2005).

The effects of numerical resistivity were addressed in a model of a non-stratified loop with uniform initial temperature (UniT). In that simulation we obtain an increase of the average temperature near the footpoint and near the apex (Fig. 5.7). This heating is caused by the numerical dissipation found in our code, which effectively acts as resistivity and viscosity in the case where ideal MHD is used. As we expect from Karampelas et al. (2017) for loops undergoing a standing kink oscillation, resistivity is the main cause for heating near the footpoint, while shear viscosity is responsible for heating in the area of the apex. This simulation was used as a template to better understand the temperature evolution in our other set-ups.

Expanding upon our previous work (Karampelas & Van Doorsselaere 2018), we have the creation of spatially extended TWIKH rolls. As a consequence of continuous driving, these TWIKH rolls expand across the loop cross section, fully deforming the initial monolithic density profile. Just like in the non-stratified case studied in that paper (see also the previous chapter), the TWIKH rolls created elongated strand-like structures along the flux tube. These strands, which resemble those studied in Antolin et al. (2016) for an impulsive standing kink wave, are also visible in the cases of resistive and viscous MHD (see Fig. 5.5). In Howson et al. (2017b), the development of KHI in impulsively oscillating flux tubes is hindered in the presence of resistivity and especially viscosity. For the driven oscillations considered in this work, the KHI was still delayed for similar values of the dissipation coefficients. However, the TWIKH rolls eventually expand throughout the loop cross section, similar to the set-up

with ideal MHD (Fig. 5.6).

By increasing the value of shear viscosity, we found that we need very low Reynolds numbers (we used $R_e \sim 10^2$) to suppress the development of the KHI when continuous drivers are used. The use of such a high value for shear viscosity, however, leads to an unusual temperature profile for an oscillating cold loop. The suppression of KHI prevents the mixing of plasma between the loop and the surrounding plasma. At the same time, we found a strong heating taking place near the apex, rather than the footpoint as is expected for loops transversely oscillating in the fundamental kink mode (Van Doorsselaere et al. 2007). This heating is obtained both in the temperature and internal energy profiles, and is connected to phase mixing taking place at the resonant layer. This shows that very high values of viscosity in the corona should not be expected, unless the corresponding heating signatures at the apex of oscillating loops are also observed.

Studying the temperature profiles along the loop axis and over time for a non-stratified cold loop (model ColdIngr), we obtain a slight temperature increase near the footpoint owing to ohmic dissipation due to numerical dissipation. However, the average temperature shows an apparent drop higher up the loop due to KHI induced mixing between plasma of different temperatures. These results are in agreement with our past studies (Karampelas et al. 2017), where a weaker driver was employed. Energy dissipation takes place all along the loop axis; the strongest values are acquired near the apex. A different temperature profile was acquired when comparing with the models of cold gravitationally stratified loops. An increase of the average temperature of our domain was seen near the footpoint and apex, despite the mixing effects (Fig. 5.9). Gravity seems to affect the evolution of our systems greatly, since the corresponding set-up in Karampelas et al. (2017) and the model ColdIngr predominately showed apparent cooling over our domain. The temperature increase in the stratified loops was located near the footpoints and apex in accordance with the results of the loop with uniform temperature. This temperature increase was also accompanied by an increase of the internal energy all along the loop length, and took its highest values near the apex. This proves that this temperature increase is not just an apparent phenomenon, but the result of actual wave heating. The temperature profiles are in agreement with the expected results from Van Doorsselaere et al. (2007) for these types of standing modes. However, the heating for the gravitationally stratified models is still between 28% and 40% of the radiative losses ($F_{radiative} = 100$ J m$^{-2}s^{-1}$) for the quiet corona (Withbroe & Noyes 1977), so it is still not enough to sustain the known coronal temperatures.

By including physical dissipation ($R_e = 10^4$ for the ColdV and $R_m = 10^4$ for the ColdR model), the internal energy increased more along the entire loop.

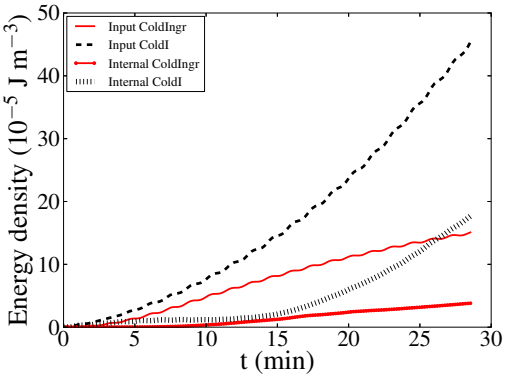

Figure 5.13: Time profile of the input energy density from the driver and internal energy density variation relative to the initial state for the ColdI and ColdIngr models. The quantities are volume averaged for the whole computational domain; the contributions from the energy flux due to the plasma displacement through the side boundaries have been incorporated to internal energy densities.

Both resistivity and viscosity seem to increase the internal energy near the apex (Fig. 5.8), and viscosity causes higher temperatures there ($\sim 5 \times 10^4$ K increase). Near the footpoint, we would expect the resistive case to lead to the highest temperature increase, since the square current densities (dominated by J_z^2) have their highest values there for all three models. The reason why the viscous case shows higher average temperatures at the footpoint as well is the shrinking of the viscous cross section there, as seen in the zt profile for the tube surface area of the ColdV model, combined with the resistive heating due to numerical dissipation. This leads to an apparent effect of higher average temperature than in the ideal or resistive MHD model.

The similar evolution of the square current densities in Fig. 5.9 for models ColdR and ColdV, the similar dynamical evolution, and their differences from the ideal MHD case hints at a description of resistivity in terms of turbulent viscosity, or (shear) viscosity as in terms of anomalous resistivity. Additional simulations with very low values of magnetic Reynolds numbers ($R_m \leq 10^2$) need to be considered in order to study their effect on the energy and dynamical evolution of oscillating loops, determining whether such high values of resistivity exist in the solar corona.

Studying the energy profiles for models ColdI, ColdR, and ColdV, we see the average value of the magnetic energy density (minus the Poynting fluxes from the side boundaries) showing a steady, almost linear growth, similar in all

models. A similar small growth was also found for the gravitational energy density because of the redistribution of plasma along the loop. The input energy from the driver showed a faster growth, reaching different values for each set-up due to the differences in the models dynamical evolution over time. For the kinetic energy of the three models, we identified a phase of a linear growth during the first six periods, a phase of decelerating growth for two more periods, and saturation phase at the later stages of the simulation. Once the kinetic energy enters the phase of decelerating growth and eventual saturation, the internal energy (minus the fluxes due to plasma flow through the boundaries) exhibits a rapid growth.

The development of a turbulent profile of our loops leads to the cascade of energy into smaller scales and more efficient heating. It is during this turbulent phase, once the inertial range is formed in the spectra, that the kinetic energy saturates. This further supports the connection between the kinetic energy saturation and the more efficient heating. The lack of smaller scales for the highly viscous ColdV2 model leads to a lack of efficient energy cascade, as proved by the practically non-existent inertial range in its power spectra in Fig. 5.12. This results in less energy at higher wavenumbers, and less efficient dissipation, as was proven in Fig. 5.11. This proves that a turbulent loop profile is needed for more efficient wave heating. In combination with past results (Magyar & Van Doorsselaere 2016; Magyar et al. 2017; Karampelas & Van Doorsselaere 2018), we conclude that the use of monolithic density profiles for flux tubes should be done with care.

We saw that the inclusion of gravity in our models plays an important role when it comes to the development and efficiency of wave heating. More specifically, stratified loops of the same eigenfrequency and initial magnetic field as a non-stratified loop showed a greater increase of internal energy with respect to their corresponding input energy, when compared to non-stratified loops. The lack of gravity seems to underestimate the efficiency of wave heating in straight flux tube models of coronal loops. Therefore, this should not be ignored in future studies.

To sum up our conclusions, we see that the inclusion of gravity in our models seems to play an important role when it comes to the development and efficiency of wave heating. The inclusion of physical dissipation should also be considered in any attempts to map the location of wave energy dissipation. Energy dissipation seems to be more efficient once the kinetic energy of our loops reaches a saturation phase, for a turbulent loop profile. Simulation with higher resolution (and thus lower numerical dissipation coefficients) are expected to lead to the turbulent profile faster, for the given parameters used here. However, once the inertial range is formed, dissipation should lead to the saturation of energy. Another important result is that resistivity and shear viscosity lead

to the development of the smaller scales in a similar fashion. Driver induced TWIKH rolls develop in our set-ups unless very high dissipation is used (for example a Reynolds number of $R_e = 10^2$). In case of very high viscosity, the development of smaller scales is hindered, heating inside the loop is suppressed, and temperatures are increased predominately near the apex. Future steps should include more physical mechanisms (thermal conduction and radiation) and a more realistic atmosphere than that considered here. Finally, drivers of different amplitudes and frequencies need to be considered in an attempt to determine the amount of energy required for sustained wave heating, while obtaining results that agree with the observed oscillation profiles in loops.

Chapter 6

Amplitudes and energy fluxes of decayless oscillations.

"We are trying to prove ourselves wrong as quickly as possible, because only in that way can we find progress."
Richard P. Feynman

Abstract
In this chapter we focus our study on the energy load of the recently observed decayless kink oscillations in coronal loops. Our aim is to investigate the correlation between the observed amplitudes of the oscillations and the input energy flux from different drivers, as well as to compare with the estimated energy fluxes from the synthetic observations. We perform 3D ideal MHD simulations in straight flux tubes for different drivers, in the presence of gravity. Synthetic images at different spectral lines are constructed with the use of the FoMo code. The development of the KHI leads to mixing of plasma between the flux tube and the hot corona. Once the KHI is fully developed, the amplitudes of the decayless oscillations show only a weak correlation with the driver strength. We find that low amplitude decayless kink oscillations may correspond to significant energy fluxes of the order of the radiative losses for the Quiet Sun. A clear correlation between the input energy flux and the amplitudes derived from our synthetic imaging data cannot be established. Stronger drivers lead to higher vales of the line width estimated energy fluxes. Finally, estimations of the energy fluxes by spectroscopic data are affected by the LOS angle, favouring

combined analysis of imaging and spectroscopic data for single oscillating loops.

This chapter is based on the work by Karampelas et al. (2019b).

6.1 Introduction

Over the past twenty years, observations of the Sun have shown the existence of waves and oscillations throughout the solar corona (Aschwanden 2006; De Moortel & Nakariakov 2012). The discovery of transverse magnetohydrodynamic (MHD) standing (Aschwanden et al. 1999; Nakariakov et al. 1999) waves in coronal loops, and propagating waves in open magnetic field structures (Verwichte et al. 2005) has led to many observational and numerical studies. The ubiquity of such waves has also been established in prominence threads (Okamoto et al. 2007), coronal loops (McIntosh et al. 2011), as well as greater areas of the corona (Tomczyk et al. 2007; Tomczyk & McIntosh 2009; Thurgood et al. 2014; Morton et al. 2016), renewing the interest on the effects of these waves in the solar atmosphere.

Analytical studies on the nature of the transverse oscillations in inhomogeneous plasmas (Zajtsev & Stepanov 1975; Ryutov & Ryutova 1976; Edwin & Roberts 1983) have described the different waves expected in a non-uniform plasma. In order to explain the observed damping of such oscillations (Tomczyk & McIntosh 2009; Verth et al. 2010; Terradas et al. 2010; Pascoe et al. 2016a, 2017; Pascoe et al. 2019), extensive theoretical and numerical work has also been performed. The mechanism of resonant absorption (also known as mode coupling) (Sakurai et al. 1991; Goossens et al. 1992; Ruderman & Roberts 2002; Arregui et al. 2005; Goossens et al. 2011; Pascoe et al. 2012, 2016b; De Moortel et al. 2016; Yu et al. 2017; Pascoe et al. 2018) are considered the reason behind this spatial and temporal attenuation of the oscillations, by transferring the energy of the global kink mode to local azimuthal Alfvén modes. Through phase mixing (Heyvaerts & Priest 1983; Soler & Terradas 2015), the energy is then transferred to ever decreasing smaller scales until it gets dissipated by resistivity and viscosity (Ofman et al. 1994a,b; Poedts & Boynton 1996; Ofman et al. 1998). Observational studies of waves in the solar chromosphere and corona (De Pontieu et al. 2007b; Tomczyk & McIntosh 2009; Morton et al. 2012) suggest the existence of enough energy flux to sustain the radiative losses of ~ 100 W m^{-2} for the non-active region corona (Withbroe & Noyes 1977). In De Moortel & Pascoe (2012) it was shown that LOS integration of footpoint driven multistrand coronal loop oscillations leads to an underestimation of the wave energy. In Antolin et al. (2017) it was found for a non-driven oscillating

loop that the wave energy ends up underestimated through the localisation of the energy by resonant absorption. Recent simulations of coronal loop waves (Pagano & De Moortel 2017; Pagano et al. 2018; Pagano & De Moortel 2019) have not reported sufficient heating to balance the radiative losses.

Alongside the high amplitude, externally initiated, decaying transverse oscillations in coronal loops (see, e.g., Verwichte et al. 2009, 2010; White & Verwichte 2012; White et al. 2012) a new group of small-amplitude decayless transverse oscillations have been identified in coronal loops (Nisticò et al. 2013; Anfinogentov et al. 2015; Duckenfield et al. 2018), with amplitudes ~ 0.1-0.4 Mm. These decayless oscillations have been interpreted in different ways over the years. They have been treated as continuously driven kink waves with a footpoint driver (Guo et al. 2019b; Karampelas et al. 2019a; Afanasyev et al. 2019), as a self-oscillatory process due to the interaction of the loops with quasi-steady flows (Nakariakov et al. 2016), or as a line of sight (LOS) effect from the development of the Kelvin-Helmholtz instability (KHI) (Antolin et al. 2016) in impulsive standing loop oscillations.

The development of the KH instability has been theorized in plasma structures were standing waves are observed (Heyvaerts & Priest 1983; Browning & Priest 1984; Zaqarashvili et al. 2015; Barbulescu et al. 2019; Hillier et al. 2019), caused by the strong shear velocities generated by the azimuthal Alfvén waves. Recent numerical studies (Terradas et al. 2008; Antolin et al. 2014; Magyar & Van Doorsselaere 2016; Howson et al. 2017a; Terradas et al. 2018; Karampelas et al. 2017; Antolin et al. 2018) have confirmed the development of transverse wave induced Kelvin-Helmholtz (TWIKH) rolls for standing kink waves. Additional work has been performed in order to develop methods of identifying the effects of KHI in oscillating loops (Goddard et al. 2018; Van Doorsselaere et al. 2018). Spatially extended TWIKH rolls have been found in the case of continuously driven standing waves, which fully deform the initial monolithic loop cross-section into a fully turbulent one (Karampelas & Van Doorsselaere 2018; Karampelas et al. 2019a). These spatially extended TWIKH rolls in simulations of continuously driven loops have also been reported as sites of mixing of plasma and heating in the solar corona, by effectively spreading the effects of phase mixing across the cross-section of loops (Karampelas et al. 2017; Guo et al. 2019b; Karampelas et al. 2019a; Afanasyev et al. 2019).

One of the main challenges in creating an efficient wave heating model is to find a way of providing a high enough energy flux over large periods of time, while still remaining within the constraints imposed by the observational data. The decayless oscillations seem to be ideal candidates for prolonged energy input in such a model, and also pose the constraint of having relatively small oscillation amplitudes. In Guo et al. (2019b), the use of a mixed Alfvén and transverse footpoint driver suggested as a way of increasing the total energy

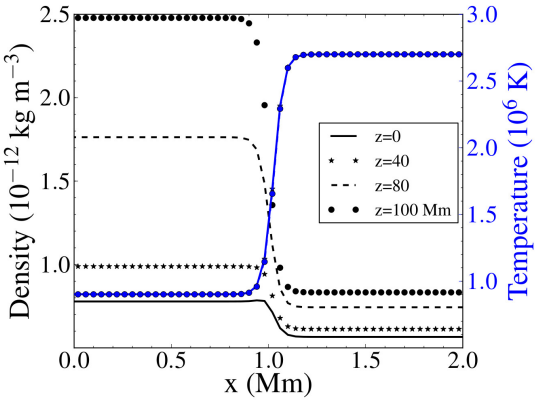

Figure 6.1: Radial profile of the initial density (with black) and temperature (with blue) for our gravitationally stratified, cylindrical flux tubes at different heights, right before the introduction of the driver. The apex is located at $z = 0$ and the footpoint at $z = 100$ Mm. $x = 0$ is the centre of the loop at $t = 0$.

input while retaining small amplitudes in the synthetic images. The authors in Afanasyev et al. (2019) suggest the use of broadband drivers as a way to include additional energy for a decreased observational impact, while still maintaining sufficient energy input. In the current work, we study the effects of transverse footpoint drivers of different strengths on the observational signatures of the induced oscillations in synthetic images. The aim is to detect the existence of a correlation between the input energy flux and the oscillation amplitudes and to determine the observed fluxes from synthetic spectroscopic and imaging data, and set possible constraints for future work.

6.2 Material and Methods

6.2.1 Basic setup

For our $3D$ simulations, we use straight, density-enhanced magnetic flux tubes in a low-β coronal environment, following Karampelas et al. (2019a). This setup models gravitationally stratified, active region coronal loops, solving the MHD equations in the presence of numerical resistivity. Each loop has a full length (L) of 200 Mm and an initial minor radius (R) of 1 Mm, which is constant with

height. The radial density profile of our cylindrical flux tubes at the footpoint is

$$\rho(x,y) = \rho_e + (\rho_i - \rho_e)\frac{1}{2}(1 - \tanh((\sqrt{x^2+y^2}/R - 1)\, b)). \tag{6.1}$$

We denote the basic values of our physical parameters with the index i (e) for internal (external) values, with respect to our tube. The external and internal density at the footpoint are equal to $\rho_e = 10^9 \mu\, m_p$ cm^{-3} $= 0.836 \times 10^{-12}$ kg m^{-3} ($\mu = 0.5$ and m_p is the proton mass) and $\rho_i = 3 \times \rho_e$. We denote the coordinates in the plane perpendicular to the loop axis by x and y , and by z the coordinate along its axis. $b = 20$ sets the width of the boundary layer to $\ell \sim 0.3R$. For the models studied, we set the temperature to be constant with height and equal to $T_e = 3 \times T_i = 2.7$ MK. Finally, we consider an initial uniform magnetic field parallel to the flux tube axis (along the z-axis) equal to $B_z = 22.8$ G. This gives us a plasma $\beta = 0.018$.

Gravity varies sinusoidally along the flux tube, corresponding to a semi-circular loop with major radius $L\pi^{-1}$, and takes a zero value at the loop apex ($z = 0$) and a maximum absolute value at the footpoints ($z = \pm 100$ Mm). Due to the hydrostatic equilibrium we have stratification of pressure and temperature along the loop. To counteract the initial pressure imbalance at the loop boundary caused by the gravitational stratification, the magnetic field is restructuring inside the flux tube, once we let the system reach a semi-equilibrium state after one period. By the end of the relaxation period, neither of temperature, pressure, nor density deviate significantly from their initial state, as in Karampelas et al. (2019a). The radial profiles of density and temperature at several positions along the z-axis are shown in Fig. 6.1.

6.2.2 Boundary conditions and driver

Our tubes are driven from the footpoint ($z = 100$ Mm), using a continuous, monoperiodic 'dipole-like' driver (Karampelas et al. 2017), inspired by that used by Pascoe et al. (2010). The period of the driver is $P \simeq 2L/c_k$, coinciding with the corresponding fundamental eigenfrequency for our gravitationally stratified flux tube (Edwin & Roberts 1983; Andries et al. 2005). For a kink speed of $c_k = 1167$ km s^{-1} we obtain a period of $P = 171$ s. The driver at the bottom boundary has a uniform and time varying velocity inside the loop,

$$\{v_x, v_y\} = \{v(t), 0\} = \left\{ v_0 \cos(\frac{2\pi t}{P}), 0 \right\}, \tag{6.2}$$

where v_0 (in km s^{-1}) is the peak velocity amplitude. Outside the loop, the velocity follows the relation

$$\{v_x, v_y\} = v(t)R^2 \left\{ \frac{(x-\alpha(t))^2 - y^2}{((x-\alpha(t))^2+y^2)^2}, \frac{2(x-\alpha(t))y}{((x-\alpha(t))^2+y^2)^2} \right\}, \tag{6.3}$$

where $\alpha(t) = v_0\,(0.5\,P/\pi)\,\sin(2\pi t/P)$ is a function that recentres the driver, tracking the footpoint. A transition region following the density profile exists between the two areas, in order to avoid any numerical instabilities due to jumps in the velocity.

We study five different models ("D1", "D2", "D4", "D6", and "D8",), each for a different corresponding value of $v_0 = 1$, 2, 4, 6 and 8 km s^{-1}.

At the bottom boundary, we also keep the velocity component parallel to the z-axis (v_z) antisymmetric ($z = 100$ Mm) and we extrapolate the values for density and pressure, using the equations for hydrostatic equilibrium. A zero normal gradient condition is used to extrapolate the values of each magnetic field component through the bottom boundary. Studying the fundamental standing kink mode for an oscillating flux tube allows us to take advantage of the inherent symmetries of this mode, as well as the symmetric nature of our driver. In the top boundary at $z = 0$, the location of the loop apex, we kept v_z, B_x, and B_y antisymmetric in the $x - y$ plane at the apex. The rest of the quantities on that boundary are defined as symmetric. Thus, only half the loop is simulated along the loop axis. All side boundaries are set to outflow (Neumann-type, zero-gradient) conditions for all variables.

6.2.3 Numerical method and grid

The 3D ideal MHD problem is solved using the PLUTO code (Mignone et al. 2018), with the extended GLM method from Dedner et al. (2002) keeping the solenoidal constraint on the magnetic field. We use the finite volume piecewise parabolic method (PPM) and the characteristic tracing method for the timestep. The domain dimensions are $(x, y, z) = (16, 6, 100)$ Mm for models D1, D2 and D4, and $(x, y, z) = (16, 10, 100)$ Mm for models D6 and D8. The latter was chosen in order to properly resolve the expanded turbulent loop cross-section from the stronger drivers. We have cell dimensions of $40 \times 40 \times 1562.5$ km for all models. The resolution is higher in the $x - y$ plane, to better resolve the small-scale structures that appear in the loop cross section. The density scale height of our setup is 28 Mm, and is close to the value of the loop major radius $L\pi^{-1} \sim 64$ Mm. Alongside the lack of radiation or thermal conduction, this allows for a coarser resolution on the z-axis, that can still sufficiently model the density stratification along the flux tube. In all of our models, we also have

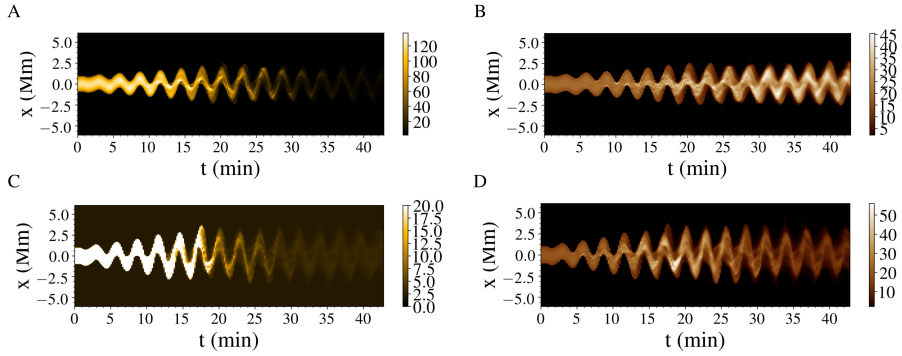

Figure 6.2: Synthetic time-distance maps for the D2 model in the Fe IX 171 Å **(A)** and Fe XII 193 Å **(B)** and for the D4 model in the Fe IX 171 Å**(C)** and Fe XII 193 Å **(D)** lines at the apex. The time distance maps show the emission (in $ergs\ cm^{-2}s^{-1}sr^{-1}$) for the numerical resolution panels of our model. For the D4 model, the intensity in the 171 Å line is saturated, in order to clearly depict the drop in the emission. The LOS angle is 0°.

the inevitable numerical dissipation effects, which lead to values of effective resistivity and viscosity many orders of magnitude larger than the expected ones in the solar corona.

6.2.4 Forward modelling

We use the FoMo code (Van Doorsselaere et al. 2016) to create synthetic images and compare to real observations. We focus on the use of the Fe XII 193 Å emission line, with maximum formation temperature of $\log T = 6.19$, in order to create spectroscopic data of our flux tubes. The 193 Å line tracks the warmer flux tube boundary layer (Antolin et al. 2016, 2017) and is better suited for our studies of driven oscillations with turbulent cross-sections (Karampelas et al. 2019a). The same analysis has been performed for the Fe IX 171 Å line. This line has a maximum formation temperature of $\log T = 5.93$, and is more sensitive to the colder plasma from the loop interior. We also use the 'Imaging' functionality of 'fomo-c' from FoMo, in order to create emission images for the corresponding AIA channels.

We create time-distance maps of the loop apex for each model, by placing a slit at LOS angles equal to 0° (perpendicular to the direction of the oscillation, or x axis), 45° and 90° (parallel to the direction of the oscillation).To better compare

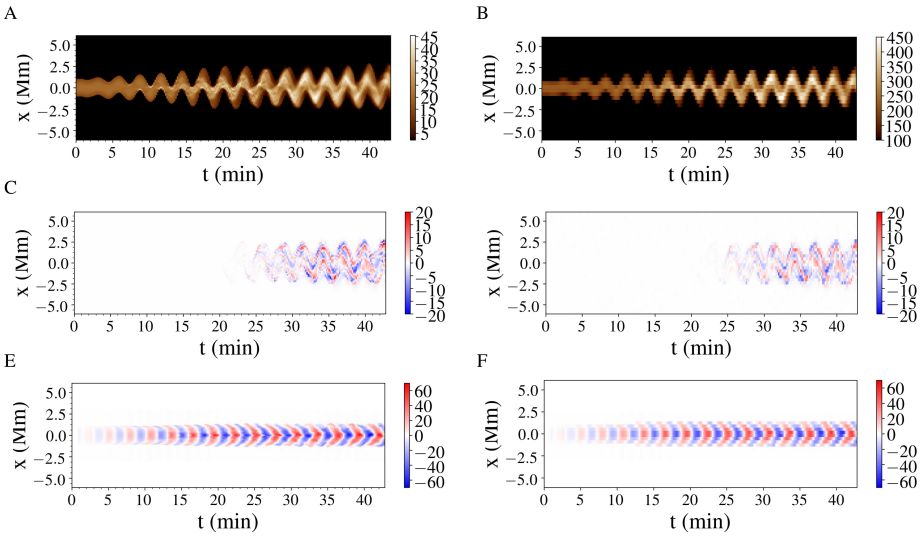

Figure 6.3: Forward modelling results for the D2 model in the Fe XII 193 Å line at the apex. The left panels show the images for numerical resolution and the right panels the images for the targeted instruments. **(A)** and **(B)** show the emission intensity (in $ergs\ cm^{-2}s^{-1}sr^{-1}$) for numerical and for AIA resolution respectively. **(C)** and **(D)** show the Doppler velocity (in km s^{-1}) at 0°, for numerical and for EIS resolution respectively. **(E)** and **(F)** is the Doppler velocity (in km s^{-1}) at 90°, for numerical and for EIS resolution respectively.

to the observations of decayless coronal loop oscillations, we degrade the original spatial resolution of the AIA synthetic images to that of SDO/AIA (0″.6). Then we resample the data to match the pixel size of the target instrument. A similar process is used for the spectroscopic data, where we try to mimic Hinode/EIS by taking a plate-scale of 1″ and a Gaussian PSF of 3″ FWHM (Antolin et al. 2017; Guo et al. 2019b), while also adding poisson distributed photon noise. For the spectroscopic data we also reduce the initial spectral resolution from 3 km s^{-1} to 36 km s^{-1} for the degraded spectrum. The temporal resolution is kept at ~ 11 s, which is very close to both that of AIA and EIS instruments.

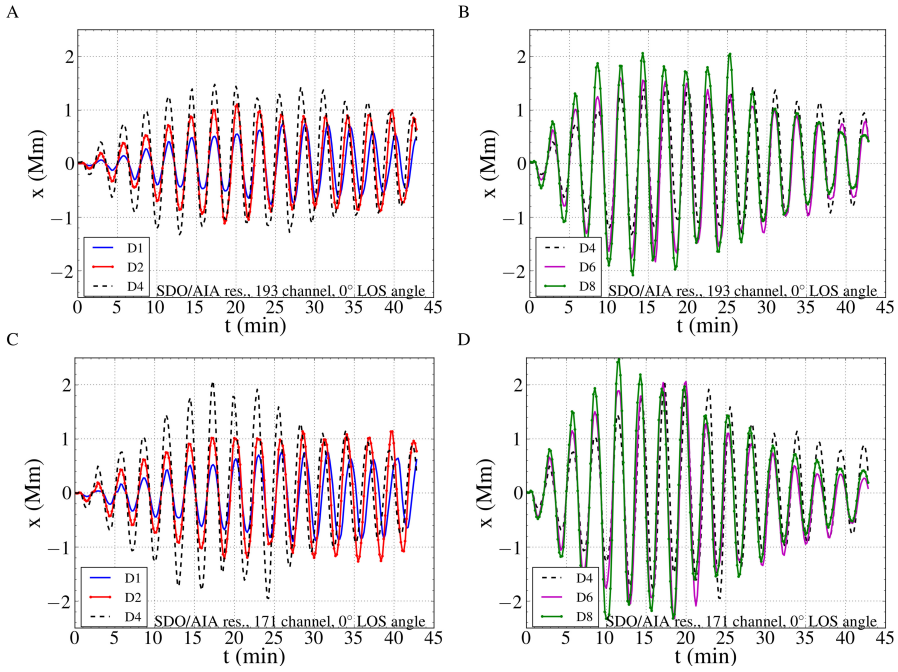

Figure 6.4: Time distance maps of the oscillation amplitude for the five models. The apex displacements were obtained by tracking the loop edge in synthetic emission images of the Fe XII 193 Å line for **(A)** and **(B)** and of the Fe IX 171 Å line for **(C)** and **(D)**, at 0°

6.3 Results

We drive our loops for fifteen cycles. As in Karampelas et al. (2017), the first waves to reach the apex ($z = 0$) are the azimuthal Alfvén waves at the boundary layer of our tube, thanks to their higher propagation speed, followed by the propagating kink waves. Because of the symmetry at the apex, the driver induced waves lead to the initiation of a standing oscillation resembling the fundamental kink mode for gravitationally stratified loops (Andries et al. 2005; Magyar et al. 2015; Karampelas et al. 2019a).

Once the standing mode is initiated, we have the gradual development of the KH instability and the expansion of the flux tube cross-section (Karampelas et al. 2017). The values of the effective numerical dissipation coefficients are low enough not to hinder the development of the instability (see Karampelas et al.

2019a). By performing forward modelling for our setups, we construct time distance maps of our oscillations at the apex, for the different spectral lines. Two examples of these forward modelling time-distance maps are presented in Fig. 6.2. There we see the apex displacement over time for the D2 and D4 models in the 171 Å and 193 Å AIA channels. As expected for loops with turbulent cross-sections (Karampelas et al. 2019a), the development of the KH instability and the spatially extended TWIKH rolls lead to extensive mixing of the loop with the surrounding plasma. For our setup of a cold loop embedded in a warmer corona, this leads to a big emission drop in the Fe IX 171 Å line.

By saturating the image of the 171 Å emission line for model D4, we can see that this drop occurs faster for stronger drivers. A smaller drop is also obtained in the 193 Å line, for stronger drivers, and is caused by the drop of the average density of the emitting plasma, and its mixing with the surrounding plasma (Karampelas et al. 2017), due to the spatially extended TWIKH rolls. In coronal observations we expect to mostly see the cooling stage of loops (Viall & Klimchuk 2012). The loops observed performing these decayless observations are expected to be driven for long periods of time, while cooling from higher initial temperatures. Hence, the observed decayless regime should correspond to the later stages of our simulations, where we observe the mixing induced emission drop.

In Fig. 6.3 we present additional synthetic images for the D2 model, both at numerical and instrument resolution. In that figure, we see the 193 Å AIA channel for the emission intensity at 0° LOS angle, as well as the Doppler velocities for the Fe XII 193 Å line at 0° and 90° angles. We see the development of emission peaks prior to the development of the TWIKH rolls, due to the excitation of higher order harmonics and the deformation of the flux tube from the combined effect of the inertia and fluting modes (Andries et al. 2005; Ruderman et al. 2010; Yuan & Van Doorsselaere 2016; Antolin et al. 2017; Terradas et al. 2018). Once the KHI develops, we get the emergence of stronger emission peaks in the 193 Å channel, stronger Doppler velocities perpendicular to the direction of the oscillation, and the gradual expansion of the resonant flows across the loop cross-section (Antolin et al. 2015; Karampelas & Van Doorsselaere 2018). The latter is evident in the bottom panels of Fig. 6.3, where we look at the loop from the side. These out of phase movements from the TWIKH rolls are present in all of our models and get more intense and spatially extended the stronger each driver is.

We track the oscillations in the constructed time-distance maps for our models by setting a threshold value off $I_{thr} = I_{min} + 0.1(I_{max} - I_{min})$, where I is the intensity across the loop on each frame, I_{max} is its maximum value and I_{min} is the background intensity. The point with this intensity is defined as the 'edge' of the loop. A spline interpolation for the position is used to inhibit tracking

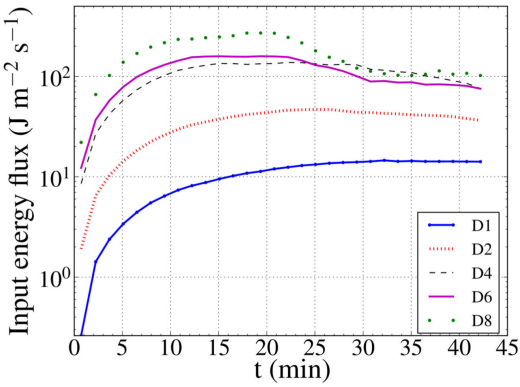

Figure 6.5: Evolution of the average values of the energy fluxes provided by the driver of each model (in W m^{-2}) over time.

errors, with the number of interpolation points being half the number of frames in the TD map. We present the displacement of the apex for each loop in Fig. 6.4, where panels for all the models are shown at a 0° LOS angle. An initial increase of the amplitude is followed by saturation and an eventual drop in the second half of the simulations. This is the stage of the simulations where the decayless regime should correspond to. In the last stages, we see that the D2 and D4 models show similar values of displacement, while the D6 and D8 models show lower amplitudes than the former ones.

Similar profiles are obtained for both emission lines used in the present work. The synthetic images in the 171 Å line show higher initial amplitudes than those in the 193 Å line. This is because the loop core has the highest transverse velocities before the development of the KH instability. The loop boundary layer has radially decreasing v_x velocities, as result of the driver shape that we use at the footpoint, leading to smaller displacements than the loop core, as seen in the two emission lines, each being more sensitive to the corresponding loop region. A similar thing was found in Antolin et al. (2016). In that work, the loop core showed a higher oscillation amplitude than the loop boundary layer, before the initiation of the KHI. In our models, the constant driving leads to overall stronger displacements, while the deformation of the loop cross-section leads to higher amplitudes in the 193 Å line for the given temperature distribution.

In Fig. 6.4 we get a small phase difference between the D1 model and all the rest. This small change in the phase between the observed displacement and the driving frequency is a LOS effect and caused by the integration of the emission

across TWIKH rolls with varying phases. A similar phase shift was observed for the turbulent layer of oscillating loops performing in Antolin et al. (2016). For the D1 model, the slower development of the KHI leads to a delay in the manifestation of that phase difference. Similar trends have been obtained for synthetic images at 45°, with the difference that the obtained displacements are smaller due to the projection of the oscillation plane on the plane of sky (POS).

In order to determine whether the obtained amplitude drop in Fig. 6.4 is caused purely by the development of strong azimuthal resonant flows and the KH eddies, we plot in Fig. 6.5 the input energy flux (J m^{-2} s^{-1}) for each driver. The Poynting fluxes are calculated for a surface area of 3×3 Mm^2 in the centre of the bottom boundary. This square contains the loop footpoint of each model, and provides 80% of the total energy input from the spatially localized driver. The curves in Fig. 6.5 represent the time evolution of the average values of the fluxes.

We can see that the efficiency of the drivers change over time, with the strongest changes happening for the stronger drivers. These variations with time are the result of the boundary conditions employed here. The zero normal gradient condition for the magnetic field allowed it to freely evolve with time, instead of fixing its value at the footpoint. This is affecting the Poynting flux from the driver in the bottom boundary, causing the evolution of the energy input, similarly to Guo et al. (2019b) and Karampelas et al. (2019a). In the scope of this study, we do not focus on creating a realistic model for a driver, but we focus on the effects of the driver strength on the synthetic data. Therefore, tracking the evolution of the driver efficiency is sufficient within the context of the current study. The initial increase in the energy flux is followed by a drop, which is again more pronounced in the models with the stronger drivers. By comparing the curves for the models D2 and D4 with the synthetic images of Fig. 6.2, we see place that this drop takes place when the loops become turbulent due to the KHI.

Focusing at the last 6 cycles of the the simulation in Fig. 6.5, we see that D4 shows a stronger input than D6, while still remaining weaker than D8. D2 on the other hand remains weaker from all the aforementioned ones, providing almost half or less as much input flux. This is in contrast to the results of Fig. 6.4, where the oscillation amplitude of the D2 model was comparable to that of the D4 model, and higher than the respective amplitudes of models D6 and D8. This shows that the previously obtained amplitudes are affected by the development of the out of phase movements of the spatially extended TWIKH rolls. All the drivers provide fluxes within the range of the radiative losses of the non-active region corona (Withbroe & Noyes 1977), with the exception of D1, which is significantly weaker than the rest.

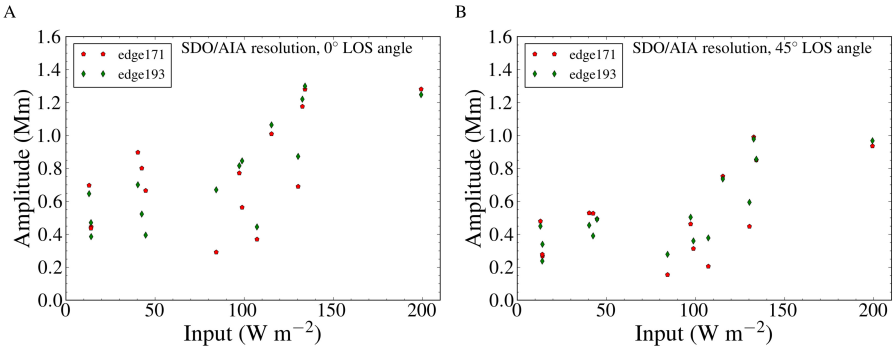

Figure 6.6: Diagrams of the average oscillation amplitudes as a function of the average energy input for each model. In **A** we have a 0° LOS angle and in **(B)** we have a 45° LOS angle. Data from the Fe XII 193 Å line and the Fe IX 171 Å line were used. The loops displacements for the two lines were obtained by tracking their edge in the corresponding synthetic emission images.

After calculating the input energy flux and the loop displacements, we plot amplitude-flux diagrams in Fig. 6.6. For these diagrams, we took the average of the (absolute values) of the maximum displacements and fluxes, for each model, at time intervals $19.95 - 28.5$ minutes, $28.5 - 34.2$ minutes and $34.2 - 42.75$ minutes. The diagrams contain the amplitudes traced from AIA-resolution synthetic images of 171 and 193 AIA channels at both 0° and 45° LOS angle. Taking this and the results from Fig. 6.4 into account, we explain the differences between the 171 and 193 Å AIA channels as LOS effects of our models. The highest values of the amplitudes are obtained for the highest driver input fluxes. However, a clear correlation is absent for fluxes ≤ 110 W m^{-2}. Instead, we see a relatively uniform distribution of amplitudes among the different fluxes in that region. The corresponding amplitudes are below 1 Mm as we look perpendicular to the oscillation direction (0°.) At a LOS angle of 45°, the value of these amplitudes is between 0.15 and 0.55 Mm, placing them within the range of the observed decayless oscillations (Nisticò et al. 2013; Anfinogentov et al. 2015).

Finally, we want to calculate the observed kinetic energy flux (W m^{-2}) across the line of sight, for a specific spectral line. Based on the work of (Antolin et al. 2017), we calculate the Doppler energy flux as:

$$F_{obs} = \frac{1}{2} \int_{\perp LOS} < \rho_{\lambda}(l,t) > v_{Dop,\lambda}(l,t)^2 \frac{c_k}{L_{\perp LOS}} dl_{\perp}, \tag{6.4}$$

and the non-thermal energy flux as:

$$F_{obs} = \frac{1}{2} \int_{\perp LOS} < \rho_\lambda(l,t) > \left(\xi_\lambda(l,t)^2 - \xi_{\lambda,th}(l,t)^2\right) \frac{c_k}{L_{\perp LOS}} dl_\perp. \tag{6.5}$$

With $c_k = 1167$ km s^{-1} we denote the kink speed. $L_{\perp LOS}$ is the length of the domain across the LOS, $v_{Dop,\lambda}$ the Doppler velocity (in km s^{-1}) for the spectral line, ξ_λ the corresponding Doppler width in km s^{-1}, and the thermal width (in km s^{-1}):

$$\xi_{\lambda,th} = \frac{c}{\lambda_0} \sqrt{\frac{T_\lambda k_B}{\mu m_p}}. \tag{6.6}$$

With c we denote the speed of light, λ_0 the wavelength at rest for the spectral line, k_B the Boltzmann constant, m_p the proton mass and with μ the atomic weight in proton masses of the emitting element. The emitting temperature T_λ is taken as an approximation from the $\xi_{\lambda,th}$ in the beginning of the simulations, where the velocities along the LOS are practically zero. The quantity $< \rho_\lambda(l,t) >$ is based on the emissivity-weighted average density from Antolin et al. (2017):

$$< \rho_\lambda(l,t) >= \frac{\int_{//LOS} \rho\epsilon(l,t)ds}{\left(\int_{//LOS} \epsilon(l,t)ds\right)|_{max}}, \tag{6.7}$$

where we instead divide the integral of density times emissivity with the maximum value of the integrated emissivity along the LOS at each frame. The fluxes from all setups are then normalized to the domain dimensions of models D6 and D8 for all setups, to make direct comparisons possible between the different models.

We plot our results for the Fe XII 193 Å spectral line in Fig. 6.7, following Hinode/EIS spatial, spectral and temporal resolution. For a LOS angle of 90°, we get an initial increase in the energy flux estimated by the Doppler velocities, which persisted for the duration of the simulations for models D1 and D2. For the models D4, D6 and D8 we see a drop in the estimated Doppler energy flux, in the last cycles of the simulations. This drop appears once the turbulent loop cross-section shows very strong out of phase flows, due to the TWIKH rolls. These azimuthal flows do not register in the Doppler velocities at this angle, leading to the aforementioned drop. A similar behaviour was noted in Antolin et al. (2017) for a non-driven transverse oscillation. We also see a correlation with the drop of the input energy flux, as observed for the the models D4, D6 and D8. However, a similar correlation is not observed for the D1 and D2 models. This shows that the observed drop in the Doppler energy flux is the combined result of the input drop and the loop deformation by the TWIKH rolls.

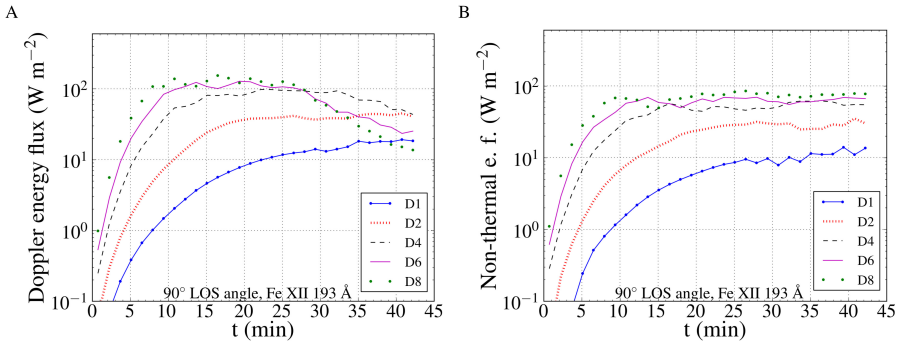

Figure 6.7: Average values of the Doppler **(A)** and non-thermal **(B)** energy fluxes for a LOS angle of 90°, based on synthetic spectroscopic data from the Fe XII 193 Åline.

The diagram of the non-thermal energy flux in Fig. 6.7 shows a saturation once the KHI fully deforms the loop cross-section. This agrees with the results of Antolin et al. (2017), where a similar saturated domain was obtained after the manifestation of the KHI. For the models D4, D6 and D8, this saturation takes place before the drop in the Doppler energy flux. The small increase of the non-thermal energy flux in the later parts of the simulation does not fully compensate for the drop in the Doppler energy flux. This shows that the aforementioned Doppler flux follows closely the input energy flux, in the case of continuously driven oscillating loops. We also see that the non-thermal energy fluxes are increasing for stronger drivers. This suggests that the observed correlation between line widths and Doppler shifts reported by McIntosh & De Pontieu (2012) can correspond to a continuous input of transverse MHD waves, supporting their hypothesis. However, the use of a single loop for each driver excludes the LOS effects of integrating over many structures, and cannot give a safe statistical result to be compared with the observations (McIntosh & De Pontieu 2012).

We see a disagreement between the total obtained (Doppler + non-thermal) energy flux, for a LOS angle of 90°, and the input in Fig. 6.5 for models D1 and D2. The former, as seen in Fig. 6.8 is overestimated with respect to the input energy flux during the later part of the respective simulations. This comes in contrast with the results of Antolin et al. (2017), where the estimated total energy flux was lower than the available energy flux calculated directly from the simulation data. This disagreement is due to the inaccuracies introduced through the method of estimating the density and temperature of the emitting

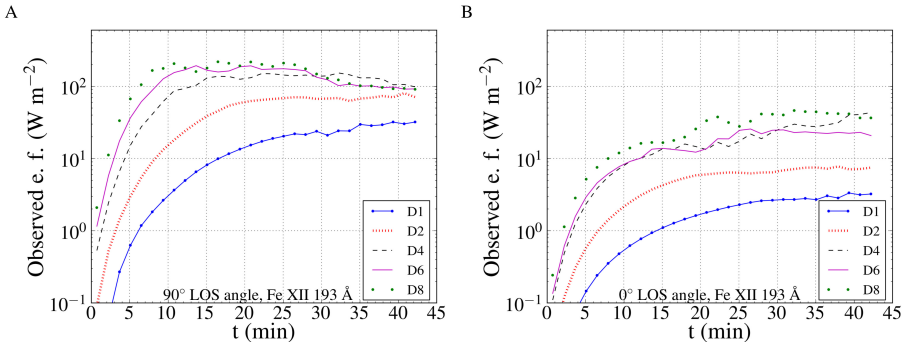

Figure 6.8: Average values of the total 'observed' (Doppler and non-thermal) energy fluxes, i.e. those calculated by the synthetic spectroscopic data from the Fe XII 193 Åline. A LOS angle of 90° **(A)** and 0° **(B)** was considered.

plasma from the synthetic data. The latter appears in the correction for the thermal terms in the non-thermal energy fluxes. Additional uncertainty can be caused by the angle of observation. As seen in Fig. 6.8, the total observed energy for a LOS angle of 0° follows the development of the TWIKH rolls and leads to an underestimation of the energy flux.

The uncertainty revolving around the LOS angle can be bypassed by a combined approach of multiple observations. Once a small angle of observation is identified by combining the energy diagrams and the spectra, like those in Fig. 6.4, we can then approximate the total energy fluxes. We achieve this by adding an additional term to the sum of the Doppler and non-thermal energy fluxes. This additional term is derived from Eq. 6.4, by replacing the Doppler velocities with the the velocity derived from the displacement of the oscillating loop, like in the time-distance maps of Fig. 6.4. The results of this calculation are presented in Fig. 6.9, and show a better agreement with the input energy than the underestimated fluxes in panel (B) of Fig. 6.8.

6.4 Discussion

In the present work we aimed to study the effects of different transverse drivers in the dynamics and energetics of decayless oscillations in coronal loops, through the use of synthetic images. We modelled the decayless oscillations as the standing waves from continuously footpoint-driven straight flux tubes, in the presence of

gravity. We performed MHD simulations for monochromatic footpoint drivers of different strengths, with the frequency coinciding with the natural frequency of the flux tubes, and performed forward modelling to our data, constructing time-distance maps at the loop apex. We then degraded the spatial and spectral resolution of our signal, targeting different instruments, namely the SDO/AIA and Hinode/EIS. From the created acquired synthetic images for the 193 Å and the 171 Å lines we studied the oscillation amplitudes in the plane of sky (POS) at the apex, generated by the five different drivers. To do so, we tracked the 'edge' of the loop from the emission images, which is defined by threshold value for the intensity, set slightly higher than the background intensity.

In Fig. 6.2 we see the drop of the emission in synthetic images for both lines employed here. This drop is the result of the spatially extended TWIKH rolls, expanding the loop cross-section and causing mixing with the surrounding plasma. This drop in the emission is stronger and occurs faster for stronger drivers, as we can see in the example of Fig. 6.2 for the D2 and D4 models. In observations we mostly expect to observe loops during their cooling stage (Viall & Klimchuk 2012), starting from unknown higher temperatures of formation. For decayless oscillations, we therefore expect them to be already in a turbulent state, because of the continuous driving. Any change in the strength of the driver could then lead to sudden changes in the observed emission in various lines, depending on the temperature gradient between the loop and the surrounding plasma, as well as the temperature of said coronal plasma.

In Fig. 6.4 we see that the final values of the amplitudes are comparable between the different models. We are mostly interested in the second half of the simulations, during which the KHI has deformed the cross-section of each loop. This is because we expect the loops performing decayless oscillations to be already in a turbulent state. During that phase, we obtain higher oscillation amplitudes from weaker drivers. This becomes obvious by comparing these time distance maps and the input energy flux diagrams of Fig. 6.5 for the D4 and D8 models. The D4 model showed bigger displacements towards the end of the simulations than D8 model, despite having a less efficient driver at that stage of the simulations. In addition to that, the D2 model showed very similar amplitudes to the D4, D6 and D8 models, despite providing less than half the energy flux of these drivers. This result is a clear indication of the importance of the out of phase flows, developed by the TWIKH rolls, in the characteristics of the observed oscillations.

Following the results of Fig. 6.7, a drop in the Doppler energy flux for the models D4, D6 and D8 was obtained. This drop is primarily related to the respective drop of the input energy flux, and secondarily to the development of the TWIKH rolls, since the drop in the input energy flux of models D1 and D2 is not followed by a drop in their Doppler flux. This is related to the

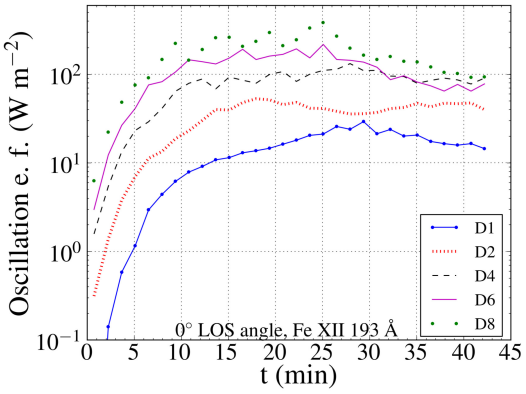

Figure 6.9: Average values of the total obtained (Doppler and non-thermal) energy fluxes with the additional term by tracking the oscillation on the POS. The values are based on the synthetic images for the Fe XII 193 Å line and the 193 AIA channel.

less deformed loop cross-sections expected for weaker drivers in continuously driven oscillations of coronal loops (Karampelas & Van Doorsselaere 2018). The connection between the Doppler energy flux and the resonant flows has also been established in Antolin et al. (2017), for a small-amplitude non-driven transverse oscillation of coronal loop.

From the diagram of the non-thermal energy flux over time in Fig. 6.7, we observe the saturation of the energy flux, attributed to the turbulent motions present across the loop cross-section. We also observe a positive correlation between the average values of the saturated non-thermal energy fluxes and the driver efficiency from Fig. 6.5. This suggests that a continuous input of transverse MHD waves could lead to the observed correlation between line widths and Doppler shifts reported by McIntosh & De Pontieu (2012). However, the small number of measurements (one observation per loop per driver) does not allow us to acquire safe statistical results. Furthermore, our study has excluded the LOS effects of integrating over many structures, which prevents us from making a direct comparison with the observations (McIntosh & De Pontieu 2012).

By taking into account the results of Fig. 6.9, we see that the sum of the non-thermal and Doppler energy flux can lead to different values, depending on the angle of observation and the methods used in the calculations. By adding

an additional term, derived by estimating the oscillation velocity from the time-distance maps, we can compensate for the effects of the observation angle when calculating the energy fluxes.

From the classic theory of damped, resonantly driven oscillator it is known that the saturated value of the amplitude of the oscillation is determined by the value of the damping coefficient (here the numerical dissipation). However, we need to stress that the obtained saturation in the amplitudes in this study is not directly caused by numerical dissipation. Similar results were also found in scaling tests with setups of higher resolution, as well as past results (Guo et al. 2019b; Karampelas et al. 2019a). It is instead the combined result of the strong out of phase flows generated by the TWIKH rolls and the effects of plasma mixing in the emission. The derived energy spectra in Karampelas et al. (2019a) reveal a turbulent profile, represented by the inertial range. The length of the inertial range is determined by the dissipation coefficients. Stronger dissipation reduces its length, and acts on larger spatial scales, as was shown in Chapter 5. As long as the dissipation coefficients are small enough for the inertial range (and turbulence) to form, the oscillation amplitudes will saturate regardless of the dissipation parameters, as soon as the dissipation forms. Dissipation should directly affect the saturation of the amplitudes, only if it is strong enough to suppress the formation of turbulence, as was shown in Karampelas et al. (2019a).

Finally, from Fig. 6.6 we conclude that we cannot obtain a clear correlation between the driver input and the observed oscillation amplitudes just from the synthetic imaging data. In our setups, the amplitudes between 0.15 and 0.55 Mm were evenly distributed over a wide range of input fluxes, up to 110 W m^{-2}. Small amplitude oscillations can potentially be hiding enough energy to sustain the non-active region corona ($\sim$ 100 W m^{-2}) (Withbroe & Noyes 1977). The development of spatially extended TWIKH rolls can mask its observational signatures, by causing out of phase movements of the loop plasma and affecting the emission at various lines. This is relevant when explaining the observed decayless oscillations (Nisticò et al. 2013; Anfinogentov et al. 2015) as the result of continuous footpoint driving of a coronal loop, and stresses the need for combined instrument observations.

To summarize our results, the mixing of plasma caused by the developed KHI affects the emission in synthetic images, leading to a drop once the loop cross-section becomes turbulent. The developed TWIKH rolls show strong out of phase flows, which lead to the saturation of the oscillation amplitudes for each model. For different angles, we obtain oscillation amplitudes near the observed ones, which do not show a clear correlation with the input energy from the driver. These observed amplitudes can potentially carry enough energy to sustain the radiative losses from the Quiet Sun. A better correlation can be obtained

between the input energy and the spectroscopic results from the Doppler energy flux and the non-thermal energy fluxes. All of our results, however, are dependent upon the angle of observations and the approximations used, hinting towards the need for combined spectroscopic and imaging observations.

Apart from our suggestion that small-amplitude decayless oscillations contain enough energy flux to support the QS, there are other ways to introduce additional energy within the context of such observed waves. In De Moortel & Pascoe (2012) it was shown that the wave energy is significantly underestimated by integration of multiple loops along the LOS. In that work, the kinetic energy estimated by the LOS Doppler velocities was $\sim 5\% - 20\%$ of the energy in the domain. A combination of a kink and Alfvén driver (Guo et al. 2019b) can also provide more energy into the system, while retaining a similar profile in AIA synthetic images. Alternatively, the use of a broadband driver might also increase the driver efficiency, for only small deviations from the expected oscillation amplitudes. The detection of such higher harmonics in decayless oscillations by Duckenfield et al. (2018) suggests that the latter method should be studied further in future works.

Chapter 7

Conclusions

"Now this is not the end. It is not even the beginning of the end. But it is, perhaps, the end of the beginning."
Winston S. Churchill

One of the open questions of Solar Physics is the existence of the Sun's million-degrees corona, laying over a much cooler surface. To be able to solve the so called Coronal Heating Problem, it is essential to identify the heating source(s) that is (are) able to balance losses owing to thermal conduction and radiation. As it was already mentioned, the magnetic field dominates the dynamics of the lower solar corona ($\beta < 1$), creating plasma structures like coronal loops. Thus, the coronal heating models are associated with the evolution of the magnetic field. Coronal heating models are usually classified into direct current (DC) and alternating current (AC) models.

For the duration of this PhD, we focused on the study of AC models, and in particular the mechanism of heating by transverse waves. The widespread presence of these waves in the solar atmosphere has already been established over a decade of observations (Aschwanden et al. 1999; Tomczyk et al. 2007; McIntosh et al. 2011). Of particular interest to our research were the recently discovered small-amplitude decayless transverse oscillations (Nisticò et al. 2013; Anfinogentov et al. 2015) in coronal loops. These oscillations, which are considered to be ubiquitous in coronal loops, do not appear to undergo damping, unlike their larger amplitude counterparts.

Studying wave heating in coronal loops, we performed thorough numerical studies (Karampelas et al. 2017; Karampelas & Van Doorsselaere 2018; Karampelas et al. 2019a,b; Guo et al. 2019b; Afanasyev et al. 2019), which

treated these decayless oscillations as footpoint driven waves. These studies mainly focused on the efficiency of wave heating in footpoint driven simulations, and their possible connection to the observed decayless oscillations. In our studies we used codes such as MPI-AMRVAC (Porth et al. 2014) and PLUTO (Mignone et al. 2012) in order to perform 3D simulations of oscillating coronal loops in ideal, resistive and viscous MHD, while also considering the effects of numerical dissipation. We also performed forward modelling on our numerical data, with the use of FoMo (Van Doorsselaere et al. 2016), in order to compare our results with real observations of coronal loops.

Simulations of both (a) footpoint driven and (b) non-driven, freely oscillating loops in Chapter 3 have shown the development of Kelvin-Helmholtz instability (KHI) at the outer layers of loops, as expected from past analytical and numerical work (e.g. Zaqarashvili et al. 2015; Antolin et al. 2014). KHI is linked to the velocity shear at the boundaries, and it has been found to result in extensive mixing of plasma between the loop and the surrounding corona. One of the questions that inspired this PhD was the association between the Kelvin-Helmholtz instability and wave heating, through resistivity and viscosity. Models with uniform initial temperature have yielded results of a weak temperature increase at the locations of the highest velocities (in our models, the apex) and highest currents (loop footpoints for our setups). This hints towards resistive and viscous heating as two possible mechanisms of energy dissipation (Karampelas et al. 2017; Guo et al. 2019b).

In the presence of a temperature gradient between the loop and its surroundings, the aforementioned mixing can potentially mask the wave heating effects, leading to apparent heating or cooling of the flux tube (Karampelas et al. 2017; Afanasyev et al. 2019, see also Chapter 3). By expanding these results in Chapter 5, to setups where gravity was included, we found that energy dissipation is more efficient in gravitationally stratified loops, and that it can lead to heating of the loops and their environment despite the effects of mixing (Karampelas et al. 2019a).

Additional focus was given in Chapter 4 to the spatial and temporal evolution of the flux tube structure. The traditional view of wave heating in loops is based on the dissipation of energy at the resonant layer. The resonant layer is expected near the outer regions, leaving the loop's inner part without any heating sources. This eventually leads to its draining (Cargill et al. 2016), unless an additional heating mechanism is considered. In Karampelas & Van Doorsselaere (2018) we saw that the KHI at the site of the velocity antinode (in our setups, the apex) expands across the entire loop cross-section for footpoint driven oscillations. This leads to the complete disruption of the initial monolithic cross-section of loops, resulting in fully deformed loops. These fully deformed loops address the aforementioned shortcomings of the localized wave heating, by spreading the

resonant layer across the entire cross-section. This result complements a former study by Magyar & Van Doorsselaere (2016), where it was proven that initially multi-stranded loop cross-sections get deformed if they experience constant driving. The combined results of these studies indicate that we should not expect the existence of purely monolithic loops.

This result was later expanded in Chapter 5 Karampelas et al. (based on the work by 2019a), where we identified the manifestation of turbulence in such deformed loop cross-sections. Here we need to stress, that the lack of thermal conduction perpendicular to the magnetic field would hinder 'actual' mixing of plasma. However, if we consider resistivity, then small scale reconnection at the interfaces of the KH eddies could disrupt the magnetic field topology, leading to proper mixing of plasma. This effect is taking place in our simulations, due to numerical dissipation. If we also consider phase mixing due to the propagation of waves in such turbulent plasma structures, then we can justify the qualitative results that we obtain. We have also seen, in Van Doorsselaere et al. (2018), that such turbulent cross-sections can produce broad differential emission measures (DEMs) that are comparable to the observations and are broader than those of impulsively excited oscillating loop models. These broad DEMs are related with multi-thermal plasma along the line of sight, and were traditionally attributed to multi-stranded loops.

As a concluding study to our previous research was a parameter study that we performed Karampelas et al. (2019b), and present in Chapter 6. This study involved simulations of driven loop oscillations for different driver strengths and the creation of forward modelled data for our turbulent loop cross-sections. The development of KHI results in strong out-of-phase motions, that affect the observed oscillation amplitudes in the synthetic images. As a result, this study has shown a lack of clear correlation between the driver input energy flux and the observed oscillation amplitudes for energy fluxes near 100 W m^{-2}, suggesting the existence of additional underlying energy in the observed decayless oscillations, able to sustain the quiet corona.

The aim of our studies was to perform a qualitative study of wave heating from transverse waves in coronal loops. Identifying the spatial evolution of energy dissipation inside a flux tube was the main goal of the last four years. This study was complemented by the additional findings of the development of turbulent loop cross sections, and the lack of correlation between the observed energy fluxes in oscillating loops, and the input fluxes. However, our approach had limitations that need to be addressed in the future. The absence of a realistic atmosphere matching the theoretical models and observations forced us to place our studies in a purely coronal environment. This prevents us from studying the energy transfer between the different layers of the solar atmosphere, especially since we have not included effects like radiative losses and thermal conduction

along the magnetic field. The interaction of different atmospheric layers and their importance in energy dissipation and the evaporation of plasma from the chromosphere into the corona also lied outside the scope of the current study. Additionally, we have not focused on the effects of magnetic field reconnection in the evolution of our systems, due to the inherent difficulties posed by the cost of the 3D MHD simulations.

In the topic of wave heating, the follow up studies will need to focus on the inclusion of realistic drivers, for the generation of the transverse oscillations. The use of broadband drivers could potentially increase the driver efficiency, as well as reproduce the observed higher harmonics in decayless loop oscillations, like those detected by Duckenfield et al. (2018). The proposed explanation of decayless oscillations as a self-oscillatory process (Nakariakov et al. 2016) should also be extensively studied in 3D setups of coronal loops. Finally, incorporating techniques to model the transition region, while bypassing the computational cost for 3D models (Johnston et al. 2017a,b) should also be given high priority in studies of wave energy dissipation. Through these additions, the different aspects of wave heating in coronal loops can be examined in greater detail, providing us with a more complete idea of the undergoing physical processes in the solar atmosphere.

Bibliography

Afanasyev, A., Karampelas, K., & Van Doorsselaere, T. 2019, ApJ, 876, 100

Andries, J., Goossens, M., Hollweg, J. V., Arregui, I., & Van Doorsselaere, T. 2005, A&A, 430, 1109

Anfinogentov, S., Nisticò, G., & Nakariakov, V. M. 2013, A&A, 560, A107

Anfinogentov, S. A., Nakariakov, V. M., & Nisticò, G. 2015, A&A, 583, A136

Antolin, P., De Moortel, I., Van Doorsselaere, T., & Yokoyama, T. 2016, ApJL, 830, L22

Antolin, P., De Moortel, I., Van Doorsselaere, T., & Yokoyama, T. 2017, ApJ, 836, 219

Antolin, P., Okamoto, T. J., De Pontieu, B., et al. 2015, The Astrophysical Journal, 809, 72

Antolin, P. & Rouppe van der Voort, L. 2012, ApJ, 745, 152

Antolin, P., Schmit, D., Pereira, T. M. D., De Pontieu, B., & De Moortel, I. 2018, ApJ, 856, 44

Antolin, P., Vissers, G., Pereira, T. M. D., Rouppe van der Voort, L., & Scullion, E. 2015, ApJ, 806, 81

Antolin, P., Yokoyama, T., & Van Doorsselaere, T. 2014, The Astrophysical Journal Letters, 787, L22

Arregui, I. 2015, Philosophical Transactions of the Royal Society of London Series A, 373, 20140261

Arregui, I., Van Doorsselaere, T., Andries, J., Goossens, M., & Kimpe, D. 2005, A&A, 441, 361

Aschwanden, M. J. 2004, Physics of the Solar Corona. An Introduction (Praxis Publishing Ltd)

Aschwanden, M. J. 2006, Philosophical Transactions of the Royal Society of London Series A, 364, 417

Aschwanden, M. J., de Pontieu, B., Schrijver, C. J., & Title, A. M. 2002, Sol. Phys., 206, 99

Aschwanden, M. J., Fletcher, L., Schrijver, C. J., & Alexander, D. 1999, ApJ, 520, 880

Aschwanden, M. J., Nightingale, R. W., Andries, J., Goossens, M., & Van Doorsselaere, T. 2003, ApJ, 598, 1375

Babcock, H. W. 1961, ApJ, 133, 572

Barbulescu, M., Ruderman, M. S., Van Doorsselaere, T., & Erdélyi, R. 2019, ApJ, 870, 108

Beliën, A. J. C., Martens, P. C. H., & Keppens, R. 1999, ApJ, 526, 478

Berghmans, D. & Clette, F. 1999, Sol. Phys., 186, 207

Browning, P. K. & Priest, E. R. 1984, A&A, 131, 283

Cargill, P. J., De Moortel, I., & Kiddie, G. 2016, ApJ, 823, 31

Cargill, P. J. & Klimchuk, J. A. 2004, ApJ, 605, 911

Chitta, L. P., Peter, H., & Solanki, S. K. 2018, A&A, 615, L9

Cranmer, S. R. 2002, Space Sci. Rev., 101, 229

De Moortel, I. & Browning, P. 2015, Philosophical Transactions of the Royal Society of London Series A, 373, 20140269

De Moortel, I., Ireland, J., & Walsh, R. W. 2000, A&A, 355, L23

De Moortel, I. & Nakariakov, V. M. 2012, Philosophical Transactions of the Royal Society of London Series A, 370, 3193

De Moortel, I. & Pascoe, D. J. 2012, ApJ, 746, 31

De Moortel, I., Pascoe, D. J., Wright, A. N., & Hood, A. W. 2016, Plasma Physics and Controlled Fusion, 58, 014001

De Pontieu, B., De Moortel, I., Martinez-Sykora, J., & McIntosh, S. W. 2017a, ApJL, 845, L18

De Pontieu, B., Martínez-Sykora, J., & Chintzoglou, G. 2017b, ApJL, 849, L7

De Pontieu, B., McIntosh, S. W., Carlsson, M., et al. 2007a, Science, 318, 1574

De Pontieu, B., McIntosh, S. W., Carlsson, M., et al. 2007b, Science, 318, 1574

Dedner, A., Kemm, F., Kröner, D., et al. 2002, Journal of Computational Physics, 175, 645

DeForest, C. E. & Gurman, J. B. 1998, ApJL, 501, L217

Duckenfield, T., Anfinogentov, S. A., Pascoe, D. J., & Nakariakov, V. M. 2018, ApJL, 854, L5

Edlén, B. 1943, ZAp, 22, 30

Edwin, P. M. & Roberts, B. 1983, Sol. Phys., 88, 179

Froment, C., Auchère, F., Aulanier, G., et al. 2017, ApJ, 835, 272

Froment, C., Auchère, F., Bocchialini, K., et al. 2015, ApJ, 807, 158

Goddard, C. R., Antolin, P., & Pascoe, D. J. 2018, ApJ, 863, 167

Goddard, C. R., Pascoe, D. J., Anfinogentov, S., & Nakariakov, V. M. 2017, A&A, 605, A65

Godunov, S. K. 1959, Mat. Sb. (N.S.), 47

Goedbloed, J. P., Keppens, R., & Poedts, S. 2010, Advanced Magnetohydrodynamics

Goedbloed, J. P. H. & Poedts, S. 2004, Principles of Magnetohydrodynamics

Goossens, M., Andries, J., & Arregui, I. 2006, Philosophical Transactions of the Royal Society of London A: Mathematical, Physical and Engineering Sciences, 364, 433

Goossens, M., Andries, J., & Aschwanden, M. 2002, Astronomy & Astrophysics, 394, L39

Goossens, M., Erdélyi, R., & Ruderman, M. S. 2011, Space Sci. Rev., 158, 289

Goossens, M., Hollweg, J. V., & Sakurai, T. 1992, Sol. Phys., 138, 233

Goossens, M. & Poedts, S. 1992, ApJ, 384, 348

Goossens, M., Soler, R., Terradas, J., Van Doorsselaere, T., & Verth, G. 2014, ApJ, 788, 9

Goossens, M., Terradas, J., Andries, J., Arregui, I., & Ballester, J. L. 2009, A&A, 503, 213

Goossens, M., Van Doorsselaere, T., Soler, R., & Verth, G. 2013, ApJ, 768, 191

Grotrian, W. 1939, Naturwissenschaften, 27, 214

Guo, M., Van Doorsselaere, T., Karampelas, K., & Li, B. 2019a, arXiv e-prints, arXiv:1907.08013

Guo, M., Van Doorsselaere, T., Karampelas, K., et al. 2019b, ApJ, 870, 55

Hasan, S. S., Kalkofen, W., & van Ballegooijen, A. A. 2000, ApJL, 535, L67

Heyvaerts, J. & Priest, E. R. 1983, A&A, 117, 220

Hillier, A., Barker, A., Arregui, I., & Latter, H. 2019, MNRAS, 482, 1143

Hollweg, J. V. 1981, Sol. Phys., 70, 25

Howson, T. A., De Moortel, I., & Antolin, P. 2017a, A&A, 607, A77

Howson, T. A., De Moortel, I., & Antolin, P. 2017b, A&A, 602, A74

Ionson, J. A. 1978, ApJ, 226, 650

Jess, D. B., Mathioudakis, M., Erdélyi, R., et al. 2009, Science, 323, 1582

Johnston, C. D., Hood, A. W., Cargill, P. J., & De Moortel, I. 2017a, A&A, 597, A81

Johnston, C. D., Hood, A. W., Cargill, P. J., & De Moortel, I. 2017b, A&A, 605, A8

Judge, P. G., Tritschler, A., & Chye Low, B. 2011, ApJL, 730, L4

Karampelas, K., Millas, D., Katsoulakos, G., Lingri, D., & Vlahakis, N. 2013, in 11th Hellenic Astronomical Conference, 30–30

Karampelas, K. & Van Doorsselaere, T. 2018, A&A, 610, L9

Karampelas, K., Van Doorsselaere, T., & Antolin, P. 2017, A&A, 604, A130

Karampelas, K., Van Doorsselaere, T., & Guo, M. 2019a, A&A, 623, A53

Karampelas, K., Van Doorsselaere, T., Pascoe, J. D., Guo, M., & Antolin, P. 2019b, Frontiers in Astronomy and Space Sciences, 6, 38

Keppens, R. & Demaerel, T. 2016, Physics of Plasmas, 23, 122117

Keppens, R., Meliani, Z., van Marle, A. J., et al. 2012, Journal of Computational Physics, 231, 718

Klimchuk, J. A. 2006, Sol. Phys., 234, 41

Koskinen, H. E. J. & Huttunen, K. E. J. 2006, Space Sci. Rev., 124, 169

Krishna Prasad, S., Banerjee, D., & Singh, J. 2012a, Sol. Phys., 281, 67

Krishna Prasad, S., Banerjee, D., & Van Doorsselaere, T. 2014, ApJ, 789, 118

Krishna Prasad, S., Banerjee, D., Van Doorsselaere, T., & Singh, J. 2012b, A&A, 546, A50

Krishna Prasad, S., Jess, D. B., & Khomenko, E. 2015, ApJL, 812, L15

Kuhn, J. R., Bush, R., Emilio, M., & Scholl, I. F. 2012, Science, 337, 1638

Kuridze, D., Henriques, V., Mathioudakis, M., et al. 2015, ApJ, 802, 26

Kuridze, D., Zaqarashvili, T. V., Henriques, V., et al. 2016, ApJ, 830, 133

Leighton, R. B. 1969, ApJ, 156, 1

Liu, W., Title, A. M., Zhao, J., et al. 2011, ApJL, 736, L13

Magyar, N. & Van Doorsselaere, T. 2016, A&A, 595, A81

Magyar, N. & Van Doorsselaere, T. 2016, The Astrophysical Journal, 823, 82

Magyar, N., Van Doorsselaere, T., & Goossens, M. 2017, Scientific Reports, 7, 14820

Magyar, N., Van Doorsselaere, T., & Marcu, A. 2015, A&A, 582, A117

Mariska, J. T. 2006, ApJ, 639, 484

Martínez-Sykora, J., De Pontieu, B., Hansteen, V. H., et al. 2017, Science, 356, 1269

Matsakos, T., Vlahakis, N., Tsinganos, K., et al. 2012, Astronomy & Astrophysics, 545, A53

McIntosh, S. W. & De Pontieu, B. 2012, ApJ, 761, 138

McIntosh, S. W., de Pontieu, B., Carlsson, M., et al. 2011, Nature, 475, 477

Mignone, A., Bodo, G., Vaidya, B., & Mattia, G. 2018, ApJ, 859, 13

Mignone, A., Zanni, C., Tzeferacos, P., et al. 2012, ApJS, 198, 7

Millas, D., Katsoulakos, G., Lingri, D., Karampelas, K., & Vlahakis, N. 2014, in International Journal of Modern Physics Conference Series, Vol. 28, International Journal of Modern Physics Conference Series, 1460200

Moreno-Insertis, F. & Galsgaard, K. 2013, ApJ, 771, 20

Morton, R. J. & McLaughlin, J. A. 2013, A&A, 553, L10

Morton, R. J., Tomczyk, S., & Pinto, R. F. 2016, ApJ, 828, 89

Morton, R. J., Verth, G., Jess, D. B., et al. 2012, Nature Communications, 3, 1315

Morton, R. J., Weberg, M. J., & McLaughlin, J. A. 2019, Nature Astronomy, 196

Nakariakov, V. M., Anfinogentov, S. A., Nisticò, G., & Lee, D.-H. 2016, A&A, 591, L5

Nakariakov, V. M. & Ofman, L. 2001, A&A, 372, L53

Nakariakov, V. M., Ofman, L., Deluca, E. E., Roberts, B., & Davila, J. M. 1999, Science, 285, 862

Nakariakov, V. M. & Verwichte, E. 2005, Living Reviews in Solar Physics, 2, 3

Nisticò, G., Nakariakov, V. M., & Verwichte, E. 2013, A&A, 552, A57

Nordlund, Å., Stein, R. F., & Asplund, M. 2009, Living Reviews in Solar Physics, 6, 2

Ofman, L., Davila, J. M., & Steinolfson, R. S. 1994a, in IAU Colloq. 144: Solar Coronal Structures, ed. V. Rusin, P. Heinzel, & J.-C. Vial, 473–477

Ofman, L., Davila, J. M., & Steinolfson, R. S. 1994b, ApJ, 421, 360

Ofman, L., Davila, J. M., & Steinolfson, R. S. 1994c, Geophys. Res. Lett., 21, 2259

Ofman, L., Klimchuk, J. A., & Davila, J. M. 1998, ApJ, 493, 474

Okamoto, T. J., Antolin, P., De Pontieu, B., et al. 2015, ApJ, 809, 71

Okamoto, T. J., Tsuneta, S., Berger, T. E., et al. 2007, Science, 318, 1577

Pagano, P. & De Moortel, I. 2017, A&A, 601, A107

Pagano, P. & De Moortel, I. 2019, A&A, 623, A37

Pagano, P., Pascoe, D. J., & De Moortel, I. 2018, A&A, 616, A125

Pant, V., Dolla, L., Mazumder, R., et al. 2015, ApJ, 807, 71

Parker, E. N. 1988, ApJ, 330, 474

Pasachoff, J. M. 2003, The Complete Idiot's Guide to The Sun

Pasachoff, J. M., Jacobson, W. A., & Sterling, A. C. 2009, Sol. Phys., 260, 59

Pascoe, D. J., Anfinogentov, S. A., Goddard, C. R., & Nakariakov, V. M. 2018, ApJ, 860, 31

Pascoe, D. J., Goddard, C. R., & Nakariakov, V. M. 2016a, A&A, 593, A53

Pascoe, D. J., Goddard, C. R., Nisticò, G., Anfinogentov, S., & Nakariakov, V. M. 2016b, A&A, 589, A136

Pascoe, D. J., Hood, A. W., de Moortel, I., & Wright, A. N. 2012, A&A, 539, A37

Pascoe, D. J., Hood, A. W., & Van Doorsselaere, T. 2019, Frontiers in Astronomy and Space Sciences, 6, 22

Pascoe, D. J., Russell, A. J. B., Anfinogentov, S. A., et al. 2017, A&A, 607, A8

Pascoe, D. J., Wright, A. N., & De Moortel, I. 2010, ApJ, 711, 990

Peter, H. & Bingert, S. 2012, A&A, 548, A1

Peter, H., Bingert, S., Klimchuk, J. A., et al. 2013, A&A, 556, A104

Peter, H., Tian, H., Curdt, W., et al. 2014, Science, 346, 1255726

Poedts, S. & Boynton, G. C. 1996, A&A, 306, 610

Poedts, S. & Goedbloed, J. P. 1997, A&A, 321, 935

Poedts, S. & Kerner, W. 1991, Physical Review Letters, 66, 2871

Poedts, S., Toth, G., Belien, A. J. C., & Goedbloed, J. P. 1997, Sol. Phys., 172, 45

Porth, O., Xia, C., Hendrix, T., Moschou, S. P., & Keppens, R. 2014, ApJS, 214, 4

Powell, K. G., Roe, P. L., Linde, T. J., Gombosi, T. I., & De Zeeuw, D. L. 1999, Journal of Computational Physics, 154, 284

Reale, F. 2014, Living Reviews in Solar Physics, 11, 4

Reale, F. & Peres, G. 2000, ApJL, 528, L45

Rouppe van der Voort, L., Leenaarts, J., de Pontieu, B., Carlsson, M., & Vissers, G. 2009, ApJ, 705, 272

Ruderman, M. & Roberts, B. 2002, The Astrophysical Journal, 577, 475

Ruderman, M. S., Goossens, M., & Andries, J. 2010, Physics of Plasmas, 17, 082108

Ryutov, D. A. & Ryutova, M. P. 1976, Soviet Journal of Experimental and Theoretical Physics, 43, 491

Sakurai, T., Goossens, M., & Hollweg, J. V. 1991, Sol. Phys., 133, 227

Schrijver, C. J. 2001, Sol. Phys., 198, 325

Schrijver, C. J., Aschwanden, M. J., & Title, A. M. 2002, Sol. Phys., 206, 69

Simon, G. W. & Leighton, R. B. 1964, ApJ, 140, 1120

Skogsrud, H., Rouppe van der Voort, L., & De Pontieu, B. 2014, ApJL, 795, L23

Soler, R. & Terradas, J. 2015, ApJ, 803, 43

Terradas, J., Andries, J., Goossens, M., et al. 2008, ApJL, 687, L115

Terradas, J., Andries, J., & Verwichte, E. 2011, A&A, 527, A132

Terradas, J., Goossens, M., & Verth, G. 2010, Astronomy & Astrophysics, 524, A23

Terradas, J., Magyar, N., & Van Doorsselaere, T. 2018, ApJ, 853, 35

Terradas, J. & Ofman, L. 2004, ApJ, 610, 523

Testa, P. & Reale, F. 2012, ApJL, 750, L10

Thurgood, J. O., Morton, R. J., & McLaughlin, J. A. 2014, ApJL, 790, L2

Tomczyk, S. & McIntosh, S. W. 2009, ApJ, 697, 1384

Tomczyk, S., McIntosh, S. W., Keil, S. L., et al. 2007, Science, 317, 1192

Toro, E. F. 2009, Riemann Solvers and Numerical Methods for Fluid Dynamics: A Practical Introduction

Tóth, G. 2000, Journal of Computational Physics, 161, 605

Uchimoto, E., Strauss, H. R., & Lawson, W. S. 1991, Sol. Phys., 134, 111

van Ballegooijen, A. A., Asgari-Targhi, M., & Berger, M. A. 2014, ApJ, 787, 87

van Ballegooijen, A. A., Asgari-Targhi, M., & Voss, A. 2017, ApJ, 849, 46

Van Doorsselaere, T., Andries, J., & Poedts, S. 2007, A&A, 471, 311

Van Doorsselaere, T., Antolin, P., & Karampelas, K. 2018, A&A, 620, A65

Van Doorsselaere, T., Antolin, P., Yuan, D., Reznikova, V., & Magyar, N. 2016, Frontiers in Astronomy and Space Sciences, 3, 4

Van Doorsselaere, T., Gijsen, S. E., Andries, J., & Verth, G. 2014a, ApJ, 795, 18

Van Doorsselaere, T., Gijsen, S. E., Andries, J., & Verth, G. 2014b, ApJ, 795, 18

Van Doorsselaere, T., Nakariakov, V. M., & Verwichte, E. 2008, The Astrophysical Journal Letters, 676, L73

Van Doorsselaere, T., Ruderman, M. S., & Robertson, D. 2008, A&A, 485, 849

Vashalomidze, Z., Kukhianidze, V., Zaqarashvili, T. V., et al. 2015, A&A, 577, A136

Vernazza, J. E., Avrett, E. H., & Loeser, R. 1981, ApJS, 45, 635

Verth, G., Terradas, J., & Goossens, M. 2010, ApJL, 718, L102

Verwichte, E., Aschwanden, M. J., Van Doorsselaere, T., Foullon, C., & Nakariakov, V. M. 2009, ApJ, 698, 397

Verwichte, E., Foullon, C., & Van Doorsselaere, T. 2010, ApJ, 717, 458

Verwichte, E., Nakariakov, V. M., & Cooper, F. C. 2005, A&A, 430, L65

Verwichte, E., Nakariakov, V. M., Ofman, L., & Deluca, E. E. 2004, Sol. Phys., 223, 77

Viall, N. M. & Klimchuk, J. A. 2012, ApJ, 753, 35

Wang, T. J., Solanki, S. K., Curdt, W., et al. 2003a, A&A, 406, 1105

Wang, T. J., Solanki, S. K., Innes, D. E., Curdt, W., & Marsch, E. 2003b, A&A, 402, L17

Wedemeyer-Böhm, S., Lagg, A., & Nordlund, Å. 2009, Space Sci. Rev., 144, 317

White, R. S. & Verwichte, E. 2012, A&A, 537, A49

White, R. S., Verwichte, E., & Foullon, C. 2012, A&A, 545, A129

Wilhelm, K., Abbo, L., Auchère, F., et al. 2011, A&ARv, 19 [[arXiv]1103.4481]

Withbroe, G. L. & Noyes, R. W. 1977, ARA&A, 15, 363

Xia, C., Keppens, R., & Fang, X. 2017, A&A, 603, A42

Yu, D. J., Van Doorsselaere, T., & Goossens, M. 2017, ApJ, 850, 44

Yuan, D. & Van Doorsselaere, T. 2016, ApJS, 223, 23

Zajtsev, V. V. & Stepanov, A. V. 1975, Issledovaniia Geomagnetizmu Aeronomii i Fizike Solntsa, 37, 3

Zaqarashvili, T. V., Zhelyazkov, I., & Ofman, L. 2015, ApJ, 813, 123

Curriculum Vitae

General information

Name:	Konstantinos Karampelas
Nationality:	Hellenic
Gender:	male
Telephone (work):	+32 16376252
Ethnicity:	Hellenic
Work Address:	Celestijnenlaan 200B box 2400, B-3001 Leuven, Belgium
Current Address:	Bogaardenstraat 23, B-3000 Leuven, Belgium
Permanent Address:	Apollonias 42, 12135 Peristeri, Greece
Email (work):	kostas.karampelas@kuleuven.be
Email (private):	kk.physicsvanity@gmail.com

Employment history

26.10.2015 – 25.10.2019	PhD student at the KU Leuven, Belgium
2013–2014	Mandatory military service

Education History

Period	Degree	Grade
2015 – 2019	PhD in mathematics (KU Leuven, Belgium) Supervisor: T. Van Doorsselaere	–
2012 – 2014	Master of Science (M.Sc.) in Astrophysics (University of Athens, Greece) Thesis supervisor: N. Vlahakis	excellent
2007 – 2012	Bachelor of Science (B.Sc.) in Physics (University of Athens, Greece) Thesis supervisor: N. Vlahakis	very good

Doctoral Thesis

Dynamics and energetics of coronal loops undergoing decayless oscillations
Supervisor: T. Van Doorsselaere

Master Thesis

Relativistic Magnetohydrodynamics in Kerr Spacetime: Application to Astrophysical Outflows
Supervisor: N. Vlahakis

Undergraduate Thesis

The magnetorotational instability in accretion disks
Supervisor: N. Vlahakis

Research Interests

- Non-relativistic, special relativistic and general relativistic MHD
- Solar Physics, waves in the solar atmosphere
- Astrophysical flows (accretion flows, winds and jets)
- Computational (astro-)physics

Teaching experience

Training and experience as teaching assistant in KU Leuven for the following courses:

- Calculus II (1st year bachelor in Mathematics, teaching period 2016-2017, 2017-2018 and 2018-2019)
- Differential equations (2nd year bachelor in Bio-Science Engineering, teaching period 2018-2019)
- Fluid dynamics (3rd year bachelor in Mathematics, teaching period 2016-2017, 2017-2018 and 2018-2019)

Skills

- Languages: Greek (native speaker), English (C2), German (B1), Dutch (B1)
- Good knowledge of Python and Mathematica, basic knowledge of C and Fortran
- Experienced with MatLab, IDL and gnuplot

Other Interests

- Music - 'Bedroom' guitar player
- Movies and theater
- Drawing
- Board and video games
- Reading
- History enthusiast

Refereed Publications (first author)

1. Karampelas, K., Van Doorsselaere, T., Pascoe, J. D., Guo, M., & Antolin, P. 2019b, Frontiers in Astronomy and Space Sciences, 6, 38

2. Karampelas, K., Van Doorsselaere, T., & Guo, M. 2019a, A&A, 623, A53
3. Karampelas, K. & Van Doorsselaere, T. 2018, A&A, 610, L9
4. Karampelas, K., Van Doorsselaere, T., & Antolin, P. 2017, A&A, 604, A130

Refereed Publications (coauthor)

1. Guo, M., Van Doorsselaere, T., Karampelas, K., & Li, B. 2019a, arXiv e-prints, arXiv:1907.08013
2. Afanasyev, A., Karampelas, K., & Van Doorsselaere, T. 2019, ApJ, 876, 100
3. Guo, M., Van Doorsselaere, T., Karampelas, K., et al. 2019b, ApJ, 870, 55
4. Van Doorsselaere, T., Antolin, P., & Karampelas, K. 2018, A&A, 620, A65
5. Matsakos, T., Vlahakis, N., Tsinganos, K., et al. 2012, Astronomy & Astrophysics, 545, A53

Conference Proceedings

1. Millas, D., Katsoulakos, G., Lingri, D., Karampelas, K., & Vlahakis, N. 2014, in International Journal of Modern Physics Conference Series, Vol. 28, International Journal of Modern Physics Conference Series, 1460200
2. Karampelas, K., Millas, D., Katsoulakos, G., Lingri, D., & Vlahakis, N. 2013, in 11th Hellenic Astronomical Conference, 30–30

Conferences, workshops, summer schools (attendance and contributions)

- *14th Hellenic Astronomical Conference*, 8-11 July, 2019, Volos, Greece – **talk**
- *9th Coronal Loops Workshop*, 11-14 June, 2019, St Andrews, UK – poster
- *2nd China-Europe Solar Physics Meeting (CESPM 2019)*, 6-10 May, 2019, Hvar, Croatia – poster

- *Waves and instabilities in the solar atmosphere: Confronting the current state-of-the-art*, 3-7 September, 2018, La Laguna, Tenerife, Spain – poster
- *UK Magnetohydrodynamics Meeting (UKMHD) 2018*, 25-28 March, 2018, St Andrews, UK – **talk**
- *Wave-based heating mechanisms in the solar atmosphere*, 12th January, 2018, London, UK – **talk**
- *Our mysterious Sun: magnetic coupling between solar interior and atmosphere*, 25-29 September, 2017, Tbilisi, Georgia – **Invited contributed talk**
- *ICNSP2017 & Frontiers of Astrophysical Modeling*, 18-20 & 21-22 September, 2017, Leuven, Belgium – poster
- *ESPM-15*, 04-08 September, 2017, Budapest, Hungary – poster
- *8th Coronal Loops Workshop*, 27-30 June, 2017, Palermo, Italy – **talk**
- *1st CESPM*, 15-19 May, 2017, Kunming, China – **talk**
- *The 5th SOLARNET summer school and workshop*, 25.08-01.09 2016, Belfast, UK – school and **talk**
- *EWASS 2016*, 4-8 July 2016, Athens, Greece – poster
- *IBUKS2016*, 13-17 June 2016, Leuven, Belgium – poster
- *Accretion and Outflows Workshop*, 1-3 October 2014, Lyon, France
- *11th Hellenic Astronomical Conference*, 8-12 September 2013, Athens – poster
- *The Role and the Origin of Magnetic Fields in Astrophysics*, 11-12.03.2013, Athens, Greece
- *XMM-Newton Advanced X-ray Astronomy school*, 13-14.12.2012, Athens, Greece – school
- *5th International Symposium on High Energy Gamma-Ray Astronomy (Gamma 2012)*, 9-13.7.2012, Heidelberg Germany

FACULTY OF SCIENCE
DEPARTMENT OF MATHEMATICS
CENTRE FOR MATHEMATICAL PLASMA ASTROPHYSICS (CMPA)
Celestijnenlaan 200B, box 2400, room 03.35
B-3001 Leuven
kostas.karampelas@kuleuven.be
http://wis.kuleuven.be/CmPA

